CORA Cork Open Research Archive
Cartlann Taighde Oscailte Chorcaí

Title	Nanofiber control of ultracold quantum gases
Authors	Hennessy, Tara
Publication date	2016
Original Citation	Hennessy, T. 2016. Nanofiber control of ultracold quantum gases. PhD Thesis, University College Cork.
Type of publication	Doctoral thesis
Rights	© 2016, Tara Hennessy. - http://creativecommons.org/licenses/by-nc-nd/3.0/
Download date	2026-11-06 15:36:19
Item downloaded from	https://hdl.handle.net/10468/2447



UCC
University College Cork, Ireland
Coláiste na hOllscoile Corcaigh

NATIONAL UNIVERSITY OF IRELAND, CORK



Nanofiber Control of Ultracold Quantum Gases

by

Tara Hennessy

A thesis submitted in partial fulfillment for the degree of Doctor of Philosophy

in the Department of Physics, Faculty of Science

Primary Supervisor: Prof. Thomas Busch

Secondary Supervisor: Prof. Andy Ruth

Head of Department: Prof. John McInerney

March 2016

These are better days, baby.

– Bruce Springsteen

Declaration of Authorship

I, Tara Hennessy, declare that this thesis entitled, 'Nanofiber Control of Ultracold Quantum Gases', and the work presented in it are my own work except where there is clear acknowledgement and appropriate reference to the work of others.

Signed: _____

Date: _____

External Examiner
Dr. Sonja Franke-Arnold – Glasgow University, Scotland, United Kingdom

Internal Examiner
Dr. Andreas Ruschhaupt – University College Cork, Ireland

Abstract

While a great amount of attention is being given to the development of nano-devices, both through academic research and private industry, the field is still on the verge. Progress hinges upon the development of tools and components that can precisely control the interaction between light and matter, and that can be efficiently integrated into nano-devices. Nanofibers are one of the most promising candidates for such purposes. However, in order to fully exploit their potential, a more intimate knowledge of how nanofibers interact with single neutral atoms must be gained. As we learn more about the properties of nanofiber modes, and the way they interface with atoms, and as the technology develops that allows them to be prepared with more precisely known properties, they become more and more adaptable and effective. The work presented in this thesis touches on many topics, which is testament to the broad range of applications and high degree of promise that nanofibers hold. For immediate use, we need to fully grasp how they can be best implemented as sensors, filters, detectors, and switches in existing nano-technologies. Areas of interest also include how they might be best exploited for probing atom-surface interactions, single-atom detection and single photon generation. Nanofiber research is also motivated by their potential integration into fundamental cold atom quantum experiments, and the role they can play there. Combining nanofibers with existing optical and quantum technologies is a powerful strategy for advancing areas like quantum computation, quantum information processing, and quantum communication. In this thesis I present a variety of theoretical work, which explores a range of the applications listed above. The first work presented concerns the use of the evanescent fields around a nanofiber to manipulate an existing trapping geometry and therefore influence the centre-of-mass dynamics of the atom. The second work presented explores interesting trapping geometries that can be achieved in the vicinity of a fiber in which just four modes are allowed to propagate. In a third study I explore the use of a nanofiber as a detector of small numbers of photons by calculating the rate of emission into the fiber modes when the fiber is moved along next to a regularly separated array of atoms. Also included are some results from a work in progress, where I consider the scattered field that appears along the nanofiber axis when a small number of atoms trapped along that axis are illuminated orthogonally; some interesting preliminary results are outlined. Finally, in contrast with the rest of the thesis, I consider some interesting physics that can be done in one of the trapping geometries that can be created around the fiber, here I explore the ground states of a phase separated two-component superfluid Bose–Einstein condensate trapped in a toroidal potential.

Acknowledgements

One page is not enough to express the many thanks I owe to all the people who have encouraged and supported me, both within and outside the scientific field over the course of this PhD. Firstly, I am deeply indebted to my supervisor Prof. Thomas Busch for his many suggestions and his constant support and encouragement during this research, without which this work would not have been possible. Thank you for your patience. It has been a privilege to have a supervisor who wants to guide happy, fulfilled people as well as do great science. Through this research group I have come to know many wonderful people who I hope I will always count among my friends. I would like to thank every single one of them for their support, wisdom and friendship. There are almost too many to mention, but I will try to name as many as I can, those I forget will have to forgive me. In no particular order; Nicola LoGullo, Ciarán Phelan, Carlo DiFranco, Marta Abad, Suzanne McEndoo, Albert Benseny Cases, Jiabao Chen, Irina Reshodko, Rashi Sachdeva, Angela White, Chandru Madaiah, Adi David, Steve Campbell, Tadhg Morgan, Nitica Sakharwade, Miguel Garcia, Gianluca Giorgi, Ricard Menchon Enrich, Yongping Zhang, Mossy Fogarty, Jeremie Gillet, Lee O'Riordan, John Goold, and Brian O'Sullivan. Also, massive thanks to Sawako Koki-chan, who has been not only a brilliant research assistant, but also a wonderful friend to me. Ever since back in the days when we were the *Ultracold Quantum Gases* group in UCC, I always felt that I was part of a strong community. I want to thank my dear friend Susanna Kent who was always nearby for a cup of coffee and a chat. I also want to thank David Rea, who was a wonderful addition to our little group in room 202. Thank you to all the past and present members of Dr. Síle Nic Chormaic's *Light-Matter Interactions Unit* here at OIST who have provided help and advice over the years. It has been an journey that would have been much harder without all of your kindness. I also want to thank Síle for her help and encouragement. Special thanks go also to the late Prof. Vladimir Minogin who generously gave time, encouragement, and guidance. Thanks to Mark, Emily, Will, and Yuna for the days and nights in the OIST village centre, many shared cups of tea, and red wine, and karaoke. Thanks to Lena for the many chats, pancakes, and cups of tea!

A special mention must be included for Mary Frawley and Neil Calder who made it possible to maintain my trad habit in Okinawa, without jigs and reels I'm not altogether sure I'd have made it! To Jim and Amy, you guys made Okinawa that bit more special for Will and I, I'll always remember the role you played, thank you for your friendship. Thanks to Anthony Kiely and Owen McConnell in UCC who were at hand when I needed help with getting paperwork submitted across time-zones. I also want to mention Brendan, Fiona, Anne Marie and Maria, because friends like you are precious. My time with Thomas' research group has been a real adventure that took me from UCC, a university within a 30 minute drive of where I was born and grew up, all the way to the headquarters of the *Quantum Systems Unit* at the other side of the world. Okinawa changed everything for the better, and I will forever be indebted to Thomas for leading me on this adventure. I want to thank my family for all their love and encouragement, I am ever grateful to my parents Sheila and Ger, and my brother Eoghan. Thanks for being a great family! Lastly, I want to thank my husband William, who continues to love me even when I'm the craziest, most stressed-out version of myself, your faithful support through the final stages of this PhD has been greatly appreciated. Thank you all.

ありがとうございます
Tara Hennessy
OIST
November 2015

Contents

Declaration of Authorship **2**

Abstract **i**

Acknowledgements **ii**

1 Introduction **1**
1.1 Ultracold Quantum Gases 1
1.2 Optical Nanofibers 2
1.3 Optical Lattices 3
1.4 The Present Work 4
1.4.1 Outline 4
1.4.2 Publications Relating to this Work 7

2 Background theory **8**
2.1 Optical Dipole Force 8
2.2 Periodic Optical Lattices 13
2.2.1 Bloch Bands and Wannier Functions 15
2.2.2 The Bose–Hubbard Model 16
2.2.3 Superfluid Phase 18
2.2.4 Mott Insulating Phase 18
2.3 Optical Fiber Background Theory 19
2.3.1 Light Propagation in Optical Fibers 20
2.3.2 A Note About TM, TE and Hybrid Modes. 24
2.4 Tapered Optical Nanofibers 25
2.5 The Fundamental Mode HE_{11} 31
2.5.1 The Fundamental HE_{11} Mode With Quasi-Linear Polarization 31
2.5.2 The Fundamental HE_{11} Mode With Circular Polarization . . 35
2.6 The First Three Higher Order Guided Modes 37
2.6.1 The HE_{21} Mode 38
2.6.2 The TE_{01} Mode 39
2.6.3 The TM_{01} Mode 40

2.7 Atom-Surface Interactions 41
2.8 Two-Color Evanescent Field Trap 43
2.8.1 Reasonable Experimental Values 48

3 Creating Atom-Number States Around Tapered Optical Fibers by Loading From an Optical Lattice 51
3.1 Introduction 51
3.2 Paper 53
3.2.1 Scattering of the Lattice at the Fiber Surface: Additional Comments 60
3.3 Conclusions and Future Work 61

4 Shaping the Evanescent Field of Optical Nanofibers for Cold Atom Trapping 63
4.1 Introduction 63
4.2 Paper 66
4.3 Conclusions and Future Work 76

5 Detecting Atoms Trapped In An Optical Lattice Using a Tapered Optical Nanofiber 77
5.1 Introduction 77
5.2 Paper 79
5.3 Conclusions and Future Work 91

6 Confined Light in the Scattered Field of Bosons in a Nanofiber Guided Mode 92
6.1 Abstract 92
6.2 Introduction 93
6.3 Helmholtz Equation in One-Dimension 94
6.4 Two and Three Interacting Bosons 98
6.5 Tonks-Girardeau Gas 105
6.6 Conclusions and Future work 108

7 Rotating Phase Separated Bose–Einstein Condensates in a Ring Trap 111
7.1 Abstract 111
7.2 Introduction 112
7.3 Superfluidity and Spinor Systems 113
7.3.1 Gross–Pitaevskii Picture 113
7.3.2 Vortices and Persistent Currents 116
7.3.3 Toroidal Traps 118
7.4 Radial Phase Separation 121
7.4.1 The Transition from Azimuthal to Radial Phase Separation . 122
7.4.2 Variational Calculation 125
7.5 Azimuthal Phase Separation 128

7.5.1 Emergence of Classical Rotation in Superfluid Bose–Einstein Condensates (paper) 130
7.6 Discussion and Future Work 136

8 Conclusions **137**

Appendices **139**

A Variational Expressions **140**

Bibliography **143**

For my family

Chapter 1

Introduction

1.1 Ultracold Quantum Gases

Almost a century ago, while the theory of quantum mechanics was still in its early stages of development, Albert Einstein generalized some, then recent, work by Satyendra Nath Bose [1] on the statistical nature of photons. Einstein predicted that a phase transition would occur in a non-interacting atomic gas at extremely low temperatures [2]. This transition, now called Bose–Einstein condensation (BEC), leads to a macroscopic occupation of the ground state at finite temperatures. For many years experimental techniques lagged behind Einstein's theory. After the discovery of superfluid Helium (^{4}He), curiosity at Einstein's theory was renewed and in 1938 F. London suggested a connection between superfluidity and Bose–Einstein condensation [3] and the first microscopic theory of interacting Bose gases was developed by N. Bogoliubov [4]. Interest in BEC gathered momentum and many related works followed. Liquid ^{4}He however, is not an ideal candidate for investigating BEC due to its strong interactions which mask the effects predicted by Einstein.

Only in recent decades, with the advent of modern cooling methods and the development of laser technology, has it became possible to cool weakly interacting atomic clouds to the range of temperatures required to achieve BEC. In 1995 three

groups simultaneously reported the first observation of Bose–Einstein condensation in dilute gases [5–7]. Since then many more bosonic atoms have been cooled to quantum degeneracy [8] and the observation of Bose–Einstein condensation was subsequently recognized with the 2001 Nobel Prize for Physics awarded to E. Cornell, C. Wieman and W. Ketterle [9, 10]. While the properties of cold atoms and superfluidity are interesting from a fundamental physics point of view, cold atoms have also demonstrated large potential as *designer* quantum systems, in which other systems can be simulated [11]. This is due to their desirable properties as being fundamental, cold, clean and highly configurable.

1.2 Optical Nanofibers

In the 1960s, Charles K. Kao, known as *The Father of Fiber Optics*, realized that optical fibers could be used for long-range optical communication [12]. Since then optical fibers have revolutionized modern telecommunications and Kao was rewarded for his pioneering work in 2009 when he received half of the Nobel Prize for Physics for "groundbreaking achievements concerning the transmission of light in fibers for optical communication".

Once their impressive capability for low loss light transport and delivery was recognized, optical fibers were primarily developed for, and utilized in, the optical communications industry. Optical fibers boast single mode transmission losses of less than 0.2 dB/km. A high degree of mode confinement results in large optical intensities inside fibers, even for a conservative input power. They are ideal for the delivery of an optical wave over considerable distances and, in addition to revolutionizing the telecommunications industry, have found a wide variety of applications across everything from temperature measurement to medical optics and decoration.

In recent years, Tapered Optical Fibers (TOFs) have become the subject of much research. TOFs are created by taking regular telecommunications optical fiber and tapering it over a hot flame so that the core is vanishing, the cladding replaces the

core, and the vacuum surrounding replaces the cladding [13]. A thin fiber produced in this way can support only a small number of modes. In this case, there exists a pronounced evanescent field that penetrates into the free-space surrounding the fiber. The shape of this evanescent field is characteristic of the fiber properties and the properties of the guided light. TOFs have broad applications as tools for probing [14] and sensing [15] in atom-optics experiments. Their evanescent field can be used for trapping and manipulating atoms at sub-micrometer distances from the fiber surface, a prominent example is the trapping scheme described in [16] and later achieved in [17]. This will be discussed in more detail in Sec. 2.4.

Today, quantum technologies are entering territory that has, until now, been dominated by classical optics. Classical devices have been engineered up to a point where their operation is limited by quantum effects. Meanwhile, new tools are being developed for application in quantum technologies. Optical fibers have so much versatility that, while they continue to offer seemingly endless applications and improvements in classical devices, they are further proving their worth by making new and exciting contributions to quantum devices.

1.3 Optical Lattices

Ultracold quantum gases confined in optical lattices have become a subject of broad interest. An optical lattice is a periodic intensity pattern formed by the interference of one or more pairs of monochromatic laser beams, which provides a clean, regular and versatile trapping geometry for cold atoms (via the ac Stark effect). One of the motivations of this area is that optical lattices allow the imitation of the physics of solid state systems in a highly controllable system [11, 18].

The last decade has yielded some landmark experiments relating to BECs in optical lattices and of particular note is the observation of a quantum phase transition between a superfluid BEC and a Mott-Insulator state [19, 20]. Optical lattices also allow for the dimensionality of a quantum gas to be changed between one-, two- or three- dimensions. A landmark example in this arena is the observation of

a one-dimensional Tonks- Girardeau gas of bosons in a two- dimensional optical lattice [21, 22]. Atoms in optical lattices have found applications in building highly accurate atomic clocks [23] and as strong candidates for use as quantum bits (qubits) in quantum computing [24–26].

In recent years, advances in techniques which allow for control of quantum systems at the single-atom level have accelerated progress in the area of quantum optics. Simultaneously, the highly-controllable environment provided by an optical lattice has proven itself further as an impressive tool for confining and investigating strongly-correlated quantum systems of ultracold atoms [27, 28]. In very recent years the hurdle of single-site addressing has finally been overcome with the advent of the quantum-gas microscope [29, 30]. A detailed review of quantum gases in optical lattices can be found in [11, 18, 31].

1.4 The Present Work

1.4.1 Outline

This thesis is organised as follows:

- **Chapter 2** introduces much of the background theory necessary for understanding the theoretical results in this thesis. Topics covered include the origin of the optical dipole force and the development of optical lattice trapping potentials. The greatest focus of this chapter is on optical fibers, tapered optical nanofibers and their description. The background theory associated with Chapter 6 and Chapter 7 will be later dealt with on a chapter-by-chapter basis. **Chapter 2** provides a detailed overview of the theory needed to begin reading.

- In **Chapter 3** I present a scheme where the evanescent field around a sub-wavelength diameter tapered optical nanofiber is combined with an optical

lattice. The work shows that when the fiber is aligned perpendicularly to the transverse plane of a two-dimensional optical lattice, the evanescent field around the fiber can be used to create a time-dependent potential which *melts* the lattice potential locally. This allows access to a regime in which a small number of atoms can be locally addressed without disturbing the rest of the lattice. If the environment around the fiber is given by a Mott-Insulator state, the melting of the lattice transfers a well-defined number of atoms into the fiber potential.

This work was published in Phys. Rev. A **85**, 053418 (2012).

- In **Chapter 4** novel optical dipole potentials based on the evanescent fields of the TE_{01}, TM_{01} and HE_{21} modes of an optical nanofiber are presented. I show that these allow us to perform a continuous transition between a helical trapping structure around the nano-fiber and a (periodic) rectangular lattice one by simply changing the polarization of the light injected into the fiber. Effects of unwanted mode mixing on the potentials are also investigated.

  This work was published in Opt. Express, **21**, 27093 (2013).

- In **Chapter 5** I show that an optical nanofiber can be used to resolve spontaneous emission from a row of regularly separated atoms in an optical lattice with single site resolution. This work is carried out for the specific example of ^{133}Cs, but the principle is applicable to any atomic species. The small size of the fiber combined with an enhanced photon collection rate allows for the attainment of large and reliable measurement signals.

  This work was published in Opt. Express, **22**, 32509 (2014).

- In **Chapter 6** I describe the properties of a system in which orthogonally incident light is scattered from a small sample of atoms in an elongated trap along the fiber axis. This is done for a classical field when the trap contains two or three atoms with arbitrary interaction strength, or a Tonks-Girardeau gas with a larger number of particles. I first show that the feedback of the light onto the atomic sample is negligible, and then describe the resulting field inside the fiber. For certain values of the interaction constant g and the harmonic oscillator width l of the atomic samples, I show that solutions for the electric field exist that are zero everywhere outside the range of trapping, which means that all of the light scattered into the fiber remains confined.

- In **Chapter 7**, in a divergence from the other chapters, I investigate the superfluid properties of rotating two-component Bose–Einstein condensates in a toroidal potential. Such a potential could be created by using evanescent light fields around a nanofiber. In the first part of this chapter I investigate the radial phase separation that results when one component has much more angular momentum than the other and devise a variational calculation that agrees well with numerical calculations. In the second part of the chapter, I show that azimuthal phase separation of the components can lead to losing the restriction of quantization on angular momentum. This condition is usually considered to be an identifying feature of superfluid flow. I investigate the implications this has on the resulting currents, including evidence that the phase boundary exhibits classical solid body rotation.

  A portion of this work is published in Phys. Rev. A **93**, 033601(2016).

- The last chapter, **Chapter 8**, outlines some general conclusions.

1.4.2 Publications Relating to this Work

T. Hennessy and Th. Busch, *Creating atom-number states around tapered optical fibers by loading from an optical lattice*, Phys. Rev. A **85**, 053418 (2012).

C. Phelan, T. Hennessy, and Th. Busch, *Shaping the evanescent field of optical nanofibers for cold atom trapping*, Opt. Express **21**, 27093 (2013).

T. Hennessy and Th. Busch, *Detecting atoms trapped in an optical lattice using a tapered optical nanofiber*, Opt. Express **22**, 32509 (2014).

A. White, T. Hennessy and Th. Busch, *Emergence of Classical Rotation in Superfluid Bose–Einstein Condensates*, Phys. Rev. A **93**, 033601(2016).

Chapter 2

Background theory

2.1 Optical Dipole Force

The optical dipole force arises from the coherent interaction of an inhomogeneous electromagnetic (EM) field with the induced electric dipole moment of an atom. The force is conservative and is the result of coherent scattering from and into the driving field. The resultant atomic energy level shift is known as the AC-Stark shift and it can lead to an atom experiencing a trapping potential [32–34].

An atom sitting in a laser light field $\mathbf{E}$ has an induced dipole moment $\mathbf{p}$, oscillating at the driving frequency ω. The laser field can be described, as usual, by $\mathbf{E}(\mathbf{r},t) = \hat{\mathbf{e}}\tilde{E}(\mathbf{r})\exp(-i\omega t) + c.c.$ and $\mathbf{p}(\mathbf{r},t) = \hat{\mathbf{e}}\tilde{p}(\mathbf{r})\exp(-i\omega t) + c.c.$, where $\hat{\mathbf{e}}$ is the polarization unit vector and the amplitude $\tilde{p}$ of the dipole moment is related to the amplitude of the field $\tilde{E}$ by $\tilde{p} = \alpha\tilde{E}$. Here α is the complex polarizability of the atomic species in question. The induced optical dipole potential is given by

$$U_{\text{dip}} = -\frac{1}{2}\langle \mathbf{pE}\rangle = -\frac{1}{2\epsilon_0 c^2}\,\text{Re}(\alpha)I, \qquad I = 2\epsilon_0 c|\tilde{E}|^2. \tag{2.1}$$

The angular brackets, $\langle..\rangle$, denote time averaging over the rapidly oscillating terms and the factor of $\frac{1}{2}$ accounts for the fact that the dipole is induced and not permanent. I is the field intensity. The potential energy in the field is proportional to

the real part of the atomic polarizability, $\mathrm{Re}(\alpha)$, and the intensity I. The gradient of U_{dip} therefore gives a conservative dipole force proportional to the gradient of the intensity of the field

$$\mathbf{F}_{\mathrm{dip}}(\mathbf{r}) = -\nabla U_{\mathrm{dip}}(\mathbf{r}) = \frac{1}{2\epsilon_0 c^2}\,\mathrm{Re}(\alpha)\nabla\mathbf{I}(\mathbf{r}). \tag{2.2}$$

The imaginary part of α, the part of the dipole oscillation which is out-of-phase, describes the power being absorbed from the field

$$P_{\mathrm{abs}} = -\frac{d}{dt}U_{\mathrm{dip}} = \frac{1}{2}\langle\dot{\mathbf{p}}\mathbf{E}\rangle + \frac{1}{2}\langle\dot{\mathbf{p}}\mathbf{E}\rangle = \langle\dot{\mathbf{p}}\mathbf{E}\rangle = 2\omega\,\mathrm{Re}(\tilde{p}\tilde{E}^*) = \frac{\omega}{\epsilon_0 c}\,\mathrm{Im}(\alpha)I. \tag{2.3}$$

This power is then reemitted as dipole radiation and, in a divergence from the classical picture, can be thought of as a stream of photons scattered at a rate given by [33]

$$\Gamma_{\mathrm{sc}}(\mathbf{r}) = \frac{P_{\mathrm{abs}}}{\hbar\omega} = \frac{1}{\hbar\epsilon_0 c}\,\mathrm{Im}(\alpha)\,I(\mathbf{r}), \tag{2.4}$$

which leads to unwanted recoils and therefore heating of the atom. All expressions above are valid for any polarizable neutral particle in an oscillating electric field. In summary, the two most important quantities are U_{dip}, which is a function of the real (dispersive) part of α, and Γ_{sc}, which is a function of the imaginary (absorptive) part of α.

An expression for the frequency dependent polarizability $\alpha(\omega)$ of an atom can be found by starting from the classical picture of the well-know Lorentz model. The Lorentz oscillator model assumes that since the nucleus of an atom is much much heavier than an electron (with mass m_e and charge e), the system can be thought of as an electron-spring system connected to a stationary, infinite mass. The oscillations have an eigenfrequency ω_0 corresponding to a particular transition frequency of the particle. In the Lorentz model, the driven oscillation of the electron is modeled based on the damped harmonic oscillator by the equation of motion $\ddot{x} + \Gamma_\omega\dot{x} + \omega_0^2 x = -eE(t)/m_e$, and the solution is given by $x(\omega) =$

$\frac{e/m_e}{\omega^2-\omega_0^2+i\omega\Gamma_\omega}$. The local induced dipole moment is then $\mathbf{p}(\omega) = -e\mathbf{x}(\omega)$, so that

$$\mathbf{p}(\omega) = -\frac{e^2}{m_e}\frac{1}{\omega^2-\omega_0^2+i\omega\Gamma_\omega}\mathbf{E}(\mathbf{t}), \tag{2.5}$$

and α is defined as the pre-factor of $\mathbf{E}(t)$

$$\alpha = \frac{e^2}{m_e}\frac{1}{\omega_0^2-\omega^2-\mathrm{i}\omega\Gamma_\omega}. \tag{2.6}$$

Here

$$\Gamma_\omega = \frac{e^2\omega^2}{6\pi\epsilon_0 m_e c^3}, \tag{2.7}$$

is the classical radiative damping rate. Substituting $e^2/m_e = 6\pi\epsilon_0 c^3\Gamma_\omega/\omega^2$ and using the on-resonance damping rate $\Gamma \equiv \Gamma_{\omega_0} = (\omega_0/\omega)^2\Gamma_\omega$, eq. (2.7) becomes

$$\alpha = 6\pi\epsilon_0 c^3 \frac{\Gamma/\omega_0^2}{\omega_0^2-\omega^2-\mathrm{i}\,(\omega^3/\omega_0^2)\,\Gamma}\ . \tag{2.8}$$

In the semiclassical approach, the atomic polarizability can be calculated by considering the atom as a two-level quantum system interacting with the classical radiation field. Using the above expression for the polarizability of the atom in eqs. (2.1) and (2.4) we arrive at the following expressions for the dipole potential and the scattering rate in the case of large detuning

$$U_{\mathrm{dip}}(\mathbf{r}) = -\frac{3\pi c^2}{2\omega_0^3}\left(\frac{\Gamma}{\omega_0-\omega}+\frac{\Gamma}{\omega_0+\omega}\right) I(\mathbf{r})\,, \tag{2.9}$$

$$\Gamma_{\mathrm{sc}}(\mathbf{r}) = \frac{3\pi c^2}{2\hbar\omega_0^3}\left(\frac{\omega}{\omega_0}\right)^3\left(\frac{\Gamma}{\omega_0-\omega}+\frac{\Gamma}{\omega_0+\omega}\right)^2 I(\mathbf{r})\,. \tag{2.10}$$

These general expressions are valid for any driving frequency ω and show two resonant contributions. Besides the unsurprising resonance at $\omega = \omega_0$, there is also the so-called counter-rotating term resonant at $\omega = -\omega_0$. Using the rotating

wave approximation (RWA), one can neglect the terms like $\frac{\Gamma}{\omega_0+\omega}$ and arrive at

$$U_{\rm dip}(\mathbf{r}) = \frac{3\pi c^2}{2\omega_0^3}\frac{\Gamma}{\Delta}I(\mathbf{r}), \tag{2.11}$$

$$\Gamma_{\rm sc}(\mathbf{r}) = \frac{3\pi c^2}{2\hbar\omega_0^3}\left(\frac{\Gamma}{\Delta}\right)^2 I(\mathbf{r}). \tag{2.12}$$

The RWA is justified as long as the trapping laser is tuned quite close to the dominant resonance at ω_0, because the Rabi frequencies, which govern the dynamics of the population transfer between the levels, are much smaller than the transition frequencies [35]. In this case, the detuning $\Delta \equiv \omega - \omega_0$ meets the condition that $|\Delta| \ll \omega_0$ and so $\omega/\omega_0 \approx 1$. The RWA effectively drops the fast rotating terms, i.e. it says that any term like $e^{i(\omega_0-\omega)t}$ averages to zero on the timescales relevant to relaxation processes.

Spontaneous emission of photons is an incoherent process which leads to heating of the atomic cloud and is usually undesirable during experiments. In order to minimize the photon scattering rate to a level at which the heating is negligible one can make use of the fact that $U_{\rm dip} \propto I/\Delta$ and $\Gamma_{\rm sc} \propto I/\Delta^2$. This means that for detuned optical dipole traps the scattering decreases faster than the trapping strength for increasing values of $|\Delta|$.

Since the force an atom experiences is proportional to the gradient of the potential, it will be attracted to regions of high or low intensity depending on the sign of the detuning. When the laser is detuned to the red of the atomic resonance ($\Delta < 0$) the atom will feel an attractive force towards regions of high intensity and when the laser is detuned to the blue of the atomic resonance ($\Delta > 0$) the atom feels a repulsive force in the high intensity regions eq. (2.12). It is important to remember that the depth of the potential is directly proportional to the intensity of the laser light.

One type of dipole trap, which is of particular relevance in Chapter 3, is an optical lattice. Optical lattices can be created by a standing wave laser light field, which have a periodic arrangement of intensity maxima and minima in space. This represents a periodic arrangement of microtraps in space for the atoms. Optical

lattice trapping potentials are one of the main foci of Chapter 3 and so, after a brief note about laser cooling, I will discuss them in more detail in the next section. Throughout this thesis I will regularly be concerned with the optical trapping potentials formed in the evanescent fields around an optical nanofiber, which are yet another example of an optical dipole trap and will be discussed later.

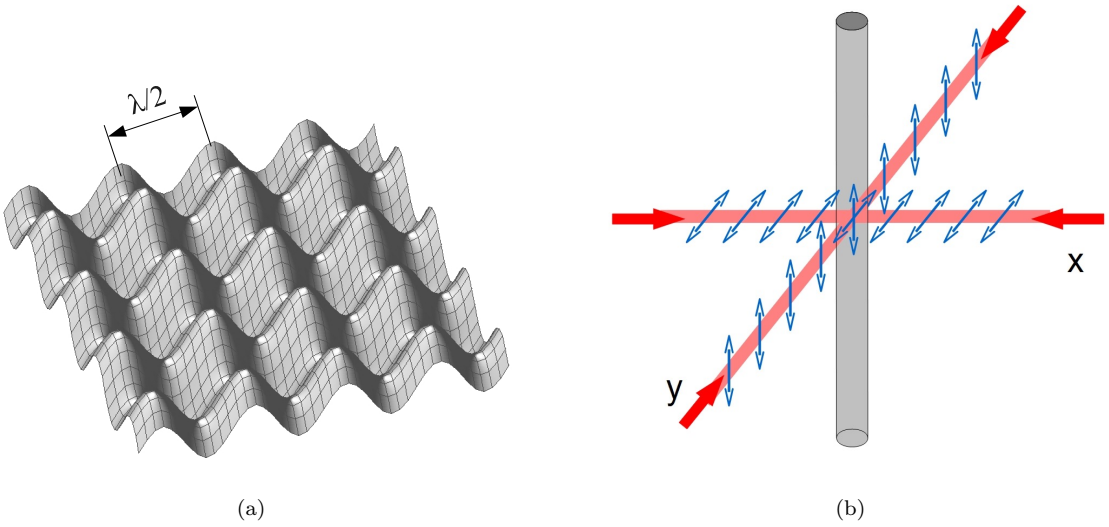
A Note About Laser Cooling

Optical dipole traps typically have depths on the order of a milli-Kelvin [33]. For trapping, atoms therefore need to be cooled to the order of a few hundred micro-Kelvin because at higher temperatures the atoms would have too much energy to be confined in the traps. A collection of atoms can be slowed using the momentum transfer that occurs when an atom absorbs a photon. A magneto-optical trap (MOT) is a device based on this principle. It combines three pairs of counter-propagating laser beams in the x, y and z directions, with an added spatially varying magnetic quadrupole field. Due to conservation of momentum, every time an atom absorbs a photon of wavelength λ the atomic velocity changes by the recoil velocity, $v_{\mathrm{rec}} = \hbar k/m$. Here, $k = 2\pi/\lambda$ and m is the mass of the atom. As the atoms in a gas are in continuous motion they *see* the cooling laser beam at a Doppler shifted frequency compared to the laboratory frame of reference. If the cooling laser is detuned by a magnitude that is less than the difference between the resonance frequencies of the ground and excited states of the transition, $\Delta = \omega - \omega_{\mathrm{A}}$, where ω is the laser frequency and ω_0 is the resonant frequency of the atom, then the moving atoms see the laser frequency shifted by $-\mathbf{k}.\mathbf{v}$, where $\mathbf{k}$ is the free-space wave-vector of the laser light and $\mathbf{v}$ is the atomic velocity. The radiation pressure is therefore stronger for atoms with velocity of opposite sign to the wave vector, i.e. $\mathbf{k}.\mathbf{v} < 0$, and the momentum transfer $\hbar\mathbf{k}$ is opposing the velocity, slowing the atom. After reaching the lower temperature limit achievable through Doppler cooling, the atoms can be further cooled by polarization gradient cooling and evaporative cooling. A detailed description of the stages of laser cooling is outside of the scope of this thesis, but can be found in [36, 37].

2.2 Periodic Optical Lattices

As seen in Sec. 2.1, a laser field can exert a purely conservative dipole force on an atom which will allow the atom to be trapped. In the following discussion we will neglect spontaneous emission, which is justified as in typical optical lattice experiments the lattice is far-detuned and so the rate at which photons are spontaneously emitted is close to zero [27]. An optical lattice potential is generated by overlapping two counter-propagating laser beams of the same frequency. The two laser beams form a standing wave and therefore create a periodic potential with period $\lambda/2$, which can be used to trap atoms. By overlapping the pair of lasers at an angle less than 180° a variety of lattice geometries with larger period can be achieved [38, 39]. To demonstrate the basic properties of an optical lattice, let us assume that we have two waves which are propagating in the x-direction with amplitude E_0 and wavelength $\lambda = 2\pi/k$. Their interference creates an optical potential $V_{\text{lat}}(x) \propto \cos^2(kx)$, which has intensity maxima and minima with periodicity $\lambda/2$. As seen in the Sec. 2.1, the direction of the force depends on the sign of the detuning of the atom. Atoms can be forced to gather at the nodes or anti-nodes of the laser intensity pattern by using blue-detuned ($\omega > \omega_0$) or red-detuned ($\omega < \omega_0$) light respectively. The lattice constant for the atomic lattice is therefore also given by $\lambda/2$.

By introducing additional pairs of laser beams propagating in the y and/or z-directions, a full two or three dimensional periodic trapping potential can be created. One of the most stable and versatile geometries for such a lattice is the two-dimensional potential formed by two pairs of orthogonally arranged, counter-propagating laser beams.



(a) (b)

FIGURE 2.1: (a) Schematic of a two-dimensional optical square lattice. (b) Polarization of laser beams in the square lattice.

A two-dimensional lattice potential made from four laser beams of equal wavelength, λ, equal power, P, and all linearly polarized, can be written as

$$V_{\text{lat}}(x,y) = V_0 \left(\cos^2(kx) + \cos^2(ky) + 2\epsilon_x \cdot \epsilon_y \cos(\phi(t)) \cos(kx) \cos(ky)\right) \ . \quad (2.13)$$

Here ϕ is the time dependent phase between the two polarization vectors ϵ_x and ϵ_y. ϵ_x is transverse to $\hat{x}$ (in y-z plane) and ϵ_y is transverse to $\hat{y}$ (in x-z plane).

For parallel polarization vectors $\epsilon_x = \epsilon_y = \hat{z}$ we have $\epsilon_x \cdot \epsilon_y = 1$ and for orthogonal polarizations between the two standing wave laser fields, or for a time dependent phase of $\phi = \pi/2$, the interference term in eq. (2.13) vanishes and the potential is proportional to the sum of the intensities of the two standing wave light fields, panel (b) in Fig. 2.1 shows the arrangement of laser polarizations that result in a square lattice. Assuming the latter, the potential is therefore represented by the sums of purely sinusoidal orthogonal fields [27] (see Fig. 2.1)

$$V_{\text{lat}}(x,y) = V_0 \left(\cos^2(kx) + \cos^2(ky)\right) \ . \quad (2.14)$$

In each direction the depth of this lattice is directly proportional to the intensity of the corresponding pair of laser beams and therefore the depth of the lattice sites in different directions can be controlled in an experiment. Even though the lattice potential is sinusoidal, for deep optical lattices and very cold atoms a single site can be approximated by a harmonic potential with typical harmonic oscillator (HO) trapping frequencies ω_{HO} of up to 100 kHz [27]. The energy of oscillations within a single well are then given by $\hbar\omega_{HO}$ and can be expressed in units of the recoil energy, $E_R = \hbar^2 k^2/2m$, as $2(E_R)(V_0/E_R)^{\frac{1}{2}}$.

For ^{87}Rb, typical values for the recoil energy are in the region of several kilohertz (or on the order of 10^{30} Joules, or 100 mK). Throughout this thesis we will consider the type of two-dimensional optical lattice described above and given by eq. (2.14). We will assume that there is an extra harmonic confinement present which has the effect of suppressing all oscillations in the z-direction, so that we can concentrate on the physics in two dimensions.

2.2.1 Bloch Bands and Wannier Functions

The localized solutions to a periodic system are given by the Wannier functions [40]. In the case of atoms confined in a two dimensional optical lattice it is convenient to choose these Wannier functions $W(x, y)$ as a basis set since they provide a representation of wave functions localized at single lattice sites. The Wannier functions can be given by linear combinations of the delocalized Bloch states $\phi_k^{(n)}(x) = e^{ikx}u_k^{(n)}(x)$ and $\phi_k^{(n)}(y) = e^{iky}u_k^{(n)}(y)$

$$w_n(x - x_j, y - y_j) = \Theta \sum_k \exp(-ikx_j)\phi_k^{(n)}(x) \times \sum_k \exp(-iky_j)\phi_k^{(n)}(y), \quad (2.15)$$

where Θ is a normalization constant and $(x - j, y_j)$ are the positions of the lattice minima. In the work in Chapter 3 and Chapter 5 we consider very deep optical lattices in which a Mott insulator state has been achieved. In this limit the Wannier functions are a good description of the ground state wave functions [18, 27, 40].

2.2.2 The Bose–Hubbard Model

Since the first observation of Bose–Einstein condensation in 1995 [5–7] the area of ultracold atomic gases has steadily progressed. One of the most notable advances was the experimental realization of the superfluid to Mott insulator transition of ultracold atoms in an optical lattice [19]. Work in this direction has led to an increased interest in the Bose–Hubbard model [27], due to the connection it provides to condensed matter and the body of work already existing in lattice structures in solid state physics.

Ultracold atoms in optical lattices represent an ideal test-bed for quantum many-body theories. They also represent a unique system for carrying out simulations of condensed matter systems, as the lattices can be controlled in a time-dependent way by varying external parameters. In particular, in recent years a variety of Hubbard type lattice models have been realized and investigated and one of the most notable advances in optical lattice physics is the Mott insulator-superfluid transition first achieved by Greiner *et al.* with cold bosonic atoms [19]. The Bose–Hubbard Hamiltonian describes a weakly interacting gas in an optical lattice and is given by

$$H_{\text{full}} = \int d^3x \hat{\Psi}^\dagger(\mathbf{x}) \left(\frac{\mathbf{p}^2}{2m} + V_{\text{lat}}(\mathbf{x}) \right) \hat{\Psi}(\mathbf{x}) + \frac{g}{2} \int dx \hat{\Psi}^\dagger(\mathbf{x}) \hat{\Psi}^\dagger(\mathbf{x}) \hat{\Psi}(\mathbf{x}) \hat{\Psi}\ (\mathbf{x}), \tag{2.16}$$

where $\hat{\Psi}(\mathbf{x})$ is the bosonic field operator for atoms in a well-defined internal atomic state. We also consider an idealized situation where the only trapping potential is that of the lattice, $V_{\text{lat}}(\mathbf{x})$, whereas a full treatment accounting for all experimental effects would also require the consideration of an external trapping potential. As these potentials are usually slowly varying compared to the optical lattice, they can be neglected for our purposes. The interaction strength between two atoms is given by g. If the atoms interact via s-wave scattering only, then g is defined by $g = 4\pi a_s/m$, where a_s is the atomic s-wave scattering length. We assume all particles to be in the lowest band of the optical lattice and expand the field operator in terms of the Wannier functions $\hat{\Psi}(\mathbf{x}) = \sum_i \hat{b}_i w_0(\mathbf{x} - \mathbf{x}_i)$, where $\hat{b}_i$ is

the annihilation operator for a particle at site $\mathbf{x}_i$. This leads to

$$H_{\text{full}} = -\sum_{i,j} J_{ij}\hat{b}_i^\dagger \hat{b}_j + \frac{1}{2}\sum_{i,j,k,l} U_{ijkl}\hat{b}_i^\dagger \hat{b}_j^\dagger \hat{b}_k \hat{b}_l \ , \tag{2.17}$$

where

$$J_{ij} = -\int dx\ w_0(\mathbf{x}-\mathbf{x}_i)\left(\frac{p^2}{2m} + V_{\text{lat}}(\mathbf{x})\right) w_0(\mathbf{x}-\mathbf{x}_j) \ , \tag{2.18}$$

and

$$U_{ijkl} = g\int dx\ w_0(\mathbf{x}-\mathbf{x}_i)w_0(\mathbf{x}-\mathbf{x}_j)w_0(\mathbf{x}-\mathbf{x}_k)w_0(\mathbf{x}-\mathbf{x}_l) \ . \tag{2.19}$$

Note first that diagonal tunneling is forbidden in a cubic lattice since the Wannier functions are orthogonal. As a result, the tunneling matrix elements J_{ij} for sites other than nearest neighbors are small. For such lattices the values of the offsite interaction matrix elements U_{ijkl} involving Wannier functions centered at different lattice sites are also small compared to onsite interactions and we can neglect them [40]. For an isotropic cubic optical lattice one then arrives at the standard Bose–Hubbard Hamiltonian

$$H_{\text{BH}} = -J\sum_{\langle i,j\rangle} \hat{b}_i^\dagger \hat{b}_j + \frac{U}{2}\sum_j \hat{b}_j^\dagger \hat{b}_j^\dagger \hat{b}_j \hat{b}_j \ , \tag{2.20}$$

where $\langle i,j\rangle$ denotes the sum over the nearest neighbors.

The lattice depth V_0 depends directly on the power in the lattice lasers. As the lattice depth increases, tunnelling (J) decreases, and atoms confined at a single site experience an increase in their repulsive energy, U.

The Bose–Hubbard Hamiltonian in eq. (2.16), even in one-dimension, is not an analytically solvable model. Despite this, the principal physics of the model is very well understood. Of particular interest is the observation of a quantum phase transition between a superfluid and insulator phase that the Bose–Hubbard Model exhibits as a function of U/J.

2.2.3 Superfluid Phase

For an ideal gas in the limit of $U = 0$, the eigenstates of H_{BH} can be found for $\epsilon_i = 0$ and periodic boundary conditions. From the eigenvalue equation $E_k^{(0)} = -2J\cos(ka)$ it follows that the lowest Bloch band is at a height $4J$ [27, 40]. The energy takes its minimum value for $k = 0$ and so in this limit particles in the ground state are delocalized over the whole lattice, i.e. the ground state of N particles in the lattice is $|\Psi_{\mathrm{SF}}\rangle \propto (\sum_i \hat{b}_i^\dagger)^N|\mathrm{vac}\rangle$, where $|\mathrm{vac}\rangle$ is the vacuum state. In this limit the system is superfluid (SF) and possesses first order long range off-diagonal correlations [18, 41].

2.2.4 Mott Insulating Phase

In the limit where the interaction parameter U dominates over the hopping term J we have a vastly different situation. Consider the case where the number N of atoms is precisely equal to the number of lattice sites. Interestingly, at about $U \approx 5.8nJ$, where n is the number of nearest neighbors of each lattice site, a quantum phase transition takes place [18, 41]. Long range correlations in the ground state cease to exist and the system is said to become Mott insulating. For the ideal configuration of exactly one atom per lattice site the ground state can be represented as a straightforward product of local Fock states. This Mott insulator state can therefore be written as $|\Psi_{\mathrm{MI}}\rangle \propto \prod_j \hat{b}_j^\dagger|\mathrm{vac}\rangle$. The observation of the transition from a homogeneous BEC superfluid to a Mott insulator has been hailed as one of the most important advances in modern day atomic physics.

Having achieved a MI state with one atom per lattice site, one can now begin to increase J so that U becomes less and less dominant and the atoms begin to hop again. This tunneling results in instances where more than one atom may occupy a single lattice site which increases the energy by U. As long as the gain in kinetic energy due to hopping remains smaller than the interaction energy, the atoms will remain localized. However, for any $J \neq 0$, the ground state is no longer a simple product state. Once J becomes of the order of, or larger than, U, the gain in

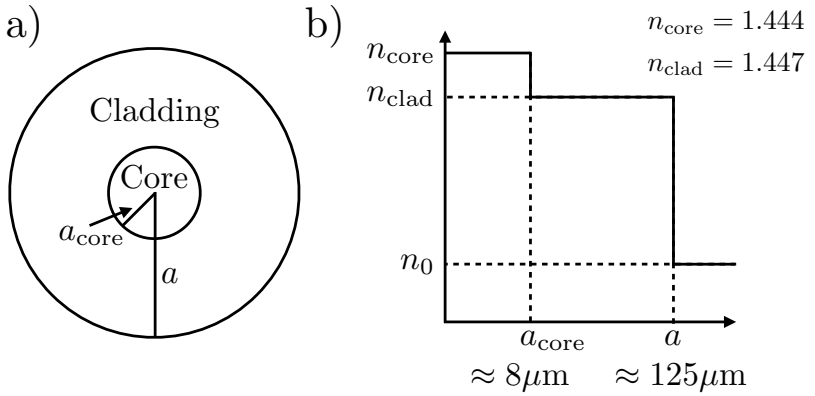


FIGURE 2.2: (a) The cross section of, and (b) the step-index profile of a typical telecommunications fiber. Note that the radius of the core has been exaggerated for illustrative purposes. Typical values of the important parameters have been indicated.

kinetic energy dominates the repulsion due to double occupancy and the system undergoes a transition back to a delocalized superfluid.

2.3 Optical Fiber Background Theory

A standard fiber consists of a core and a surrounding cladding area. The materials are chosen such that a step-index profile results, see Fig. 2.2. A typical material for the cladding is silica (SiO_2) and the core is made from silica doped with germanium ions. This doping leads to a refractive index which is about 1% greater than the refractive index of the cladding, and this difference in turn leads to total internal reflection (TIR) of light coupled into the fiber core, within a certain acceptance angle (or numerical aperture) , and so allows it to be transmitted along the fiber. A telecommunications fiber is typically around 125 μm in diameter, the diameter of the core is usually ten to thirty times smaller than the entire fiber diameter. This is necessary in order to minimize losses at the core-cladding interface when the fiber bends. Laser light can be coupled into a fiber using a number of different and well established coupling techniques. The propagation inside the fiber is then determined by Maxwell's equations, and if they are solved exactly, four individual types of propagating mode can be identified. These are the hybrid modes HE and

EH, which have six non-vanishing contributions to the electromagnetic field, and the transverse modes TE (transverse electric) and TM (transverse magnetic), for which at least one component is vanishing.

2.3.1 Light Propagation in Optical Fibers

The cylindrical symmetry of fibers suggests the use of cylindrical coordinates. We assume that both media, that of the core and that of the cladding, are non-absorbing and that they have a magnetic permeability equal to the vacuum permeability, μ_0. The field components are E_r, E_ϕ, E_z, H_r, H_ϕ, and H_z. Note that since the unit vectors in the r and ϕ directions are not constant vectors, the wave equations for the transverse components becomes complicated, whereas the wave equation for the z components is simply given by

$$(\nabla^2 + k^2)\begin{bmatrix} E \\ H \end{bmatrix} = 0. \tag{2.21}$$

Here $k^2 = \omega^2 n^2/c^2$ is the wave-vector, and ∇^2 is the Laplacian operator

$$\nabla^2 = \frac{\partial^2}{\partial r^2} + \frac{1}{r}\frac{\partial}{\partial r} + \frac{1}{r^2}\frac{\partial^2}{\partial r}. \tag{2.22}$$

The direction of light propagation is along the waveguide, so we assume that every component of the field vector assumes the same z and t dependence of $\mathrm{e}^{i(\omega t - \beta z)}$

$$\begin{bmatrix} \vec{E}(\vec{r},t) \\ \vec{H}(\vec{r},t) \end{bmatrix} = \begin{bmatrix} \vec{E}(r,\phi) \\ \vec{H}(r,\phi) \end{bmatrix} \mathrm{e}^{i(\omega t - \beta z)}. \tag{2.23}$$

Eqs. (2.21) and (2.23) are Maxwell's equations and they can be presented in cylindrical form as (see, for example, [42])

$$\begin{aligned} i\omega\varepsilon E_r &= i\beta H_\phi + \frac{1}{r}\frac{\partial}{\partial\phi}H_z \\ i\omega\varepsilon E_\phi &= -i\beta H_r - \frac{\partial}{\partial r}H_z \\ i\omega\varepsilon E_z &= -\frac{1}{r}\frac{\partial}{\partial\phi}H_r + \frac{1}{r}\frac{\partial}{\partial r}(rH_\phi) \end{aligned} \tag{2.24}$$

$$\begin{aligned} -i\omega\mu H_r &= i\beta E_\phi + \frac{1}{r}\frac{\partial}{\partial\phi}E_z \\ -i\omega\mu H_\phi &= -i\beta E_r - \frac{\partial}{\partial r}E_z \\ -i\omega\mu H_z &= -\frac{1}{r}\frac{\partial}{\partial\phi}E_r + \frac{1}{r}\frac{\partial}{\partial r}(rE_\phi) \end{aligned} \tag{2.25}$$

and are solved by

$$E_r = \frac{-i\beta}{\omega^2\mu\varepsilon - \beta^2}\left(\frac{\partial}{\partial r}E_z + \frac{\omega\mu}{\beta}\frac{\partial}{r\partial\phi}H_z\right) \quad H_r = \frac{-i\beta}{\omega^2\mu\varepsilon - \beta^2}\left(\frac{\partial}{\partial r}H_z - \frac{\omega\varepsilon}{\beta}\frac{\partial}{r\partial\phi}E_z\right)$$

$$E_\phi = \frac{-i\beta}{\omega^2\mu\varepsilon - \beta^2}\left(\frac{\partial}{r\partial\phi}E_z - \frac{\omega\mu}{\beta}\frac{\partial}{\partial r}H_z\right) \quad H_\phi = \frac{-i\beta}{\omega^2\mu\varepsilon - \beta^2}\left(\frac{\partial}{r\partial\phi}H_z + \frac{\omega\varepsilon}{\beta}\frac{\partial}{\partial r}E_z\right). \tag{2.26}$$

(2.27)

So, rather elegantly, it is enough to determine H_z and E_z to fully know the wave solution for every component. Given the assumed z-dependence of eq. (2.23), the wave equation (2.21) becomes

$$\left(\frac{\partial^2}{\partial r^2} + \frac{1}{r}\frac{\partial}{\partial r} + \frac{1}{r^2}\frac{\partial^2}{\partial\phi} + (k^2 - \beta^2)\right)\begin{bmatrix}E_z\\H_z\end{bmatrix} = 0, \tag{2.28}$$

which is separable, with solutions of the form

$$\begin{bmatrix}E_z\\H_z\end{bmatrix} = \begin{bmatrix}\psi_1\\\psi_2\end{bmatrix}\mathrm{e}^{\pm il\phi}, \qquad l = 0, 1, 2... \ . \tag{2.29}$$

From this eq. (2.28) becomes

$$\frac{\partial^2\psi}{\partial r^2} + \frac{1}{r}\frac{\partial\psi}{\partial r} + (k^2 - \beta^2 - \frac{l^2}{r^2})\psi = 0. \tag{2.30}$$

which has solutions called Bessel functions of order l. The general solution of eq. (2.30) is then

$$\psi(r) = c_1 J_l(hr) + c_2 Y_l(hr), \qquad \text{if } k^2 - \beta^2 > 0 \qquad c_1, c_2 \in \mathbb{C}\ . \tag{2.31}$$

$$\psi(r) = c_3 I_l(qr) + c_4 K_l(qr), \qquad \text{if } k^2 - \beta^2 < 0 \qquad c_3, c_4 \in \mathbb{C}\ . \tag{2.32}$$

where the c_n are constants, J_l and Y_l are Bessel functions of the first and second kind respectively, and I_l and K_l are modified Bessel functions of the first and second kind respectively, all of order l. Also, $h^2 = k^2 - \beta^2$ and $q^2 = \beta^2 - k^2$. Here q is an important parameter, as it corresponds to the reciprocal of the decay length Λ of the evanescent field outside the fiber, so that $q = 1/\Lambda$. The evanescent decay length Λ, for a nanofiber of radius $a = 150$ nm, when the light in the fiber has

wavelength $\lambda = 780$ nm is $\Lambda \approx 0.5$ μm, for longer wavelengths the decay length can extend up to 2 μm outside the fiber surface.

The condition that any loss-less mode should be confined to the core, restricts the axial propagation constant β to the range $n_2 k_0 \leq \beta \leq n_1 k_0$, where $k_0 = \omega/c$ is the wave vector of the propagating field. This implies that the solution of eq. (2.30) will take the form of eq. (2.31) inside the core, when $r < a$, and the form of eq. (2.32) outside it, when $r > a$. Since Y_l is singular at $r = 0$, the fields in eq. (2.30) are only finite if $c_2 = 0$. For a loss-less mode the power density is restricted to the fiber and the guided fields must therefore vanish for large r. Because I_l diverges as $r \to \infty$, we require $c_3 = 0$ in order to show an evanescent decay of the field. Inside the core the field components E_z and H_z are then given by

$$\begin{aligned} E_z(r,\phi,z,t) &= AJ_l(hr)\ \mathrm{e}^{i(\omega t \pm l\phi - \beta z)}, \\ H_z(r,\phi,z,t) &= BJ_l(hr)\ \mathrm{e}^{i(\omega t \pm l\phi - \beta z)}, \end{aligned} \tag{2.33}$$

whereas outside the core the have the form

$$\begin{aligned} E_z(r,\phi,z,t) &= CK_l(qr)\ \mathrm{e}^{i(\omega t \pm l\phi - \beta z)}, \\ H_z(r,\phi,z,t) &= DK_l(qr)\ \mathrm{e}^{i(\omega t \pm l\phi - \beta z)}. \end{aligned} \tag{2.34}$$

Using eqs. (2.33) and (2.34), combined with eqs. (2.21), (2.29), and (2.27), the fields E_r, E_ϕ, H_r, and H_ϕ, inside and outside the fiber core can now be expressed in terms of E_z and H_z. Here, for brevity, we restrict ourselves to including only E_r and E_z outside the fiber core ($r > a$). All of the solutions can be found in chapter 3 of [42] and for $r > a$ are given by

$$\begin{aligned} E_r(r,\phi,z,t) = &\ \frac{\beta}{q}\left[iCK_l(qr) - \frac{\omega\mu_0(\pm l)}{\beta}D\frac{K_l qr}{qr}\right]\mathrm{e}^{i(\omega t \pm l\phi - \beta z)}, \\ E_\phi(r,\phi,z,t) = &-\frac{\beta}{q}\left[(\pm l)C\frac{K_l(qr)}{qr} + \frac{i\omega\mu_0}{\beta}DK_l' qr\right]\mathrm{e}^{i(\omega t \pm l\phi - \beta z)}. \end{aligned} \tag{2.35}$$

It is necessary to remember that the tangential components $E_{\phi,z}$ and $H_{\phi,z}$ have to be continuous at the core-cladding boundary, which requires the boundary

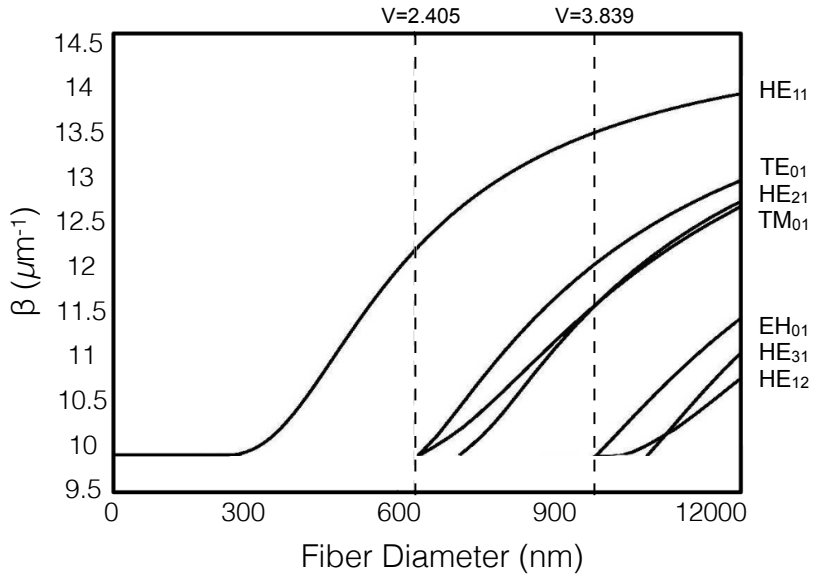


FIGURE 2.3: Numerical solutions of eq. (2.37) for the propagation constant β for a vacuum-clad silica fiber, with light at 852 nm wavelength. The dashed lines indicate the single-mode cut-off, and the first-four-mode cut-off. One can see that the TE_{01} TM_{01} and HE_{21} modes become available at approximately the same radius.

conditions

$$E_{\phi,z}(r=a)|_{\text{core}} = E_{\phi,z}(r=a)|_{\text{cladding}},$$
$$H_{\phi,z}(r=a)|_{\text{core}} = H_{\phi,z}(r=a)|_{\text{cladding}}. \tag{2.36}$$

Combining these with eq. (2.35) and all of its accompanying expressions (for E_r, E_ϕ, E_z, H_r, H_ϕ, and H_z inside and outside the fiber core), then leads to the mode condition that can be solved numerically to find the propagation constant β of each mode, and also to determine the number of modes allowed to propagate in the fiber. This mode condition is given by

$$\left(\frac{J_l'(ha)}{haJ_l(ha)}+\frac{K_l'(qa)}{qaK_l(qa)}\right)\left(\frac{n_1^2J_l'(ha)}{haJ_l(ha)}+\frac{n_2^2K_l'(qa)}{qaK_l(qa)}\right) = l^2\left[\left(\frac{1}{qa}\right)^2+\left(\frac{1}{ha}\right)^2\right]^2\left(\frac{\beta}{k_0}\right)^2, \tag{2.37}$$

where again

$$h = \sqrt{k_0^2 n_1^2 - \beta^2}\,, \tag{2.38}$$

$$q = \sqrt{\beta^2 - k_0^2 n_2^2}\,. \tag{2.39}$$

and the wavenumber in free space is $k_0 = 2\pi/\lambda$. The dashed functions, $J'(x)$ and $K'(x)$, represent a derivative with respect to the argument. The numerical solutions of eq. (2.37) are shown in Fig. 2.3. By solving eq. (2.37) for $J_l'(ha)/haJ_l(ha)$, using the Bessel relations

$$J_l'(x) = -J_{l+1}(x) + \frac{l}{x}J_l(x) \quad \text{and} \quad J_l'(x) = J_{l-1}(x) - \frac{l}{x}J_l(x)$$

it is possible to identify different sets of solutions that correspond to different modes. In the case where $l = 0$ it is possible to arrive at simplified mode conditions for the TM and TE modes (i.e. when $\partial/\partial\phi = 0$ and all the components are radially symmetric). These simplified mode equations will be given where they are relevant in Sec. 2.6.

2.3.2 A Note About TM, TE and Hybrid Modes.

The exact solutions for the bound field modes are usually divided into two subgroups: hybrid modes and transverse modes. The hybrid modes contain both electric (E) and magnetic (H) field components along the fiber axis and are denoted HE (EH) when E_z is smaller (larger) than H_z. For the transverse modes, the longitudinal component of either the electric or magnetic field is zero and the modes are thus said to be transverse electric (TE) or transverse magnetic (TM). In other words, TE modes have only H (magnetic field) components in the direction of propagation and TM modes have only E components in the direction of propagation.

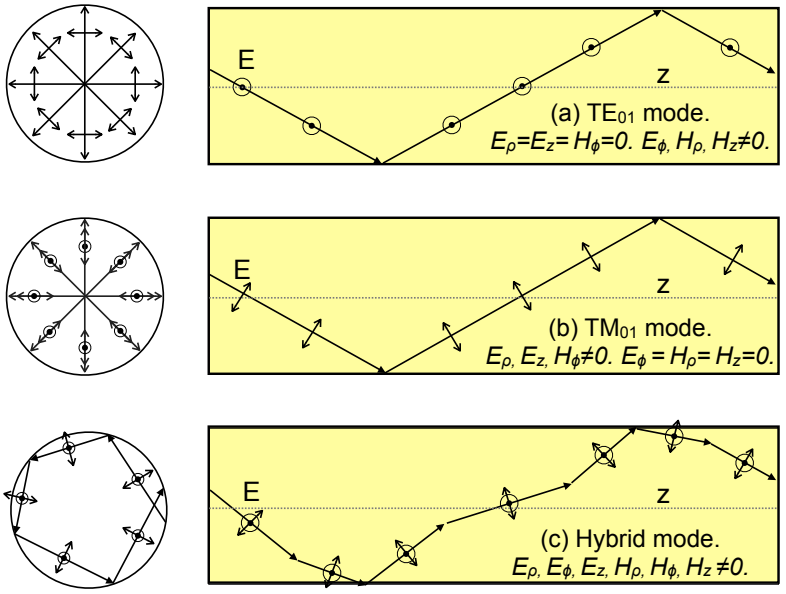


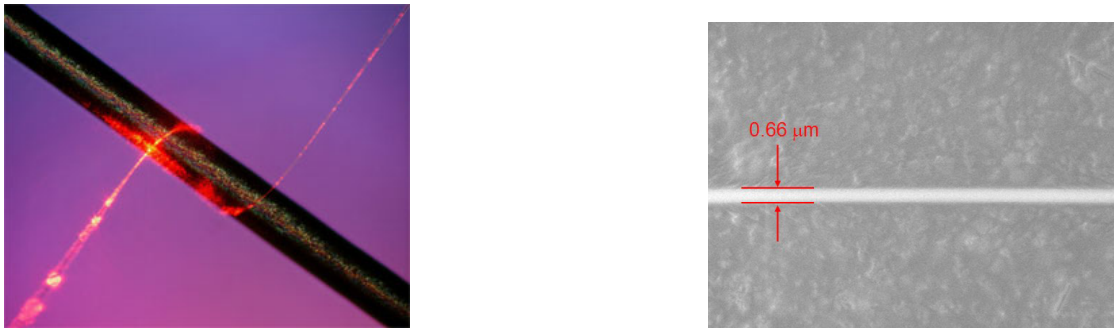
FIGURE 2.4: Note that only the vertical light rays are shown in the longitudinal cross-section for (a) and (b), while several directions are contained in the transverse cross-section. This figure is recreated from [43] where it appears as Fig. 2-11, a similar figure appears as Fig. 11-2 in [44].

It is helpful to consider the schematic light ray drawings shown in Fig. 2.4. The transverse modes always intersect the fiber axis effectively causing either the electric (a) or magnetic (b) field to be purely transverse. The TE_{01} only has circular fields lines for the electric field, while the TM_{01} electric field lines are perpendicular and parallel to the fiber axis. In contrast to the transverse modes, the hybrid modes circulate around the fiber axis without ever passing through it. This is what gives rise to the non-zero components of both the electric and magnetic field in all directions. The HE_{11} mode is a hybrid, it is neither TE (transverse electric) nor TM (transverse magnetic) because the axial field components E_z and H_z are not zero [42].

2.4 Tapered Optical Nanofibers

Tapered nanofibers are sub-wavelength diameter optical fibers with a cylindrical silica core. Tapered fibers can be created by heating and pulling commercial

grade optical fiber and tapering, so that the refractive indices that determine the guiding properties of the fiber are that of the original silica cladding and that of the surrounding vacuum [13]. Throughout the tapering process the transition from the untapered region to the tapered region must remain adiabatic to avoid losses, some images of tapered fibers are shown in Fig. 2.5. Current tapered fiber technology can produce fibers with radii as low as a few hundred nanometres [14, 45–47] and such thin fibers can only support a finite number of modes. Due to the tapering process, the original core has vanished and the refractive indices that determine the guiding properties of the tapered fiber are those of the original silica cladding and of the surrounding vacuum (see Fig. 2.6). In this case, there exists a pronounced evanescent field that penetrates into the free-space surrounding the fiber. The shape of this evanescent field is characteristic of the fiber properties and the properties of the guided light. In particular it can be used for trapping and manipulating atoms at sub-micrometer distances from the fiber surface.



(a) (b)

FIGURE 2.5: (a) The thicker line is a human hair and wrapped around it is a tapered optical fiber, from the Mazur group at Harvard, see *www.mazur.harvard.edu/research/*. (b)This picture is the tapered part of an optical fiber of radius 330 nm. From the group of Síle Nic Chormaic at OIST, Okinawa, Japan.

Atoms can be trapped and guided by the gradient force of a light field, see Sec. 2.1. When light is incident at a boundary between two media, the refracted field does not drop instantaneously to zero, but rather decays quasi-exponentially on the



FIGURE 2.6: As the fiber is pulled the core essentially vanishes, the cladding becomes the new guiding area and the surrounding vacuum acts as an infinite cladding.

length-scale of the field's wavelength. This is called the evanescent field. Evanescent light fields are particularly interesting because they provide high spatial gradients and a well-defined potential shape which is dependent on the shape of the dielectric surface from which they originate. However, usually the power and the range of the evanescent field are small. A system where the intensity of the evanescent field is a significant portion of the overall intensity of the wave is therefore desireable. Tapered optical fibers allow access to this scenario by having fiber diameters so small that a large portion of the field intensity is no longer guided in the fiber core, but instead in the evanescent region.

Among the particularly desirable qualities of tapered optical fibers are therefore their strong transverse confinement properties and the pronounced evanescent field they exhibit. Several works have already been undertaken that show how these properties can be used [48]. For example, experimental work has demonstrated how the evanescent field can efficiently probe and couple atoms and molecules to the fiber mode [17, 49, 50], which opens the possibility of a range of applications for the detection and manipulation of these particles. In particular, evanescent field spectroscopy of a small number of atoms in the vicinity of a tapered optical fiber (TOF) has been performed [49, 51, 52] and the use of the evanescent field for trapping atoms has also been proposed and achieved [16, 17, 50, 52]. Another useful property of such tapered optical nanofibers is that the field distributions can exhibit a cylindrical asymmetry depending on the polarization of the light [53, 54].[1]

[1] In particular, in the case of the fundamental mode with quasi-linear polarization, it has been shown that a substantial azimuthal dependence of the total intensity is observed in the vicinity of the fiber surface [53, 54], this will be discussed later in Sec. 2.5.1.

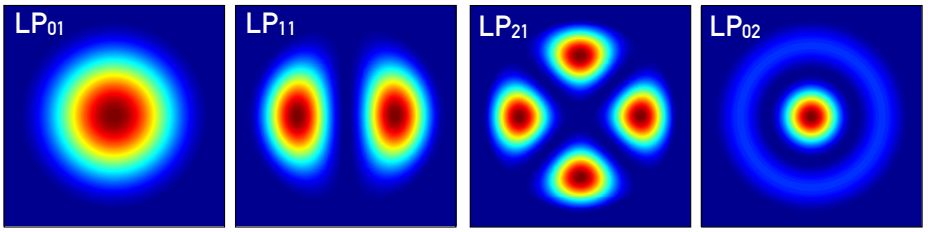


FIGURE 2.7: The intensity distribution of the first four LP modes for $\lambda = 700$ nm laser light in a fiber of radius $a = 1\,\mu$m. Each square corresponds to 2.5 μm $\times$ 2.5 μm. The color scale varies between low intensity (blue) and high intensity (red).

At this point it is important to mention the significance of linearly polarized (LP) modes, as references to them appear throughout the fiber literature. The refractive-index difference, $n_1 - n_2$, in a communications grade fiber is of the order of 1%, which allows the approximation $n_2/n_1 \approx 1$ and enables a very simplified analysis of optical fibers. Where this approximation applies it is a very powerful tool that gives clear results. Mode expressions arrived at through making this approximation are referred to as LP modes. Since an LP mode is derived by the approximation $n_2/n_1 \approx 1$, it is called the weakly guiding approximation. When the fiber is very thin and the silica cladding is replaced by air, the large difference in refractive index between the silica core and the vacuum cladding means that the fiber becomes strongly guiding and the approximation does not apply. A significant z-component develops and the modes can no longer be regarded as mainly transversal. It becomes necessary to solve Maxwell's equations exactly, as we have described in the previous sections. The exact modes can still be grouped according to the LP modes but are no longer degenerate.

The first four LP modes are shown in Fig. 2.7. The LP modes are linear combinations of the exact modes, grouped as follows:

$$\begin{aligned} &\mathrm{LP}_{0,m} : \mathrm{HE}_{1,m} \\ &\mathrm{LP}_{1,m} : \mathrm{HE}_{2,m}, \mathrm{TE}_{0,m}, \mathrm{TM}_{0,m} \\ &\mathrm{LP}_{l,m} : \mathrm{HE}_{l+1,m}, \mathrm{EH}_{l-1,m}, \text{ for } l \geq 2. \end{aligned} \tag{2.40}$$

As an example we consider the modes shown in Fig. 2.8. Here the TE_{01} and HE_{21}

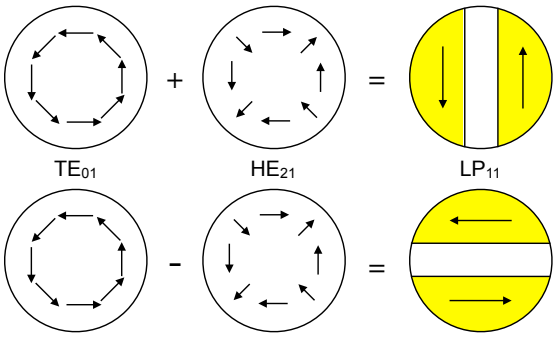


FIGURE 2.8: Two different linear combinations of the TE_{01} and HE_{21} modes combine to form the LP_{11} mode in two different polarization and spatial configurations. Since we are only looking at the transverse polarization in the fiber, the z-component of the hybrid mode does not enter. This figure is recreated from [43] where it appears as Fig. 2-12, a similar figure appears as Fig. 14-5(d) in [44].

modes are combined to make the $LP_{11} = TE_{01} \pm HE_{21}$ mode for two different spatial and polarization configurations. The yellow shaded regions indicate the intensity distribution similar to what is shown in Fig. 2.7. Two more polarization configurations exist for the LP_{11} mode. These are obtained by combining the TM_{01} and HE_{21} modes and give similar intensity distributions to the ones shown but with the polarization lines rotated by 90 degrees. Like the LP modes, each exact mode is characterized by its propagation constant β. The intensity distributions, and polarizations of the first four nanofiber modes, HE_{11}, HE_{21}, TE_{01} and TM_{01}, are shown in Fig. 2.9.

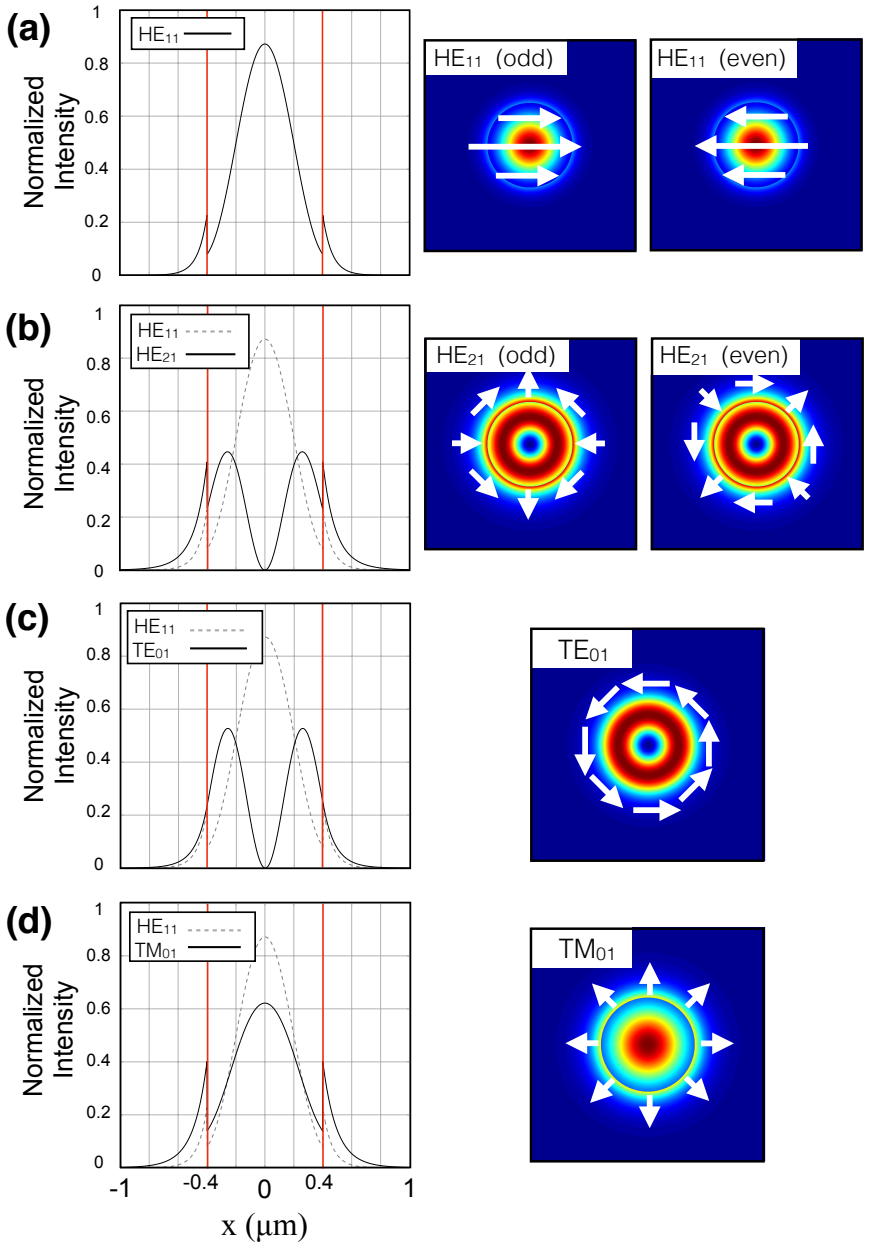


FIGURE 2.9: Intensity distribution of the first four nanofiber modes. The vertical red lines in the first panel on the left indicate the position of the nanofiber surface. In the panels on the right hand side, the arrows indicate the polarization direction. These images were produced for a fiber of radius 400 nm, and lights of wavelength 780 nm. For these parameters, only the first four modes are allowed to propagate in the fiber. Row (a) is the HE_{11} mode, row (b) shows the HE_{21} mode, row (c) is the TE_{01} mode and row (d) is the TM_{01} mode.

Frequently during this thesis we want to ensure that only the fundamental mode HE_{11} travels in the fiber. To guarantee this we choose parameters such that they

satisfy the single-mode condition as indicated in Fig. 2.3, see [42, 44]

$$V = ka\sqrt{n_1^2 - n_2^2} < V_c \cong 2.405, \tag{2.41}$$

where V_c is the single mode cut-off. We will also be interested in the regime where the first four modes, HE_{11}, TE_{01}, TM_{01}, and HE_{21}, are the only modes available in the fiber, which is guaranteed when $2.405 < V < 3.839$. I will now describe these four modes. Throughout this thesis, the refractive index and the radius of the tapered silica waist will be referred to as n_1 and a, respectively.

2.5 The Fundamental Mode HE_{11}

The first fiber mode we will consider is the fundamental mode HE_{11}. As described at the end of Sec. 2.3.1, by solving eq. (2.37) for $J_l'(ha)/haJ_l(ha)$, using the Bessel relations (eq. (2.40)) we can re-frame the mode equation, eq. (2.37), for the different families of solutions corresponding to the various modes. For the HE_{11} mode, β is determined from

$$\begin{aligned}\frac{J_0(ha)}{haJ_1(ha)} = &- \frac{n_1^2 + n_2^2}{2n_1^2}\frac{K_1'(qa)}{qaK_1(qa)} + \frac{1}{h^2a^2} \\ &- \left[\left(\frac{{n_1}^2 + {n_2}^2}{2{n_1}^2}\frac{{K_1}'(qa)}{qaK_1(qa)}\right)^2 + \frac{\beta^2}{{n_1}^2k^2}\left(\frac{1}{q^2a^2} + \frac{1}{h^2a^2}\right)^2\right]^{\frac{1}{2}},\end{aligned} \tag{2.42}$$

which, when solved numerically, gives a set of β values corresponding to the HE propagation modes.

2.5.1 The Fundamental HE_{11} Mode With Quasi-Linear Polarization

Let us first describe the fundamental mode with quasi-linear polarization. Following Sec. 2.3.1, the solutions of Maxwell's equations in cylindrical coordinates

(r, ϕ, z) for the electric field $\vec{E}$ for this mode inside the dielectric fiber ($r < a$) are given by [42]

$$
\begin{aligned}
E_x(r,\phi,z;t) &= -iA\frac{\beta}{2h}\left[(1-s)J_0(hr)\cos(\phi_0) - (1+s)J_2(hr)\cos(2\phi-\phi_0)\right]e^{i(\omega t-\beta z)},\\
E_y(r,\phi,z;t) &= -iA\frac{\beta}{2h}\left[(1-s)J_0(hr)\sin(\phi_0) - (1+s)J_2(hr)\sin(2\phi-\phi_0)\right]e^{i(\omega t-\beta z)},\\
E_z(r,\phi,z;t) &= AJ_1(hr)\cos(\phi-\phi_0)e^{i(\omega t-\beta z)}.
\end{aligned}
\tag{2.43}
$$

Outside of the fiber ($r > a$) they are given by [42]

$$
\begin{aligned}
E_x(r,\phi,z;t) &= A\frac{\beta}{2q}\frac{J_1(ha)}{K_1(qa)}\left[(1-s)K_0(qr)\cos(\phi_0) + (1+s)K_2(qr)\cos(2\phi-\phi_0)\right]e^{i(\omega t-\beta z)},\\
E_y(r,\phi,z;t) &= A\frac{\beta}{2q}\frac{J_1(ha)}{K_1(qa)}\left[(1-s)K_0(qr)\sin(\phi_0) + (1+s)K_2(qr)\sin(2\phi-\phi_0)\right]e^{i(\omega t-\beta z)},\\
E_z(r,\phi,z;t) &= iA\frac{J_1(ha)}{K_1(qa)}K_1(qr)\cos(\phi-\phi_0)e^{i(\omega t-\beta z)},
\end{aligned}
\tag{2.44}
$$

where s is defined as

$$
s = \left[\frac{1}{(ha)^2} + \frac{1}{(qa)^2}\right]\left[\frac{J_1'(ha)}{haJ_1(ha)} + \frac{K_1'(qa)}{qaK_1(qa)}\right]^{-1}, \tag{2.45}
$$

and h and q are as before in eqs. (2.38) and (2.39).

The polarization direction of the transverse electric field is defined by ϕ_0, with x-polarization given when $\phi_0 = 0$ and y-polarization for $\phi_0 = \pi/2$. The normalization constant for the modes is given by A and is directly proportional to the square root of the total power, P.

For practical applications, such as trapping of atoms by the optical force of an evanescent wave around a thin fiber, it is necessary to calculate the optical potential which is proportional to the total intensity $|E|^2$ of the electric field. Here

these are given, inside and outside the fiber, by [42, 49]

$$|\vec{E}_{\rm in}(r,\phi)|^2 = A^2\frac{\beta^2}{4h^2}\Bigg[(1-s)^2J_0^2(hr)+(1+s)^2J_2^2(hr)+2\frac{h^2}{\beta^2}J_1^2(hr) + 2\left(\frac{h^2}{\beta^2}J_1^2(hr)-(1+s)(1-s)J_0(hr)J_2(hr)\right)\cos[2(\phi-\phi_0)]\Bigg], \tag{2.46}$$

$$|\vec{E}_{\rm out}(r,\phi)|^2 = A^2\frac{\beta^2}{4q^2}\frac{J_1^2(ha)}{K_1^2(qa)}\Bigg[(1-s)^2K_0^2(qr)+(1+s)^2K_2^2(qr)+2\frac{q^2}{\beta^2}K_1^2(qr) + 2\left(\frac{q^2}{\beta^2}K_1^2(qr)+(1+s)(1-s)K_0(qr)K_2(qr)\right)\cos[2(\phi-\phi_0)]\Bigg]. \tag{2.47}$$

For simplicity let us introduce the following parameters to rescale the above equations

$$u = 2h^2/(\beta^2(1-s)^2)\,, \tag{2.48}$$

$$w = 2q^2/(\beta^2(1-s)^2)\,, \tag{2.49}$$

$$f = (1+s)^2/(1-s)^2\,, \tag{2.50}$$

$$\xi = 2(1+s)/(1-s)\,, \tag{2.51}$$

so that we obtain

$$|\vec{E}_{\rm in}|^2 = G_{\rm in}[J_0^2(hr)+uJ_1^2(hr)+fJ_2^2(hr) + [uJ_1^2(hr)-\xi J_0(hr)J_2(hr)]\cos[2(\phi-\phi_0)]], \tag{2.52}$$

$$|\vec{E}_{\rm out}|^2 = G_{\rm out}[K_0^2(qr)+wK_1^2(qr)+fK_2^2(qr) + [wK_1^2(qr)+\xi K_0(qr)K_2(qr)]\cos[2(\phi-\phi_0)]], \tag{2.53}$$

where $G_{\rm in} = \frac{|A|^2}{2u}$ and $G_{\rm out} = \frac{|A|^2J_1^2(ha)}{(2wK_1^2(qa))}$. In each of the eqs. (2.52) and (2.53), the initial terms, proportional to $J_0^2(hr)$ and $K_0^2(qr)$ respectively, represent the total intensity of the electric field in the $\rm LP_{01}$ mode. On their own, these terms are a good approximation of the full $\rm HE_{11}$ mode, a simplification often made by those working with standard telecommunications fibers. Typical values of the

parameters that appear here will be discussed later in Sec. 2.8.1.

The above expressions for the HE_{11} mode are valid for any core radius a and any pair of refractive indices n_1 and n_2 as long as $n_1 > n_2$. As indicated above, in conventional single-mode fibers where $\Delta \equiv (n_1 - n_2)/n_1 \ll 1$ and $a > \lambda$ one can make the additional approximation $s = -1 + (qa/V)^2[haJ_0(ha)/J_1(ha)]\Delta + O(\Delta^2) \approx -1$ which leads to the ϕ-dependent terms containing $(1+s)J_2(hr)$ and $(1+s)K_2(qr)$ becoming negligible. Hence, the transverse component will be zero if $\phi_0 = 0$ or $\phi_0 = \pi/2$, respectively. In addition we find $h, q \ll \beta$, which means that the longitudinal component E_z is small as well. The exact HE_{11} mode with quasi-linear polarization of a conventional weakly guiding fiber can thus be approximated by an LP_{01} mode [42, 55].

The electric field in the LP_{01} mode is given by

$$\vec{E} = AJ_0(hr)\ \hat{\mathbf{e}}\ e^{i(\omega t - \beta z)} \qquad \text{for } r < a \tag{2.54}$$

$$\vec{E} = A\frac{J_0(ha)}{K_0(qa)}K_0(qr)\ \hat{\mathbf{e}}\ e^{i(\omega t - \beta z)} \qquad \text{for } r > a \tag{2.55}$$

where the polarization vector $\hat{\mathbf{e}}$ can be assigned as $\hat{\mathbf{e}} = \hat{\mathbf{x}}$ or $\hat{\mathbf{e}} = \hat{\mathbf{y}}$.

In the field expressions for the LP_{01} mode above, the transverse profiles of $|E_x|^2$ and $|E_y|^2$ are indistinguishable and the polarization of the field is almost completely linear. Hence, the intensity distribution is cylindrically symmetric. In the case of sub-wavelength diameter nanofibers, neither of the relations $\Delta \ll 1$ and $a > \lambda$ are satisfied. For nanofibers, the factor $(1 + s)$ is not negligible and the decay parameter qa can become sufficiently small so that both $K_1(qa)$ and $K_2(qa)$ are much larger than $K_0(qa)$. As a result, the terms with $K_1(qr)$ and $K_2(qr)$ in the expression of eqs. (2.44), can be large in the vicinity of the fiber surface. When $K_1(qr)$ is large, the longitudinal component E_z outside the fiber can also become significant, and when $K_2(qr)$ is large the terms with azimuthal dependence, that is $\cos(2\phi - \phi_0)$ and $\sin(2\phi - \phi_0)$, can become significant. These terms lead to an azimuthal dependence of the field intensity outside the fiber. In addition, when qa is small and the refractive index difference is large, then the parameter h may

become comparable with, or even larger than, β. Then, the component E_z of the field where $r < a$ may also become non-negligible compared to E_ϕ and E_r, see eqs. (2.43). So, there can be a significant z component E_z both inside $r < a$ and outside $r > a$ the fiber surface, and one can see that characteristics of the exact fundamental mode HE_{11} can become very different from the linearly polarized mode LP_{01} [55].

2.5.2 The Fundamental HE_{11} Mode With Circular Polarization

Let us next investigate the electric field equations for the fundamental HE_{11} mode with circular polarization. Its components inside the fiber ($r < a$) are given by

$$\begin{aligned} E_r(r,\phi,z;t) &= -iA\frac{\beta}{2h}\left[(1-s)J_0(hr) - (1+s)J_2(hr)\right]e^{i(\omega t \pm \phi - \beta z)}\,, \\ E_\phi(r,\phi,z;t) &= \pm A\frac{\beta}{2h}\left[(1-s)J_0(hr) - (1+s)J_2(hr)\right]e^{i(\omega t \pm \phi - \beta z)}\,, \\ E_z(r,\phi,z;t) &= AJ_1(hr)e^{i(\omega t \pm \phi - \beta z)}\,, \end{aligned} \tag{2.56}$$

and outside the fiber ($r > a$) by

$$\begin{aligned} E_r(r,\phi,z;t) &= -iA\frac{\beta}{2q}\frac{J_1(ha)}{K_1(qa)}\left[(1-s)K_0(qr) + (1+s)K_2(qr))\right]e^{i(\omega t \pm \phi - \beta z)}\,, \\ E_\phi(r,\phi,z;t) &= \pm A\frac{\beta}{2q}\frac{J_1(ha)}{K_1(qa)}\left[(1-s)K_0(qr) - (1+s)K_2(qr))\right]e^{i(\omega t \pm \phi - \beta z)}\,, \\ E_z(r,\phi,z;t) &= A\frac{J_1(ha)}{K_1(qa)}K_1(qr)e^{i(\omega t \pm \phi - \beta z)}\,. \end{aligned} \tag{2.57}$$

Here the parameters s, h and q are defined in the same way as for linear polarization given earlier by equations (2.45), (2.38) and (2.39), respectively.

The $\pm$ in the field equations indicates the direction of polarization around the fiber axis ($+$ indicates clockwise and $-$ indicates counterclockwise). The normalization constant is again given by A and is proportional to the square root of the input power of the coupled light fields.

The absolute value of the field intensity in the HE_{11} mode averaged over one oscillation period is then given by [55]

$$|\vec{E}_{\rm in}(r)|^2 = A^2 \frac{\beta^2}{2h^2}\left[(1-s)^2 J_0^2(hr) + (1+s)^2 J_2^2(hr) + 2\frac{h^2}{\beta^2} J_1^2(hr)\right] , \tag{2.58}$$

$$|\vec{E}_{\rm out}(r)|^2 = A^2 \frac{\beta^2}{2q^2}\frac{J_1^2(ha)}{K_1^2(qa)}\left[(1-s)^2 K_0^2(qr) + (1+s)^2 K_2^2(qr) + 2\frac{q^2}{\beta^2} K_1^2(qr)\right] . \tag{2.59}$$

Since there is no ϕ dependence here the resultant distribution of $|\vec{E}(r)|^2$ is cylindrically symmetric. The functions E_j are also independent of the azimuthal angle ϕ_0. Hence, the intensities $|E_j|^2$ of the cylindrical-coordinate components of the field are independent of ϕ_0, and so is the total intensity $|E|^2$ of the electric field. We can easily calculate the total intensity $|E|^2$ of the electric field in a fundamental mode with rotating polarization. For the field inside the fiber, having been rescaled as in the previous section, we obtain

$$|\vec{E}_{\rm in}|^2 = 2G_{\rm in}[J_0^2(hr) + uJ_1^2(hr) + fJ_2^2(hr)], \tag{2.60}$$

and for the field outside the fiber, we get

$$|\vec{E}_{\rm out}|^2 = 2G_{\rm out}[K_0^2(qr) + wK_1^2(qr) + fK_2^2(qr)]. \tag{2.61}$$

The terms $J_0^2(hr)$ and $K_0^2(qr)$ in the expressions (2.60) and (2.61), respectively, correspond to the total intensity of the electric field in the mode LP_{01}. The other terms describe the deviations of the exact fundamental mode HE_{11} with rotating polarization from the approximate mode LP_{01}. The total intensity of the electric field in a fundamental mode with rotating polarization is the sum of the corresponding intensities for two constituent modes with quasi-linear polarizations. The ϕ_0-dependent terms cancel each other and therefore do not appear in eqs. (2.60) and (2.61). The intensity distribution, and polarization direction of the HE_{11} mode are shown in row (a) of Fig. 2.9.

The above expressions are mathematically valid for the fundamental mode with

rotating polarization of a fiber with an arbitrary core radius a and an arbitrary pair of refractive indices $n_1 > n_2$.

It is therefore clear that the small radius of the fiber and the high contrast between the refractive indices of the silica core and the vacuum clad substantially modify the intensity distributions and the polarization properties of the field and its components, especially in the vicinity of the fiber surface. A substantial azimuthal dependence of the total intensity is observed in the vicinity of the fiber surface for linear polarizations which is not present if the fundamental mode has circulating polarization [53, 54]. The difference between the exact and approximate modes is relatively small in the case of rotating polarization [54]. Consequently, the underlying physics of the optical potential of the evanescent wave around a vacuum-clad subwavelength-diameter fiber is basically the same as that of the approximate mode LP_{01}. However, the difference of the magnitude in the vicinity of the fiber surface is not negligible. Therefore, the use of the exact solutions of Maxwell's equations is required in a systematic quantitative treatment for a thin fiber.

2.6 The First Three Higher Order Guided Modes

Modal dispersion occurs when there is more than one mode present in a fiber. In the telecommunications industry this effect is a hindrance since it leads to lower transfer efficiency. In this thesis, particularly in Chapter 4, we examine how tailoring the interference between different modes might be used to engineer atom traps. As the fiber radius increases, the higher order modes TE_{01}, TM_{01}, and HE_{21} appear in the fiber at almost the same radius, see Fig. 2.3. In this thesis, we never consider more than the first four modes. The fundamental HE_{11} mode has been discussed already in Sec. 2.5 and the expressions for the electric field components for the TE_{01}, TM_{01}, and HE_{21} modes are given in the following subsections.

2.6.1 The HE_{21} Mode

Again, as described at the end of Sec. 2.3.1, in the case where $l = 0$ we can reframe the mode equation (eq. (2.37)) for the HE family of solutions. For the HE_{21} mode, β is determined from

$$\begin{aligned}\frac{J_1(ha)}{haJ_2(ha)} =& -\frac{(n_1^2+n_2^2)}{2n_1^2}\frac{K_2'(qa)}{qaK_2(qa)} + \frac{2}{h^2a^2} \\ & - \frac{(n_1^2-n_2^2)}{n_1^2}\left[\left(\frac{K_2'(qa)}{2qaK_2(qa)}\right)^2 + \left(\frac{2n_1k\beta}{a^2h^2q^2}\right)^2\right]^{1/2},\end{aligned} \tag{2.62}$$

and the mode functions of the electric parts of the fundamental guided mode HE_{21} [56] for $r < a$ are given by

$$\begin{aligned}E_r &= A_{21}\frac{i\beta}{2h}[(1-u)J_1(hr) - (1+u)J_3(hr)], \\ E_\phi &= -A_{21}\frac{\beta}{2h}[(1-u)J_1(hr) + (1+u)J_3(hr)], \\ E_z &= A_{21}J_1(hr),\end{aligned} \tag{2.63}$$

and for $r > a$, by

$$\begin{aligned}E_r &= A_{21}\frac{i\beta}{2q}\frac{J_2(ha)}{K_2(qa)}[(1-u)K_1(qr) + (1+u)K_3(qr)], \\ E_\phi &= -A_{21}\frac{\beta}{2q}\frac{J_2(ha)}{K_2(qa)}[(1-u)K_1(qr) - (1+u)K_3(qr)], \\ E_z &= A_{21}\frac{J_2(ha)}{K_2(qa)}K_2(qr).\end{aligned} \tag{2.64}$$

Again, for simplicity, some of the constant parameters have been tidied into u, A, R_1 and R_2, such that

$$u = \frac{2\Big(1/h^2a^2 + 1/q^2a^2\Big)}{J_2'(ha)/haJ_2(ha) + K_2'(qa)/qaK_2(qa)}, \tag{2.65}$$

$$A = \frac{1}{\sqrt{\pi}a\sqrt{{n_1}^2R_1 + {n_2}^2R_2}}, \tag{2.66}$$

$$R_1 = {J_2}^2(ha) - J_1(ha)J_3(ha) + \frac{\beta^2}{2h^2}\Big[(1-u)^2({J_1}^2(ha) - J_0(ha)J_2(ha)) + (1+u)^2({J_3}^2(ha) - J_2(ha)J_4(ha))\Big], \tag{2.67}$$

and

$$R_2 = \frac{{J_2}^2(ha)}{{K_2}^2(qa)}\Bigg\{K_1(qa)K_3(qa) - {K_2}^2(qa) + \frac{\beta^2}{2q^2}\left[(1-u)^2(K_0(qa)K_2(qa) - {K_1}^2(qa)) + (1+u)^2(K_2(qa)K_4(qa) - {K_3}^2(qa))\right]\Bigg\}. \tag{2.68}$$

The intensity distribution, and polarization of the HE_{21} mode is shown in row (b) of Fig. 2.9.

2.6.2 The TE_{01} Mode

Again, as described at the end of Sec. 2.3.1, in the case where $l = 0$ we can reframe the mode equation (eq. (2.37)) for the TE family of solutions and find that for the TE_{01} mode, β is determined from

$$\frac{J_1(ha)}{haJ_0(ha)} = -\frac{K_1(qa)}{qaK_0(qa)}. \tag{2.69}$$

The mode functions of the electric parts of the fundamental guided mode TE_{01} [56] for $r < a$ are given by

$$\begin{aligned} E_r &= 0, \\ E_\phi &= \frac{i}{\sqrt{\pi}ha^2}\frac{K_0(qa)/J_0(ha)}{\sqrt{{n_1}^2P_1 + {n_2}^2P_2}}J_1(hr), \\ E_z &= 0, \end{aligned} \tag{2.70}$$

and for $r > a$

$$\begin{aligned} E_r &= 0, \\ E_\phi &= -\frac{i}{\sqrt{\pi} q a^2} \frac{K_1(qr)}{\sqrt{{n_1}^2 P_1 + {n_2}^2 P_2}}, \\ E_z &= 0, \end{aligned} \tag{2.71}$$

where, for simplicity, some of the constant parameters have been tidied into P_1 and P_2, such that

$$P_1 = \frac{1}{a^2 h^2} \frac{{K_0}^2(qa)}{{J_0}^2(ha)} \Big({J_1}^2(ha) - J_0(ha) J_2(ha) \Big), \tag{2.72}$$

$$P_2 = \frac{1}{a^2 q^2} \Big(K_0(qa) K_2(qa) - {K_1}^2(qa) \Big). \tag{2.73}$$

The intensity distribution, and polarization of the TE_{01} mode is shown in row (c) of Fig. 2.9.

2.6.3 The TM_{01} Mode

For the TM_{01} mode, β is determined from

$$\frac{J_1(ha)}{ha J_0(ha)} = -\frac{n_2^2}{n_1^2} \frac{K_1(qa)}{qa K_0(qa)} \tag{2.74}$$

and the mode functions of the electric parts of the fundamental guided mode TM_{01} [56] for $r < a$ are given by

$$\begin{aligned} E_r &= -\frac{i\beta}{\sqrt{\pi} h a} \frac{K_0(qa)/J_0(ha)}{\sqrt{{n_1}^2 Q_1 + {n_2}^2 Q_2}} J_1(hr), \\ E_\phi &= 0, \\ E_z &= -\frac{1}{\sqrt{\pi} a} \frac{K_0(qa)/J_0(ha)}{\sqrt{{n_1}^2 Q_1 + {n_2}^2 Q_2} K_0(qr)}, \end{aligned} \tag{2.75}$$

and for $r > a$

$$\begin{aligned} E_r &= -\frac{i\beta}{\sqrt{\pi}qa}\frac{1}{\sqrt{{n_1}^2Q_1 + {n_2}^2Q_2}}K_1(qr), \\ E_\phi &= 0, \\ E_z &= -\frac{1}{\sqrt{\pi}a}\frac{1}{\sqrt{{n_1}^2Q_1 + {n_2}^2Q_2}}K_0(qr). \end{aligned} \tag{2.76}$$

Here, for simplicity, some of the constant parameters have been tidied into Q_1 and Q_2, such that

$$Q_1 = \frac{{K_0}^2(qa)}{{J_0}^2(ha)}\left[{J_0}^2(ha) + \frac{{n_1}^2k^2}{h^2}{J_1}^2(ha) - \frac{\beta^2}{h^2}J_0(ha)J_2(ha)\right], \tag{2.77}$$

$$Q_2 = \frac{\beta^2}{q^2}K_0(qa)K_2(qa) - {K_0}^2(qa) - \frac{{n_2}^2k^2}{q^2}{K_1}^2(qa). \tag{2.78}$$

The intensity distribution, and polarization of the TM_{01} mode is shown in row (d) of Fig. 2.9.

2.7 Atom-Surface Interactions

An atom near the surface of a dielectric medium experiences a force due to the van der Waals interaction, which is an induced dipole-dipole interaction. As we are interested in fields close to the surface of the fiber, this usually attractive force between the atom and the surface has a significant effect and has to be taken into account in our calculations. The van der Waals potential acting on an atom near the surface of a dielectric fiber of infinite length can be written as [16, 57]

$$V^c_{\mathrm{vdW}}(r) = \frac{\hbar}{4\pi^3\epsilon_0}\sum_{n=-\infty}^{\infty}\int_0^\infty dk\,[k^2K_n'^2(kr)+(k^2+n^2/r^2)K_n^2(kr)]\int_0^\infty d\xi\,\alpha(i\xi)G_n(i\xi), \tag{2.79}$$

where

$$G_n(\omega) = \frac{[\epsilon(\omega)-\epsilon_0]I_n(ka)I_n'(ka)}{\epsilon_0 I_n(ka)K_n'(ka) - \epsilon(\omega)I_n'(ka)K_n(ka)}\,. \tag{2.80}$$

Here ϵ_0 is the dielectric constant in a vacuum. The dynamical dielectric function of silica is given by multiplying eq. (2.91) (given later in Sec. 2.8.1) by ϵ_0 so that

$$\epsilon(\omega) = \epsilon_0 n_1 \ . \tag{2.81}$$

When the fiber radius a is very large compared to the atom-to-surface distance D, the expression for the van der Waals potential, $V_{\rm vdW}$ near a curved surface, given in eq. (2.79) tends to the simpler form of the potential for an atom close to a flat dielectric surface

$$V^f_{\rm vdW} = -\frac{C_3}{(r-a)^3} \ , \tag{2.82}$$

where C_3 is a van der Waals constant. In [16] it was shown that $V^c_{\rm vdW}/V^f_{\rm vdW} < 1$, i.e. the magnitude of $V^c_{\rm vdW}$ is usually smaller than that of $V^f_{\rm vdW}$. When the atom-to-surface distance D tends to zero the two potentials $V^c_{\rm vdW}$ and $V^f_{\rm vdW}$ tend to the same values. When D increases, the ratio $V^c_{\rm vdW}/V^f_{\rm vdW}$ lessens, that is, the relative difference between $V^c_{\rm vdW}$ and $V^f_{\rm vdW}$ increases. This makes sense since the closer the atom is to the cylindrical surface, the more the fiber *looks* like a flat wall to the atom.

In Chapter 3, when we consider the combination of a nanofiber with an optical lattice, we have a situation where the two atoms that are closest to the fiber are sitting at a distance which is half the lattice constant away from the fiber axis. Therefore the distance from the trapped atom to the fiber surface is given by $D = r - a = (\lambda/4) - 150\text{nm} = 150\text{nm}$, if we consider a lattice with a wavelength of $\lambda = 1200$ nm. We will see that the significant part of the van der Waals potential is well inside this range, i.e. in the region of $r < 100$ nm. Since it is the short range, $r - a \leq \lambda/10$, over which the effects of the van der Waals interaction are most significant, the flat surface approximation is sufficient for our simulations. The trapping potential shown in Fig. 2.11 (created by a red- and a blue-detuned field, see next section) also includes the effect of the van der Waals interaction. Atoms within the range of the van der Waals potential will be attracted to the fiber and contact with the high temperature object will lead to their loss from the system. In all of the nanofiber schemes presented in Chapters 3, 4, and 5, we will

need to consider the influence of the van der Waals potential and in each of these chapters it will be necessary to include a repulsive, blue-detuned, evanescent field for the purpose of keeping trapped atoms away from the fiber surface.

2.8 Two-Color Evanescent Field Trap

In the paper presented in Chapter 3 I will show that by combining two oppositely detuned evanescent fields with the optical lattice potential, and taking into account the van der Waals forces acting on an atom close to the surface of the fiber, it is possible to influence the geometry of the optical lattice potential locally in a highly controllable way, without disturbing the lattice globally.

In this section I will describe the trapping potential that can be formed in the evanescent field of a tapered optical fiber when an atom is in the presence of two light fields in their fundamental modes with frequencies ω_1 and ω_2, wavelengths λ_1 and λ_2 and wave numbers k_1 and k_2, respectively. This kind of trapping scheme was first discussed by Le Kien, Balykin and Hakuta in [16, 58, 59] inspired by the earlier work of Ovchinnikov [60]. We ensure that the single mode condition $V_i \equiv k_i a\sqrt{n_1(\omega_i)^2 - {n_2}^2} < V_c \cong 2.405$ is satisfied for both modes.

To avoid having to deal with dissipative processes we will assume that the atom is in the ground-state and that the light fields are far detuned from the atomic transition frequencies. The optical potential in the field of mode i is given by $U_i = -\frac{1}{4}\alpha_i|E_i|^2$, where α is the real part of the atomic polarizability, discussed in Sec. 2.1, at the optical frequency ω_i [32]. The factor of 1/4 in the optical potential U comes from the fact that 1/2 is contributed by the temporary induced dipole and the other 1/2 by time-averaging of the intensity over optical oscillations.

For the evanescent field to form a radially symmetric potential with a minimum in a ring around the fiber we require that the input fields are circularly polarized (see description in Chapter 2). The polarization of the transverse component of each propagating field rotates elliptically in time, and in cylindrical co-ordinates

$\{r, \phi, \theta\}$ the time-averaged intensity of the electric field in the mode i is given by

$$|E_i|^2 = \mathcal{E}_i{}^2 \left[{K_0}^2(q_i r) + w_i {K_1}^2(q_i r) + f_i {K_2}^2(q_i r) \right] . \tag{2.83}$$

Here $\mathcal{E}_i$ is the strength of the electric field and w_i and f_i are defined in eqs. (2.49) and (2.50).

The force of the optical potential can be attractive or repulsive depending on the sign of the detuning with respect to the atomic transition used for trapping. We choose parameters so that mode 1 is red detuned ($\Delta_1 < 0$) and mode 2 is blue-detuned ($\Delta_2 > 0$). If we assume that the timescale of atomic motion is much slower than the beating period of the two light fields (the beating period is given by the inverse of their frequency difference) then we can add the two optical potentials to find a net optical potential given by

$$\begin{aligned} U_{\text{red-blue}}(r) =& G_2[K_0^2(q_2 r) + w_2 K_1^2(q_2 r) + f_2 K_2^2(q_2 r)] \\ & - G_1[K_0^2(q_1 r) + w_1 K_1^2(q_1 r) + f_1 K_2^2(q_1 r)] . \end{aligned} \tag{2.84}$$

Here $G_1 = \alpha_1 \mathcal{E}_1^2/4 = |\alpha_1| \mathcal{E}_1^2/4$ and $G_2 = -\alpha_2 \mathcal{E}_2^2/4 = |\alpha_2| \mathcal{E}_2^2/4$ are proportional to the powers in the corresponding modes. Since the detunings are in opposite directions, α_1 will always be positive and α_2 will always be negative. We know that the sign of G_1 is directly determined by the sign of the atomic polarizability α_1, and the sign of G_2 is directly determined by the sign of α_2. This allows us to take absolute values in the expressions for G_1 and G_2 because their sign difference is accounted for in eqn.(2.84). Since the evanescent decay length $\Lambda_2 = 1/q_2$ of the blue-detuned field is shorter than the evanescent decay length $\Lambda_1 = 1/q_1$ of the red-detuned field [42] (which follows from the fact that $\omega_1 < \omega_2$) we also find $q_1 < q_2$.

By choosing parameter values for the two fields, so that the repulsive force exerted by the blue-detuned field appropriately balances the attractive force associated with the red-detuned field, it is possible to create a ring shaped trapping potential in the transverse plane. When the light is circularly polarized, U is independent of

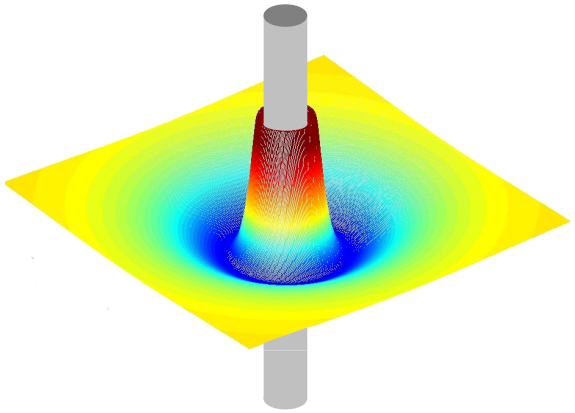


FIGURE 2.10: The two-colour evanescent field of the HE_{11} mode with circular polarization around a tapered optical fiber, including the van der Waals interaction. The axes are not shown here but the dimensions of the potential are given in Fig. 2.11. The possible trapping depths range from a few pico-Kelvin to a few micro-Kelvin. The parameters are given in the text. (This image appears in the paper included in Chapter. 3, Phys. Rev. A **85**, 053418 (2012).)

ϕ and z, and so the trapping potential is radially symmetric. Atoms close to the fiber surface, can be confined in this cylindrical shell-shaped trapping potential. Confinement in the z-direction can be achieved by counter-propagating one of the fields in the fiber which leads to a series of ring traps around the z-axis. Fig. 2.10 shows a 2D plot of the symmetric trapping ring around the fiber and a single slice of this potential is presented in Fig. 2.11.

The parameters taken here are $\lambda_1 = 980$ nm, $\lambda_2 = 640$ nm, $P_1 = 3$ mW and $P_2 = 2.5$ mW. The fiber radius chosen is $a = 150$ nm, the refractive indices are $n_2 = 1$ and n_1, the refractive index of silica, is calculated using eq. (2.91) for the relevant wavelengths (see below). In Fig. 2.11, the dashed red line indicates the fiber surface, the solid red and blue lines are the absolute values of the red and blue-detuned evanescent field contributions to the potential respectively, the dashed black line is the van der Waals interaction and the solid black line is the total potential, i.e. the sum of the red and blue-detuned evanescent field potentials and the van der Waals potential. For typical experimental parameters, the value of $q_i a$ is large and so the coefficients w_i and f_i are small (more specific typical values are given later in Sec. 2.8.1). Therefore the contributions of the terms containing w_i and f_i in eq. (2.84) are not substantial and the first term in each expression is

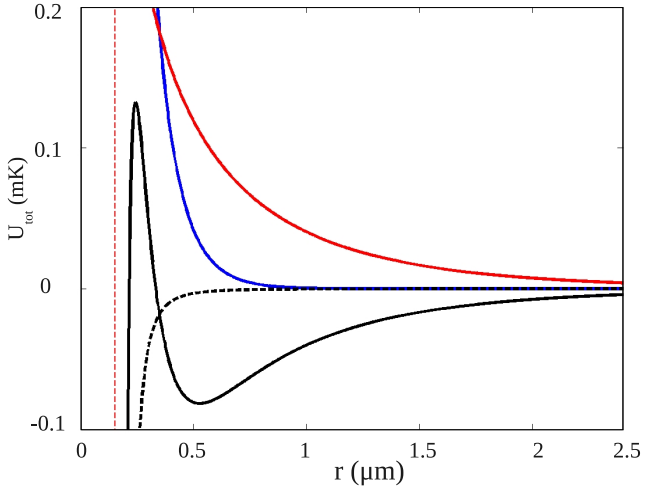


FIGURE 2.11: A slice of the radially symmetric evanescent field potential shown in Fig. 2.10 in the radial direction. The solid red line represents the absolute value of the red-detuned field. The solid blue line represents the absolute value of the blue-detuned field. The dashed black line represents the van der Waals potential and the solid black line represents the sum of the three together. The dashed red line is the fiber surface.

a good approximation to the exact potential shape [55]

$$U_{\text{red-blue}}(r) \approx G_2 K_0^2(q_2 r) - G_1 K_0^2(q_1 r) \; . \tag{2.85}$$

While this approximation is not good enough to investigate the exact dynamics of atoms in the vicinity of the fiber, it can be used to approximate such things as the distance of the minimum point from the fiber axis. Let us call the value of r at which the minimum is located R_m. We then know that $U'(R_m) = 0$, which leads to [16]

$$q_2 G_2 K_0(q_2 R_m) K_1(q_2 R_m) - q_1 G_1 K_0(q_1 R_m) K_1(q_1 R_m) = 0 \; , \tag{2.86}$$

and therefore

$$\frac{G_2}{G_1} = \frac{q_1 K_0(q_1 R_m) K_1(q_1 R_m)}{q_2 K_0(q_2 R_m) K_1(q_2 R_m)} \; . \tag{2.87}$$

When $r \neq R_m$ it is worth considering the right hand side of eq. (2.87) more closely. Since $q_1 < q_2$, it is a monotonically increasing function of r and we know that if it

has a solution $R_m > a$ with

$$\frac{G_2}{G_1} > \frac{q_1 K_0(q_1 a) K_1(q_1 a)}{q_2 K_0(q_2 a) K_1(q_2 a)}\,, \tag{2.88}$$

then a trapping minimum in the evanescent field outside the fiber exists. This can be achieved if either the power in the blue-detuned field is large enough or the power of the red-detuned field is small enough (but not zero). It is helpful to note that when the power in the blue-detuned light field increases or the power of the red-detuned field decreases, the trapping potential becomes shallower and the minimum point moves away from the fiber surface. Conversely, when the power of the blue-detuned light decreases or the power of the red-detuned light increases, the potential depth increases and the minimum is moved towards the fiber surface.

If the atom makes contact with the room-temperature fiber surface, it will be lost. To prevent this one must ensure that the potential has a non-negative value at the fiber surface, which means

$$\frac{G_2}{G_1} \geq \frac{K_0^2(q_1 a)}{K_0^2(q_2 a)}\,, \tag{2.89}$$

and the depth of the potential will take its maximum value when [16]

$$\frac{G_2}{G_1} = \frac{K_0^2(q_1 a)}{K_0^2(q_2 a)}. \tag{2.90}$$

For a more comprehensive discussion about the effects changes in the evanescent field parameters have on the shape of the potential see [16].

In recent years, further work has shown that the two-color trap can be made state insensitive by using so-called *magic wavelengths* [61, 62]. Vector light shifts due to the elliptic polarization of the nanofiber modes can be also be removed by introducing counter propagating beams [62, 63].

Lastly, fig. 2.12 shows an example of the kind of two-color evanescent field trap that can be created using a similar scheme as that described above (also described in [16]), but exploiting the asymmetry of the intensity field in the vicinity of the

fiber when the propagating light is quasi-linearly polarized, as discussed in Sec. 2.5.1.

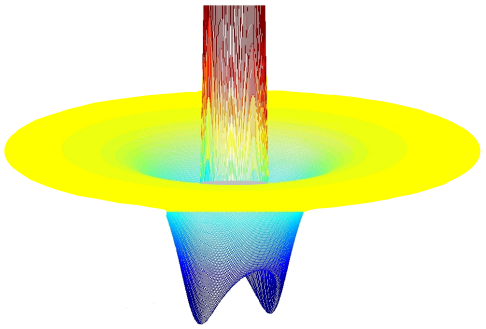


FIGURE 2.12: The two-color evanescent field of the HE_{11} mode with quasi-linear polarization around a tapered optical fiber. The axes are not labeled here, the trapping depth is on the order of a few micro-Kelvin. The minima are positioned at approximately 500 nm from the fiber axis.

2.8.1 Reasonable Experimental Values

In this thesis we consider tapered optical fibers (TOF) with radii starting at $a = 150$ nm and never exceeding $a = 500$ nm, which covers the transition from the single-mode regime to the one where four modes can propagate for the wavelengths of interest. The refractive index of the vacuum clad is $n_2 = 1$. The refractive index of fused silica (SiO_2) is a function of the traveling wavelength and can be obtained using a Sellmeier-type dispersion formula and assuming the refractive index of the vacuum to be $n_2 = 1$ [64]:

$$n_1 = 1 + \frac{0.6961663\lambda^2}{\lambda^2 - (0.0684043)^2} + \frac{0.4079426\lambda^2}{\lambda^2 - (0.1162414)^2} + \frac{0.8974794\lambda^2}{\lambda^2 - (9.896161)^2} \,. \qquad (2.91)$$

In this formula the wavelength λ is taken in units of μm. For quick calculations n_1 is often approximated as $n_1 \approxeq 1.45$.

An effort has been made to ensure that the values of the parameters chosen throughout this thesis are consistent with current experimental possibilities. The two atomic species of particular relevance to us in this thesis are the alkali atoms

Rubidium-87 (^{87}Rb) and Cesium-133 (^{133}Cs). The two dominant lines in the alkali atoms are the $D_1(^2S_{1/2} \rightarrow \ ^2P_{1/2}$ and $D_2(^2S_{1/2} \rightarrow \ ^2P_{3/2})$ transitions. When we discuss trapping of ^{87}Rb we consider that the atoms are excited at the dominant $5S-5P$ optical transition with a wavelength $\lambda = 780$ nm. The upper $5P$ level has a spontaneous decay rate at this transition of $2\gamma_0 = 2\pi \cdot 6$ MHz. At the aforementioned transition the van der Waals constant, C_3, is evaluated as $C_3 = 2\pi \cdot 3$ kHz μm^3 [65, 66]. In the publications presented in Chapters 3 and 4, we consider two light fields in the fiber, one blue-detuned and one red-detuned, with detunings chosen on the order of $\frac{\Delta}{2\pi} = 10^2$ THz. The evanescent decay lengths of the light fields extend quite far outside the fiber, particularly the red detuned field, which is significant as far as $\Lambda \approx 1.2\,\mu$m. Similarly, when discussing ^{133}Cs, we consider the dominant wavelength at $\lambda = 852$ nm.

To highlight some of the unique properties of a single mode nanofiber with linearly polarized light, as discussed in Sec. 2.5, we give a numerical example here. We choose a fiber radius $a = 150$ nm that is small compared to the optical wavelength λ =980 nm for this example. In this case the refractive index of the silica core is $n_1 \cong 1.4507$ and that of the vacuum clad is $n_2 = 1$. Solving eq. (2.37), gives us $ha \approx 1.0074$, $qa \approx 0.0819$, and $\beta a \approx 0.9652$. Using these parameters, we find $s \approx -0.9938$. Since the fiber radius a is small compared to the wavelength λ, the evanescent decay length is large compared to the fiber radius, leading to an intensity distribution where most of the power of the field is located outside the fiber. The single-mode condition is satisfied, $V = ka\sqrt{n_1^2 - n_2^2} \approx 1.0107 < 2.405$, indicating that the considered fiber is a single-mode fiber. The field intensity distribution of the evanescent field is not cylindrically symmetric and significant azimuthal variations exist. This azimuthal dependence is in the terms $wK_1^2(qr)\cos[2(\phi-\phi_0)]$ and $fK_0(qr)K_2(qr)\cos[2(\phi-\phi_0)]$ which are considerable because qa is small, so that close to the fiber surface $K_1(qr)$ and $K_2(qr)$ are dominant over $K_0(qr)$. For this example we have $K_1(qa)/K_0(qa) \cong 4.6040$ and $K_2(qa)/K_0(qa) \cong 113.43$.

When we calculate the atomic polarizability α, first described in Sec. 2.1, we consider the four dominant lines of the ^{87}Rb atom, which are (see [67]) $\lambda_{1a} = 780.027$ nm, $\lambda_{2a} = 794.760$ nm, $\lambda_{3a} = 420.180$ nm, and $\lambda_{4a} = 421.553$ nm . The

emission transition probabilities of these lines are given by $\gamma_{1a} = 3.81 \times 10^7$ s^{-1}, $\gamma_{2a} = 3.61 \times 10^7$ s^{-1}, $\gamma_{3a} = 0.18 \times 10^7$ s^{-1}, and $\gamma_{4a} = 0.15 \times 10^7$ s^{-1}, respectively.

For ^{133}Cs the numbers substituted are (again see [67]) $\lambda_{1a} = 852.11$ nm, $\lambda_{2a} = 894.35$ nm, $\lambda_{3a} = 455.53$ nm, and $\lambda_{4a} = 459.32$ nm. The emission transition probabilities of these lines are given by $\gamma_{1a} = 3.28 \times 10^7$ s^{-1}, $\gamma_{2a} = 2.86 \times 10^7$ s^{-1}, $\gamma_{3a} = 0.18 \times 10^7$ s^{-1}, and $\gamma_{4a} = 0.07 \times 10^7$ s^{-1}, respectively. For both ^{87}Rb and ^{133}Cs the four corresponding upper states have statistical weights of $g_1 = 4$, $g_2 = 2$, $g_3 = 4$ and $g_4 = 2$ and the statistical weight of the ground state is $g_a = 2$.

Chapter 3

Creating Atom-Number States Around Tapered Optical Fibers by Loading From an Optical Lattice

Note: The groundwork for this paper was done during my masters degree in 2009, while I was working on ideas for implementing quantum logic operations in optical lattices using nanofibers. The idea of preparing number states was only conceived towards the end of the MSc, and even though early results appear in my MSc thesis, the bulk of the project was carried out in 2011, when I rejoined Prof. Busch's research group as a PhD student. The paper was finally completed and accepted in early 2012. Except for the initial schematic, none of the figures in the paper appear in my MSc thesis.

3.1 Introduction

In the paper that follows, I present a scheme where a two-color evanescent field around a subwavelength diameter tapered nanofiber, (as first described by Le Kien

et al. [16]), can be inserted at an appropriate point in a optical lattice in order to allow local manipulations of the optical potential geometry. I show that when the fiber is aligned perpendicularly to the transverse plane of a two-dimensional optical lattice the evanescent field around the fiber can be used to create a time-dependent potential which locally *melts* the lattice potential. Since we have control over the evanescent field parameters, we have some control over the number of lattice sites that become affected by the potential, and thereby, in the Mott limit, over the number of atoms.

The introduction of a tapered fiber into a lattice will cause modification of the lattice structure due to scattering at the fiber surface and I first show that this modification is weak enough to not destroy the periodic arrangement of the trapping sites. However, the attractive van der Waals interaction is large enough to have a significant influence on the atoms in the trapping sites closest to the fiber surface and to prevent losses due to this, I investigate the use of a repulsive (blue-detuned) evanescent field to enhance the barrier close to the fiber. Lastly I characterize the resulting atomic samples in the melted part of the lattice.

This scheme allows access to a regime in which a small number of particles can be addressed locally without disturbing the rest of the lattice. Furthermore, when the environment around the fiber is given by a well ordered Mott-Insulator state, melting the lattice transfers a controllable and well-defined number of atoms from the individual lattice sites around the fiber into the fiber potential. Once this has happened, the optical lattice can be switched off to prevent other atoms from entering the fiber potential by tunneling. The atom number is therefore fixed by the initial choice of evanescent field parameters and does not change. Such states are also of interest in quantum information as they carry large quantities of entanglement [68].

3.2 Paper

Manuscript Information

Manuscript Title: Creating atom-number states around tapered optical fibers by loading from an optical lattice.

Journal Information: Phys. Rev. A **85**, 053418 (2012).

Authors: Tara Hennessy and Thomas Busch

DOI: 10.1103/PhysRevA.85.053418

The project was suggested by Thomas Busch developed equally between him and myself. All calculations were carried out by me.

Creating atom-number states around tapered optical fibers by loading from an optical lattice

T. Hennessy* and Th. Busch
Department of Physics, University College Cork, Cork, Republic of Ireland
(Received 6 December 2011; published 22 May 2012)

We describe theoretically a setup in which a tapered optical nanofiber is introduced into an optical lattice potential for cold atoms. First, we consider the disturbance to the geometry of the lattice potential due to scattering of the lattice lasers from the dielectric fiber surface and show that the resulting distortion to the lattice can be minimized by placing the fiber at an appropriate position in the lattice. We then calculate the modifications of the local potentials that are achievable by transmitting off-resonant light through the fiber. The availability of such a technique holds the potential to deterministically create and address small well-defined samples of atoms in the evanescent field of the tapered nanofiber.

DOI: 10.1103/PhysRevA.85.053418 PACS number(s): 37.10.Jk, 37.10.Vz, 42.81.Wg

I. INTRODUCTION

During the last two decades, advances in the cooling and trapping of atoms and ions have assisted in the creation of clean and highly controllable systems, in which fundamental quantum-mechanical experiments can be carried out with very low levels of noise. This has led to several breakthrough successes in the quest for implementing ideas of quantum information processing (QIP) [1], high-precision atomic clocks [2], and quantum metrology [3].

For neutral atoms optical lattices have been important and hold a great deal of promise in this area. The high degree of control one has over the laser parameters has allowed for the execution of many seminal experiments in these periodic systems. In particular, by controlling the amplitude of the lasers one can adjust the trapping depth, which can act as a switch between regimes in which the dynamics are controlled either by tunneling between different lattice sites or by interactions between the atoms. This has led to the celebrated observation of the superfluid–Mott insulator transition, in which a state with one atom per lattice site can be created [4,5].

States which have a well-defined number of particles, so-called atomic Fock states, are currently of large interest in physics. Their sub-Poissonian number statistics is valuable for applications in atom metrology and quantum information processing and has merit for investigating the foundations of quantum mechanics as well. Several ground-breaking experiments have recently reported the creation of such states [6–8], and a significant amount of theoretical work has been devoted to their characterization [9,10]. Knowing the exact number of atoms *a priori* in each run of the experiment is still a difficult task, and techniques which can deterministically create a desired atom number are under vigorous development.

Here we present a near-field optics approach to creating such definite atom-number states and propose the use of the evanescent field of an optical fiber as a tool for manipulating the optical lattice potential locally (see Fig. 1). While standard optical fibers have a diameter of several hundred micrometers, recent progress in tapering techniques allows for the creation of fibers of subwavelength diameter [11] and even down to 50 nm [12]. A significant amount of the intensity in these fibers is carried in their evanescent field and can therefore be used to create an optical potential for ultracold atoms. In this work we will examine the effects of introducing a submicrometer fiber into an optical lattice and demonstrate the possibility of deterministically creating states of fixed particle number using appropriately chosen fields inside the fiber.

This paper is organized as follows: in Sec. II we will present a short review of the potential forces relating to optical lattices and submicrometer-diameter, single-mode silica fibers. We then discuss the modifications of an optical lattice potential due to effects from light scattering on a fiber in Sec. III and examine several achievable potential geometries resulting from the combination of the lattice potential and the evanescent field potentials in Sec. IV. The resulting atomic state is discussed in Sec. V, and we finally conclude in Sec. VI.

II. POTENTIAL FORCES

A. Optical lattices

To understand the influence the introduction of the fiber into an optical lattice has, let us first briefly review the optical potentials associated with optical lattices and nanofibers. Optical lattices exist today in many laboratories and represent periodic arrays of microtraps generated by the dipole force of a standing-wave laser light field [4,5,13]. A variety of trapping geometries are achievable, with the most common being rectangular [5] or triangular [14].

The simplest case of an optical lattice trapping potential is given by a one-dimensional model, in which two counterpropagating laser beams interfere. This results in a standing wave for the optical intensity given by

$$I(z) = I_0 \sin^2(kz), \tag{1}$$

where $k = 2\pi/\lambda$ is the free-space wave number of the laser light, I_0 is the maximum intensity of the laser beam, and the periodicity is given by $\lambda/2$. The spatially varying ac Stark shift then forms a potential for the induced dipole moment $\mathbf{p}$ of the atom given by

$$U_{\mathrm{dip}} = -\frac{1}{2}\langle \mathbf{p}\cdot\mathbf{E}\rangle = -\frac{1}{2\epsilon_0 c}\mathrm{Re}(\alpha)I, \tag{2}$$

where ϵ_0 is the vacuum permittivity, c is the speed of light, and $\alpha(\omega_L)$ is the optical polarizability, which depends on the

*thennessy@phys.ucc.ie

 ©2012 American Physical Society

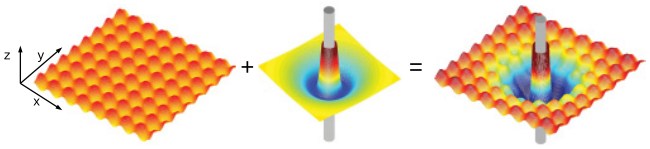


FIG. 1. (Color online) Schematic showing a typical optical potential geometry resulting from the combination of an optical lattice potential and a trapping potential around an optical nanofiber.

frequency of the laser field **E**. Its real part is given by Ref. [15]

$$\alpha(\omega) = 2\pi\epsilon_0 c^3 \sum_j \frac{g_j}{g_a} \frac{\gamma_{ja}\left(1-\frac{\omega^2}{\omega_{ja}^2}\right)}{\left(\omega_{ja}^2-\omega^2\right)^2+\gamma_{ja}^2\omega^2}, \tag{3}$$

where g_j and g_a are the statistical weights of the excited and ground states, respectively, ω_{ja} are the transition frequencies, and γ_{ja} are the emission transition probabilities [16]. Depending on the detuning of the laser beam, the atoms can be forced to gather at the nodes or antinodes of the laser intensity pattern by using light blue-detuned ($\omega_L > \omega_0$) or red-detuned ($\omega_L < \omega_0$) with respect to the chosen transition ω, respectively.

By introducing pairs of counterpropagating lasers in the remaining directions of space, higher-dimensional lattices can be created. The interference terms between the laser fields in the different directions can be eliminated by choosing perpendicular polarization vectors of the two laser fields, which for a two-dimensional setup results in an intensity pattern represented by the sums of purely sinusoidal orthogonal fields (see Fig. 1):

$$I(x,y) = I_0[\sin^2(kx) + \sin^2(ky)]. \tag{4}$$

Throughout this paper we will consider this type of two-dimensional optical lattice; however, a generalization to three-dimensional, layered lattices is straightforward. We will also assume that every beam is independent and not created through retroreflection.

Optical lattices typically have lattice constants in the range of 400–650 nm, and we will consider a lattice with a trapping wavelength $\lambda/2 = 527$ nm. We choose the lattice to be loaded with ^{133}Cs atoms, which localize in the high-field regions.

B. Subwavelength diameter optical fibers

Recent developments in tapered, dielectric fiber technology have made it possible to produce fibers with radii a as low as a few hundred nanometers [12]. In such fibers the core has vanished, and the fibers can be described by one large refractive index step between the remaining cladding, $n_1(\omega)$, and the outside vacuum, n_2. An interesting consequence of the subwavelength nature of the diameter is that the majority of the field will be guided in the evanescent field on the fiber's surface. It therefore becomes accessible to atoms in the fiber's vicinity, and light blue-detuned with respect to the atoms transition frequency will create a repulsive force, preventing the atoms from coming too close to the fiber, which is at room temperature. At the same time red-detuned light will result in an attractive force, and a combination of both fields was suggested by Le Kien *et al.* [17] as a way of creating a trapping potential around the fiber. This was experimentally observed in Ref. [18].

Let us briefly review the description of such a potential, following closely [17]. We consider two frequencies, ω_r and ω_b, where the indices correspond to the red- and blue-detuned fields, respectively. They are chosen such that the single-mode condition

$$V_i \equiv k_i a\sqrt{n_1^2(\omega) - n_2^2} < 2.405 \tag{5}$$

is fulfilled [19] and both light fields are in the fundamental mode HE_{11}. The intensity distribution of the evanescent fields depends on the polarization of the input fields, and here we choose circular polarization for both beams to achieve angular symmetry [20,21]. In cylindrical coordinates $\{r,\phi,\theta\}$, the time-averaged intensity outside the fiber is then given by

$$|E_i|^2 = \epsilon_i^2\left[K_0^2(q_i r) + w_i K_1^2(q_i r) + f_i K_2^2(q_i r)\right]. \tag{6}$$

Here K_n are the modified Bessel functions of the second kind and ϵ_i is the strength of the electric field. The decay of the fields from the surface of the fiber is characterized by q_i, which is the reciprocal of the decay length Λ_i and is given by

$$q_i = \sqrt{\beta_i^2 - {n_2}^2{k_i}^2}, \tag{7}$$

where β is the longitudinal propagation constant of the mode [20]. Finally, the prefactors are given by Ref. [21]

$$w_i = \frac{2{q_i}^2}{\beta_i^2(1-s_i)^2}, \tag{8}$$

$$f_i = \frac{(1+s_i)^2}{(1-s_i)^2}, \tag{9}$$

with s defined as

$$s_i = \frac{\left(\frac{1}{q_i^2a^2}+\frac{1}{h_i^2a^2}\right)}{\left[\frac{J_1'(h_ia)}{h_iaJ_1(h_ia)}+\frac{K_1'(q_ia)}{q_iaK_1(q_ia)}\right]} \tag{10}$$

and $h_i = (n_1^2k_i^2 - \beta_i^2)^{\frac{1}{2}}$. The combined optical potential around the fiber for a blue-detuned field and a red-detuned field is therefore given by (see Fig. 1)

$$U(r) = \frac{|\alpha_b|\varepsilon_b^2}{4}\left|\left[K_0^2(q_br) + w_bK_1^2(q_br) + f_bK_2^2(q_br)\right]\right. - \frac{|\alpha_r|\varepsilon_r^2}{4}\left|\left[K_0^2(q_rr) + w_rK_1^2(q_rr) + f_rK_2^2(q_rr)\right]\right., \tag{11}$$

where the factors in front of the mode-structure terms are directly proportional to the powers of the individual light fields, P_r and P_b.

C. Van der Waals interaction

Finally, we need to take into account the van der Waals attraction between the atoms and the fiber. The classical van der Waals potential felt by an atom near the surface of a dielectric fiber of infinite length is given by Ref. [22]

$$V(r) = \frac{\hbar}{4\pi^3\epsilon_0}\sum_{n=-\infty}^{\infty}\int_0^\infty dk\left[k^2K_n'(kr) + \left(k^2+\frac{n^2}{r^2}\right)K_n^2(kr)\right] \times \int_0^\infty d\xi\ \alpha(i\xi)G_n(i\xi), \tag{12}$$

where

$$G_n(\omega) = \frac{[\epsilon(\omega) - \epsilon_0] I_n(ka) I_n'(ka)}{\epsilon_0 I_n(ka) K_n'(ka) - \epsilon(\omega) I_n'(ka) K_n(ka)}. \quad (13)$$

Here $I_n(x)$ and $K_n(x)$ are the modified Bessel functions of the first and second kinds, respectively. It should be noted that this approximation neglects the resonant frequencies of silica. However, as these are substantially different and weaker than those of Cs atoms, this is justified [17].

A detailed analysis of expression (12) was carried out by Le Kien *et al.* [17], who found that for atoms close to the surface the van der Waals potential tends to the same values as that for a flat surface. The latter has the simple and well-known form

$$V_{\text{flat}} = -\frac{C_3}{(r-a)^3}, \quad (14)$$

$$C_3 = \frac{\hbar}{16\pi^2\epsilon_0} \int_0^\infty d\xi \; \alpha(i\xi) \left[\frac{\epsilon(i\xi) - \epsilon_0}{\epsilon(i\xi) + \epsilon_0}\right]. \quad (15)$$

The ground-state cesium atom has its dominant (D_2) line at 852 nm, which gives a van der Waals constant of $C_3 = 2\pi \times 1.56$ kHz μm^3 [23], and this value will be used throughout this paper. In the following we will also use the simplified expression (14) whenever justified while making sure the full expression gives identical results.

III. SCATTERING AT THE FIBER

When a fiber is introduced in a position perpendicular to the transverse plane of a two-dimensional optical lattice, the four incident beams will be scattered from the cylindrical surface and distort the regularity of the lattice. To describe this we approximate the fiber by an infinite cylinder of radius $a = 150$ nm oriented orthogonally to the lattice vectors and assume that the waves undergo a linear scattering process [24]. In cylindrical coordinates the four incident waves of the conventional lattice have the form of plane waves,

$$\mathbf{E}_I(\theta_j) = \mathbf{E}_0 \exp\left[ikr\cos(\theta - \theta_j)\right], \quad (16)$$

coming from the angles $\theta_j = 0, \pi/2, \pi, 3\pi/2$, and the total lattice field is that given by

$$E_I = \sqrt{[\mathbf{E}_I(0) + \mathbf{E}_I(\pi)]^2 + \left[\mathbf{E}_I\left(\frac{\pi}{2}\right) + \mathbf{E}_I\left(\frac{3\pi}{2}\right)\right]^2}. \quad (17)$$

Assuming that the beams along the $\pi/2$ direction are polarized parallel to the cylinder axis and the ones along the π direction are orthogonal, the scattered field can be written as in Ref. [25], where the respective polarizations are contained in E_0.

$$E_S^{\parallel} = E_0 \sum_{n=0}^{\infty} \left\{ i^n a_n H_n^{(1)}(kr) \cos\left[n\left(\theta + \frac{\pi}{2}\right)\right] + i^n a_n H_n^{(1)}(kr) \cos\left[n\left(\theta + \frac{3\pi}{2}\right)\right]\right\}, \quad (18)$$

$$E_S^{\perp} = \frac{E_0}{kr} \sum_{n=0}^{\infty} \left\{ i^n b_n H_n^{(1)}(kr) \cos(n\theta) + i^n b_n H_n^{(1)}(kr) \cos[n(\theta + \pi)]\right\}, \quad (19)$$

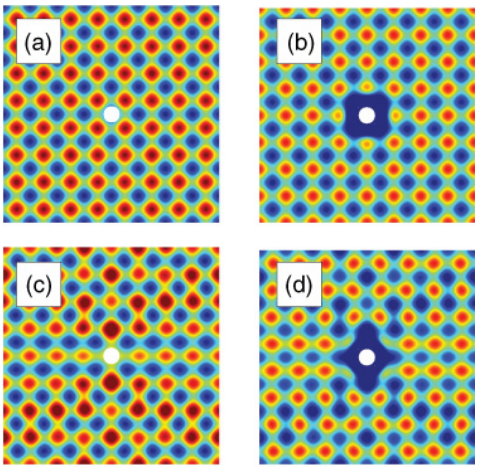


FIG. 2. (Color online) (a) Lattice intensity including the scattering of the light on the fiber when the fiber is placed at an intensity minimum of the lattice. (b) van der Waals potential and optical lattice potential which includes the scattered lattice field. (c) and (d) show the same for a fiber placed at a lattice intensity maximum. Each plot spans an area of 4.2 μm $\times$ 4.2 μm, and the lattice depth is $60E_R$. A color scale has been used which varies from blue to red, where the blue (dark gray) areas correspond to minima and red (medium gray) areas correspond to maxima.

where $H_n^{(1)}$ are Hankel functions of the first kind and the scattering coefficients are given by

$$a_n = \frac{J_n(\alpha) J_n'(m\alpha) - m J_n(m\alpha) J_n'(\alpha)}{H_n^{(2)}(\alpha) J_n'(m\alpha) - m J_n(m\alpha) H_n^{(2)'}(\alpha)}, \quad (20)$$

$$b_n = \frac{m J_n(\alpha) J_n'(m\alpha) - J_n(m\alpha) J_n'(\alpha)}{m H_n^{(2)}(\alpha) J_n'(m\alpha) - J_n(m\alpha) H_n^{(2)'}(\alpha)}. \quad (21)$$

From this the complete field follows as

$$E_{\text{tot}} = \sqrt{(E_I^{\parallel} + E_S^{\parallel})^2 + (E_I^{\perp} + E_S^{\perp})^2}. \quad (22)$$

Here we note that all of the square plots in this paper span an area of 4.2 μm $\times$ 4.2 μm. This 4.2 μm corresponds to approximately four optical lattice wavelengths and thus an eight by eight grid of traps. The optical intensity in the vicinity of a fiber of radius $a = 150$ nm for a lattice constant of $\lambda/2 = 527$ nm is shown in Figs. 2(a) and 2(c). One can see that if the fiber is located at a minimum of the optical intensity [Fig. 2(a)], the lattice structure is almost unaffected. Positioning the fiber at an optical intensity maximum [Fig. 2(c)], on the other hand, leads to noticeable disturbances, which, nevertheless, leave the basic lattice structure intact. Clearly, larger fibers will lead to more scattering; however, the numbers chosen here are well in reach of experimental possibilities.

In general the scattered radiation propagates as a cylindrical wave, and its intensity falls off as the inverse power of the radial distance. Since the energy flow is only in the planes of constant z, the scattered radiation corresponding to a particular incident ray will be observed only in that plane which contains the incident ray, and no scattering into other layers of a three-dimensional lattice occurs.

The overall potential seen by the atoms must include the van der Waals potential, and Figs. 2(b) and 2(d) show that the

lattice sites most affected by the scattering are also strongly affected by the van der Waals potential. (Note that the Cs atoms we are considering here are high-field seekers.) It is clear that in a shallower lattice the effect of the van der Waals attraction will be more severe on a larger range, and we will show in the next section that the introduction of a repulsive blue field can be a useful tool for counteracting this effect.

IV. ADDING FIBER POTENTIALS

A. Compensating the van der Waals potential

In order to minimize the disturbance of the lattice due to the van der Waals potential, we will study the possibility of compensating the attractive potential with a repulsive one from a blue-detuned optical field. The joint potential is simply given by adding the blue part of Eq. (11) to the van der Waals expression of Eq. (14):

$$U_c(r) = \frac{|\alpha_b|\varepsilon_b^2}{4}\left[K_0^2(q_b r) + w_b K_1^2(q_b r) + f_b K_2^2(q_b r)\right] - \frac{C_3}{(r-a)^3}. \quad (23)$$

Since the modified Bessel functions have an exponentially decaying form, it is not possible to perfectly compensate the van der Waals potential at all distances from the fiber. However, the discrepancy is weaker at larger distances, which allows the reduction of the radius in which the attractive potential is significant. In Figs. 3 and 4 we show the potential for the two different positions of the fiber for different intensities of the blue beam. One can clearly see that in both cases it is possible to achieve a situation in which almost all lattice sites close to the fiber are still intact (middle panel). This is important for the construction of a well-defined Mott insulator state around the fiber, which is a prerequisite to loading the fiber potential with a well-defined particle number. While the exact number of restored lattice sites also depends on the lattice depth, the graphs show typical achievable experimental values. For very small distances from the fiber surface, the attractive van der Waals potential will always be stronger than the compensating optical field, and tunneling will become an important loss factor at longer times.

Let us also remark that with such a localized potential it is possible to remove atoms from specific lattice sites by using the fiber as a dark absorber [11]. Used in conjunction with existing ideas involving optical conveyor belts [26], this simple setup could be an effective method of removing entire rows or patterns of atoms.

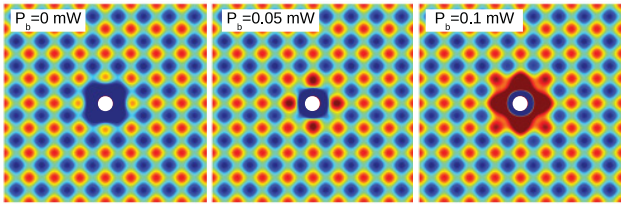


FIG. 3. (Color online) Combined potentials (van der Waals, blue-detuned evanescent field, and optical lattice) for a fiber placed at a minimum of the lattice intensity. The wavelength of the evanescent field is $\lambda_b = 700$ nm, and its power is increased through $P_b = 0$, 0.05, and 0.10 mW from left to right. The lattice depth is chosen to be $60E_R$.

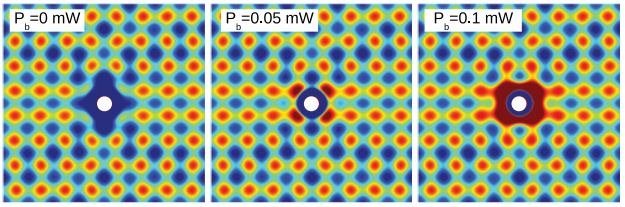


FIG. 4. (Color online) Same as Fig. 3, with the fiber placed at a maximum of intensity of the lattice. Each plot spans an area of 4.2 μm $\times$ 4.2 μm.

B. Loading the fiber potential

In the following we will consider the situation where an attractive, red-detuned field is added to the fiber as well. This will allow for the creation of a circular potential minimum around the fiber, deep enough to trap ultracold atoms. Recent experiments have demonstrated this by stochastically trapping atoms from a surrounding thermal or condensed cloud [18]. Since in our situation the environment around the fiber is given by the well-ordered optical lattice, a controlled melting of the lattice by the evanescent field will transfer a controllable number of atoms from the individual lattice sites into the fiber potential. The resulting state is therefore highly number squeezed and can be used in applications in quantum information or metrology [7,27].

We study this process by assuming a realistic experimental situation of a Mott insulator made from Cs atoms with a resonant transition at $\lambda_0 = 852$ nm [28]. For the two light fields in the fiber we consider a blue-detuned field at a wavelength of $\lambda_b = 700$ nm and the red-detuned field at $\lambda_r = 980$ nm. The detunings of the fiber fields from the dominant line of the atom are then given by $\frac{\Delta_b}{2\pi} = -46$ THz and $\frac{\Delta_r}{2\pi} = 76$ THz, and with a fiber radius of 150 nm, the evanescent decay lengths corresponding to the blue and red fields are $\Lambda_b = 0.36$ μm and $\Lambda_r = 1.83\mu$m. The two-dimensional optical lattice we consider has a depth $60E_R$.

Two typical examples of resulting trapping geometries, when all potentials are taken into account, are shown in Figs. 5 and 6 for a fiber located at an intensity minimum. Since we assume the fiber to be initially dark, the lattice sites which are visible closest to the fiber in Figs. 5(c) and 6(c) are actually empty because they are within the radius of the surface van der Waals potential. For all other sites in the vicinity of the fiber one can clearly see that the addition of the red and blue fields allows for the lowering of the on-site energies. Therefore, as the asymptotic potential of the evanescent field goes to zero and since there is no local maximum in the fiber potential, a sudden switch-off of the optical lattice will leave all atoms with center-of-mass energies <0 trapped in the fiber potential alone. In the example shown in Fig. 5, where $P_b = 0.12$ mW and $P_r = 0.036$ mW, one finds that this condition is fulfilled for eight lattice sites. Increasing the evanescent fields to $P_b = 0.17$ mW and $P_r = 0.082$ mW (see Fig. 6) the radius of the evanescent field increases, and careful examination shows that 20 sites are reached. Note that, due to

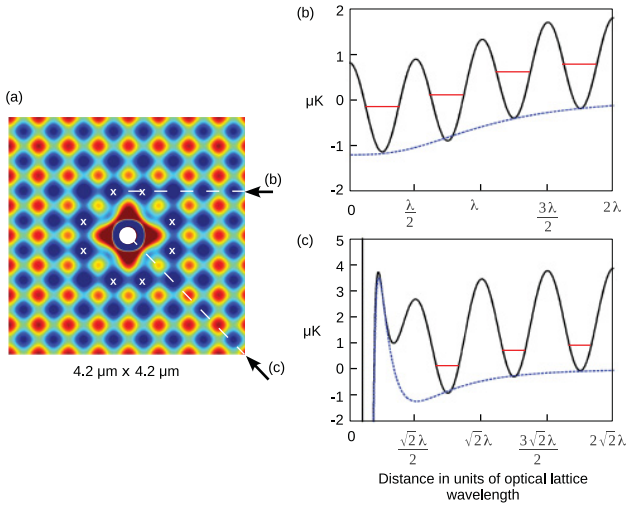


FIG. 5. (Color online) (a) The red- and blue- detuned beams in the fiber are switched on for $P_b = 0.12$ mW and $P_r = 0.036$ mW. The lattice sites for which the energy is lowered such that the residing atoms will be trapped in the fiber potential after the optical lattice is switched off are marked with a cross. (b) and (c) cut through the potential at the lines indicated in (a). The black solid line represents a slice of the two-dimensional potential geometry. The relevant on-site energies are indicated as well, and the dotted blue line indicates the potential after the optical lattice is switched off. The fact that the fiber potential does not always meet exactly the zero points of the overall potential before switch-off is due to phase shifting of the optical lattice after scattering on the fiber.

the rectangular geometry of the considered lattice, only certain atom numbers can be achieved, and realistic parameters limit this technique to samples of only a few tens of atoms. If the switch-off process of the optical lattice is done on a time scale shorter than the typical atom tunneling time in an optical lattice (which is of the order of several milliseconds [5]), no other atoms will be able to join the well-defined sample.

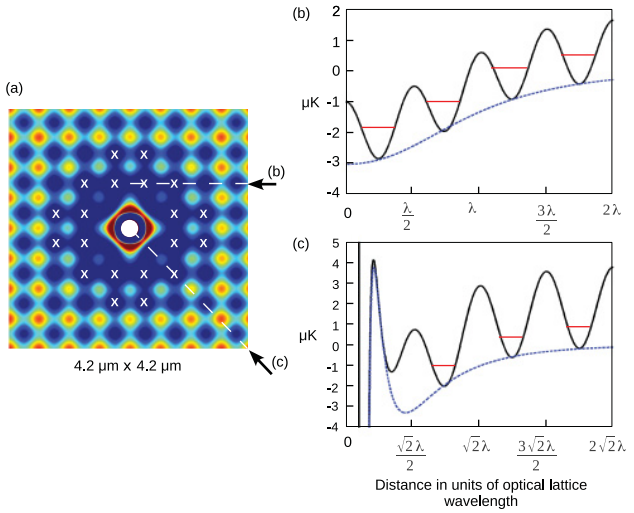


FIG. 6. (Color online) Same as Fig. 5, but for higher powers of the evanescent fields, $P_b = 0.17$ mW and $P_r = 0.082$ mW. A larger number of atoms will be trapped after the optical lattice is switched off.

The state created in this sudden-switch-off procedure is a highly excited, out-of-equilibrium state in the final potential, and subsequent cooling is necessary to prevent further atom loss due to scattering and thermalization. While a detailed calculation of these effects goes beyond the scope of this work, loss through rethermalization can be minimized by applying a Feshbach resonance while carrying out this process and subsequently adiabatically lowering the fiber potential while switching the interaction back on [29].

It is also worth pointing out that in both examples above the presence of the repulsive blue field ensures the existence of a repulsive wall between the fiber and the atoms, thereby preventing direct atom loss through the room-temperature object. However, the power in the blue-detuned field does not correspond to the same field strength that optimally cancels the effects of the van der Waals potential, as discussed in the previous section. It is rather necessary to overcompensate the van der Waals potential and recreate the trapping minimum using the red-detuned field. In the next section we will discuss the nature of the atomic state created in the fiber potential.

V. ATOMIC STATE

Let us finally briefly characterize the atomic many-body state that can be created by the procedure above and focus in particular on the nature of the correlations in the sample. For this we first consider the effective dimensionality of the ground state of the potential around the fiber after the optical lattice is switched off. Since the size of the radial ground state of the potential will be much smaller than the curved, azimuthal one, we can assume an approximate separation of the wave function in the two directions. This allows us to describe the spectrum in the azimuthal direction by a free-space periodic potential with the well-known spectrum $E_n^a = (n^2\hbar^2\pi^2)/(2mL^2)$, where $L = 2\pi r_m$ is the circumference of the potential at the position of its radial minimum r_m. Since no analytical expression for the position of this minimum is known, we find it numerically and estimate the energy difference between the ground and the first excited states in the azimuthal direction to be of the order of $\Delta E_{10}^a = E_1^a - E_0^a \sim 10^{-33}$ J for both situations shown in Fig. 5

To find the spectrum in the radial direction, we numerically diagonalize the radial part of the potential for a wide range of parameters and find typical values for the separation of the ground and first excited states to be of the order of $\Delta E_{10}^r \sim 10^{-30}$ J. This significant difference in the stiffness of the spectra in the two different directions (the z direction can be adjusted separately to be stiff) translates into an approximate one-dimensional situation with an aspect ratio of $\sim 10^3$.

Having established the effective dimensionality of the potential, the many-body state of a one-dimensional Bose gas can now be characterized using the Lieb-Liniger parameter $\gamma = mg_{1D}/\hbar^2 n_{1D}$ [30]. Here g_{1D} is the one-dimensional coupling constant given by $g_{1D} = \frac{4\hbar^2 a_{3D}}{ma_\perp}(a_\perp - Ca_{3D})^{-1}$, with $C \approx 1.4603$, and n_{1D} is the linear density of the atoms [31]. For values of $\gamma \gg 1$ the atomic many-body state would be in the strongly correlated Tonks-Girardeau regime, whereas for $\gamma < 1$ the gas can be treated as weakly correlated. For both

cases shown in Fig. 5 the radial ground-state size is of the order of $a_\perp \sim 0.2\ \mu$m (we assume the same is achieved in the z direction), and the position of the radial minimum is at $r_m \sim 6.6\ \mu$m. This leads to values of $\gamma = 0.560$ for the 8-atom case and $\gamma = 0.346$ for the 20-atom case, putting both states firmly in the weakly correlated regime.

VI. CONCLUSION

In this work we have suggested that the combination of optical lattices and tapered optical nanofibers can be used to create small atomic samples which allow control over the final atom number. While introducing the fiber into the optical lattice inevitably leads to a disturbance of the lattice in the vicinity of the fiber due to scattering of the lattice beams, we have shown that this can be minimized and, due to the small fiber diameter, usually leaves the overall lattice structure intact. The attractive van der Waals potential close to the surface of the fiber can be compensated by using a blue-detuned evanescent field around the fiber, which allows a reduction of the range of the fiber's influence to the size of a single lattice site for typical experimental parameters. Adding a second, red-detuned light field to the fiber then allows local melting of the optical lattice and can be used to create a small sample with a well-defined atom number. Finally, we have shown that these samples are in the superfluid regime and therefore are good candidates for investigating the physics of persistent currents or, using more varied optical potentials around the fiber, the physics of superfluid superconducting quantum interference devices.

ACKNOWLEDGMENTS

This project was supported by Science Foundation Ireland under Projects No. 05/IN/I852 and No. 10/IN.1/I2979. We would like to thank Síle Nic Chormaic, Laura Russell, Mary Frawley, David Rea, and Vladimir Minogin for valuable discussions.

[1] J. Stolze and D. Suter, *Quantum Computing: A Short Course from Theory to Experiment* (Wiley VCH, Weinheim, Germany, 2008).
[2] G. Wilpers, T. Binnewies, C. Degenhardt, U. Sterr, J. Helmcke, and F. Riehle, Phys. Rev. Lett. **89**, 230801 (2002).
[3] J. Ye, H. J. Kimble, and H. Katori, Science **320**, 1734 (2008).
[4] D. Jaksch, C. Bruder, J. I. Cirac, C. W. Gardiner, and P. Zoller, Phys. Rev. Lett. **81**, 3108 (1998).
[5] M. Greiner, O. Mandel, T. Esslinger, T. W. Hänsch, and I. Bloch, Nature (London) **415**, 39 (2002).
[6] C.-S. Chuu, F. Schreck, T. P. Meyrath, J. L. Hanssen, G. N. Price, and M. G. Raizen, Phys. Rev. Lett. **95**, 260403 (2005).
[7] J. Esteve, C. Gross, A. Weller, S. Giovanazzi, and M. K. Oberthaler, Nature (London) **455**, 1216 (2008).
[8] A. Itah, H. Veksler, O. Lahav, A. Blumkin, C. Moreno, C. Gordon, and J. Steinhauer, Phys. Rev. Lett. **104**, 113001 (2010).
[9] D. Sokolovski, M. Pons, A. del Campo, and J. G. Muga, Phys. Rev. A **83**, 013402 (2011).
[10] M. Pons, D. Sokolovski, and A. del Campo, Phys. Rev. A **85**, 022107 (2012).
[11] M. J. Morrissey, K. Deasy, Y. Wu, S. Chakrabarti, and S. Nic Chormaic, Rev. Sci. Instrum. **80**, 053102 (2009).
[12] L. Tong, R. R. Gattass, J. B. Ashcom, S. He, J. Lou, M. Shen, I. Maxwell, and E. Mazur, Nature (London) **426**, 816 (2003).
[13] I. Bloch, J. Dalibard, and W. Zwerger, Rev. Mod. Phys. **80**, 885 (2008).
[14] C. Becker, P. Soltan-Panahi, J. Kronjäger, S. Dörscher, K. Bongs, and K. Sengstock, New J. Phys. **12**, 065025 (2010).
[15] See, for example, J. D. Jackson, *Classical Electrodynamics*, 3rd ed. (Wiley, New York, 1998).
[16] J. E. Sansonetti, W. C. Martin, and S. L. Young (2005), Handbook of Basic Atomic Spectroscopic Data (version 1.1.2), National Institute of Standards and Technology [http://physics.nist.gov/Handbook].
[17] F. Le Kien, V. I. Balykin, and K. Hakuta, Phys. Rev. A **70**, 063403 (2004).
[18] E. Vetsch, D. Reitz, G. Sagué, R. Schmidt, S. T. Dawkins, and A. Rauschenbeutel, Phys. Rev. Lett. **104**, 203603 (2010).
[19] The refractive index n_1 of fused silica (SiO_2) can be calculated using a Sellmeier-type dispersion formula [17], taking the refractive index of the vacuum $n_2 = 1$, $n_1 - 1 = \frac{0.696166\lambda^2}{\lambda^2-(0.068404)^2} + \frac{0.407942\lambda^2}{\lambda^2-(0.116241)^2} + \frac{0.897479\lambda^2}{\lambda^2-(9.896161)^2}$, where λ is in units of micrometers.
[20] A. Yariv, *Optical Electronics* (CBS College, New York, 1985).
[21] F. LeKien, J. Q. Liang, K. Hakuta, and V. I. Balykin, Opt. Commun. **242**, 445 (2004).
[22] M. Boustimi, J. Baudon, P. Candori, and J. Robert, Phys. Rev. B **65**, 155402 (2002).
[23] L. Russell, D. A. Gleeson, V. G. Minogin, and S. Nic Chormaic, J. Phys. B **42**, 185006 (2009).
[24] M. Kerker, *The Scattering of Light, and Other Electromagnetic Radiation* (Academic, New York, 1969).
[25] A. R. Jones, J. Phys. D **6**, 417 (1973).
[26] D. Schrader, S. Kuhr, W. Alt, M. Müller, V. Gomer, and D. Meschede, Appl. Phys. B **73**, 819 (2001).
[27] M. Pons, D. Sokolovski, and A. del Campo, New J. Phys. **12**, 065025 (2010).
[28] C.-L. Hung, X. Zhang, N. Gemelke, and C. Chin, Phys. Rev. Lett. **104**, 160403 (2010).
[29] W. Alt, D. Schrader, S. Kuhr, M. Muller, V. Gomer, and D. Meschede, Phys. Rev. A **67**, 033403 (2003).
[30] E. Lieb and W. Liniger, Phys. Rev. **130**, 1605 (1963); E. Lieb, *ibid*. **130**, 1616 (1963).
[31] M. Olshanii, Phys. Rev. Lett. **81**, 938 (1998).

3.2.1 Scattering of the Lattice at the Fiber Surface: Additional Comments

The panels on the left hand side of Fig. 2 in the paper included on the previous pages (Sec. 3.2) show the lattice intensity pattern, including scattering at the fiber, when a fiber of radius $a = 150$ nm is placed at an intensity minimum in the lattice (in panel (a)) and when the fiber is placed at an intensity maximum (in panel (c)). In Figs 3.1 and 3.2 further examples of the lattice intensity pattern are included for additional values of the fiber radius a. In Fig. 3.1 the fiber sits at a lattice intensity minimum and in Fig. 3.2 the fiber sits at an intensity maximum.

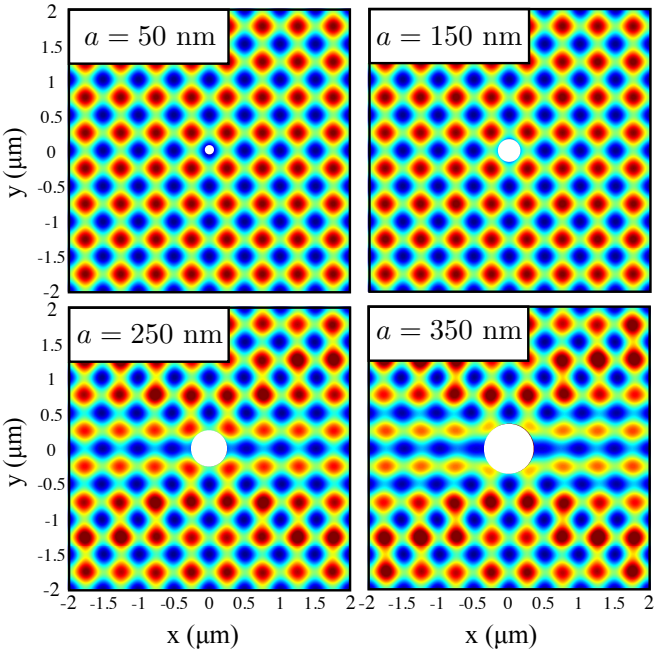


FIGURE 3.1: Lattice intensity pattern for increasing values of fiber radius when the fiber sits at a minimum of the lattice intensity. The fiber radius increases from $a = 50$ nm where no disturbance to the lattice is evident in panel (a), to $a = 350$ nm where the disturbance to the lattice is very significant in panel (d).

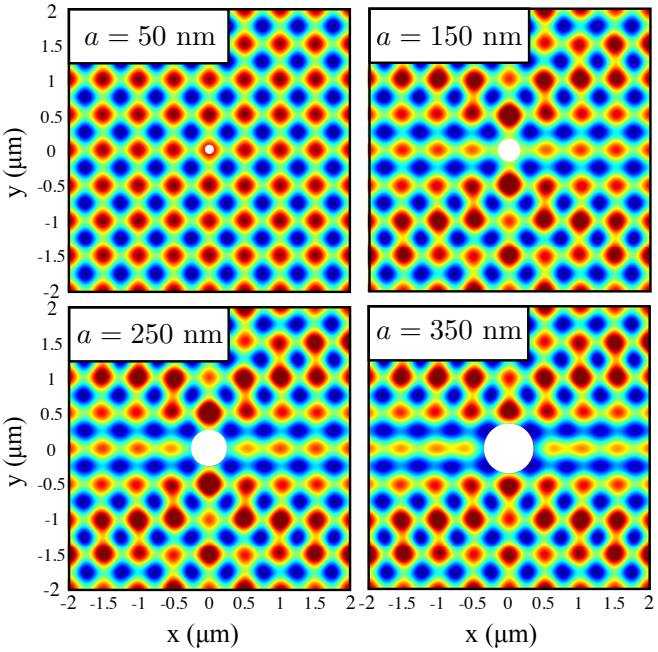


FIGURE 3.2: Lattice intensity pattern for increasing values of fiber radius when the fiber sits at a maximum of the lattice intensity. The fiber radius increases from $a = 50$ nm where no disturbance to the lattice is evident in panel (a) to $a = 350$ nm where the disturbance to the lattice is very significant in panel (d).

Distortion of the lattice due to scattering is evidently greater in the x-direction where the lattice beams are polarized parallel with the fiber surface. In Figs. 3.1 and 3.2, each plot spans an area of 4 μm $\times$ 4 μm. The other parameters are unchanged from the paper and, as in the paper, the color scale chosen varies from blue to red where the blue areas correspond to minima of the lattice intensity and red areas to maxima of the lattice intensity.

3.3 Conclusions and Future Work

While our work demonstrates that optical nanofibers can be used to locally address atoms in an optical lattice, the introduction of the quantum gas microscope half a decade ago [29] has provided a much more versatile and less invasive way of achieving the same. These systems allow a laser beam to be focused below the diffraction limit, so that individual lattice sites can be addressed. This advance, in

combination with the advent of schemes for manipulating and selectively removing atoms from optical lattices as in [69], is a significant step forward towards the realization of scalable quantum computers with optical lattices, see for example [24–26].

While therefore optical nanofibers are unlikely to contribute greatly to advances in manipulating neutral atoms in optical lattices in the short term, they nevertheless posses other properties that make them attractive for use in lattices. For example the local modification of the lattice potential, especially in combination with higher order modes can be of interest in creating new and more complex geometries. Furthermore, fibers can act as cavities (see Chapter 7), and therefore offer an advantage in situations where the light levels have to be low. Finally, flipping this situation on its head, another interesting question is about the effect of the atoms on the light traveling in the fiber. A first step in this direction is discussed in Chapter 5.

Chapter 4

Shaping the Evanescent Field of Optical Nanofibers for Cold Atom Trapping

4.1 Introduction

This chapter comprises of a paper in which we present optical dipole trapping geometries for cold, neutral atoms that can be created using the evanescent fields of an optical nanofiber. The nanofiber has a diameter large enough to allow the next lowest lying family of three modes above the fundamental mode to propagate. Specifically, the four modes allowed are HE_{11}, TE_{01}, TM_{01} and HE_{21}.

The creation of helical potentials in free space has previously been considered [70, 71] where they were generated by counter-propagating Laguerre-Gauss beams with counter-directed orbital angular momenta. In this work, we show that simple adjustments to the parameters of the counter-propagating laser light traveling in a nanofiber result in significant changes to the intensity profile of the evanescent field along the direction of propagation.

A pair of counter-propagating linearly polarized beams will form a standing wave pattern. Alternatively, if the pair are circularly polarized, the standing wave that results from their superposition can take two different forms depending on whether they have the same or opposite sign. When the pair of beams are both of the same sign, the intensity pattern that results from their superposition is azimuthally symmetric. When the pair of beams have opposite sign, the resulting standing pattern is everywhere linearly polarized, the polarization direction is rotating through 2π along the direction of propagation and this results in an intensity pattern that has two maxima which take on a double helix pattern with periodicity $\frac{\lambda}{2}$.

As discussed in Chapters 2 and 3, if both a red- and blue-detuned fundamental mode are present in the fiber at the same time, the differing decay lengths of their respective evanescent fields result in a combined optical potential with a minimum at some distance from the fiber surface. The described evanescent fields can therefore be turned into a potential geometry by considering the combination of counter-propagating higher order modes with a blue-detuned field in the fundamental mode. For example, using a blue-detuned HE_{11} fundamental mode in combination with counter propagating red-detuned HE_{21} modes allows for the formation of a potential in the shape of four intertwined spirals, as shown in the schematic Fig. 4.1. The tapered waist of a nanofiber can be a few mm in length [45], allowing for many full revolutions of the trap minimum which has a spacing constant of $\lambda/2$. We demonstrate the effect of varying the polarization between circular and linear in each of the two counter-propagating HE_{21} beams on the trapping geometry. By changing the polarization from circular to linear in each of the two counter-propagating HE_{21} modes simultaneously, the four-helix configuration can be transformed into a lattice configuration. The potential barriers between traps in the azimuthal and longitudinal directions can be controlled independently.

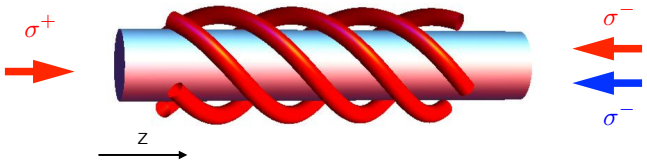


FIGURE 4.1: Two oppositely circularly polarized, counter propagating, red-detuned HE_{21} modes can be combined with a single blue-detuned HE_{11} fundamental mode to achieve a helical potential.

Simultaneous excitation of the TE_{01}, TM_{01} and HE_{21} modes has been observed in [72, 73] and a scheme allowing excitation of the TE_{01}, TM_{01} and HE_{21} modes while suppressing the fundamental mode has been demonstrated in [74]. However, selective excitation between the TE_{01}, TM_{01} and HE_{21} modes has not been achieved. At the end of the paper we discuss the modification to the 4-helix configuration due to unwanted mode mixing from the TE_{01} and TM_{01} modes.

Shortly before the publication of our work, D. Reitz and A. Rauschenbeutel, in [75], showed that a double helix potential can be created in the evanescent field of a single mode tapered fiber by combining three circularly polarized HE_{11} modes.

4.2 Paper

Manuscript Information

Manuscript Title: Shaping the evanescent field of optical nanofibers for cold atom trapping.

Journal Information: Optics Express **21**, Issue 22, 27093-27101 (2013).

Authors: Ciarán Phelan, Tara Hennessy, and Thomas Busch

DOI: 10.1364/OE.21.027093

The project was jointly conceived by Ciarán Phelan, Thomas Busch and myself. All calculations were shared between Ciarán Phelan and myself.

Shaping the evanescent field of optical nanofibers for cold atom trapping

C.F. Phelan,[1,*] **T. Hennessy,**[1,2] **and Th. Busch**[1,2]

[1]*OIST (Okinawa Institute of Science and Technology), 1919-1 Tancha, Onna-son, Okinawa 904-0495, Japan*
[2]*University College Cork, Cork, Ireland*
[*]*ciaran.phelan@oist.jp*

Abstract: We investigate trapping geometries for cold, neutral atoms that can be created in the evanescent field of a tapered optical fibre by combining the fundamental mode with one of the next lowest possible modes, namely the HE_{21} mode. Counter propagating red-detuned HE_{21} modes are combined with a blue-detuned HE_{11} fundamental mode to form a potential in the shape of four intertwined spirals. By changing the polarization from circular to linear in each of the two counter-propagating HE_{21} modes simultaneously the 4-helix configuration can be transformed into a lattice configuration. The modification to the 4-helix configuration due to unwanted excitation of the the TE_{01} and TM_{01} modes is also discussed.

© 2013 Optical Society of America

OCIS codes: (060.0060) Fiber optics and optical communications; (060.2270) Fiber characterization; (060.2280) Fiber design and fabrication; (060.2400) Fiber properties; (350.5500) Propagation .

References and links

1. L. Tong, R. R. Gattass, J. B. Ashcom, S. He, J. Lou, M. Shen, I. Maxwell, and E. Mazur, "Subwavelength-diameter silica wires for low loss wave guiding," Nature **426**, 816 (2003).
2. J. M. Ward, D. G. O'Shea, B. J. Shortt, M. J. Morrissey, K. Deasy, and S. Nic Chormaic, "Heat-and-pull rig for fiber taper fabrication," Rev. Sci. Instrumm.**77**, 083105 (2006).
3. A. Yariv, *Optical electronics*, 3^{rd} ed. (CBS College, New York 1985), chap. 3.
4. M. J. Morrissey, K. Deasy, Y. Wu, S. Chakrabarti, and S. Nic Chormaic, "Tapered optical fibers as tools for probing magneto-optical traps," Rev. Sci. Instrum. **80**, 53102 (2009).
5. K. P. Nayak, P. N. Melentiev, M. Morinaga, F. Le Kien, V. I. Balykin, and K. Hakuta, "Optical nanofiber as an efficient tool for manipulating and probing atomic fluorescence," Opt. Express **15**, 5431–5438 (2007).
6. Yu. B. Ovichnikov, S. V. Shul'ga, and V. I. Balykin, "An atomic trap based on evanescent light waves," J. Phys. B **24**, 3173 (1991).
7. F. Le Kien, V. I. Balykin, and K. Hakuta, "Atom trap and waveguide using a two-color evanescent light field around a sub wavelength-diameter optical fiber," Phys. Rev. A **70**, 063403 (2004).
8. E. Vetsch, D. Reitz, G. Sagué, R. Schmidt, S. T. Dawkins, and A. Rauschenbeutel, "Optical interface created by laser-cooled atoms trapped in the evanescent field surrounding an optical nanofiber," Phys. Rev. Lett. **104**, 203603 (2010).
9. F. Le Kien, V. I. Balykin, and K. Hakuta, "State insensitive trapping and guiding of cesium atoms using a two-color evanescent field around a subwavelength-diameter fiber," J. Phys. Soc. Japan **74**, 910–917 (2005).
10. A. Goban, K. S. Choi, D. J. Alton, D. Ding, C. Lacröute, M. Potoschnig, T. Thiele, N.P. Stern, and H.J. Kimble, "Demonstration of a state insensitive, compensated nanofiber trap," Phys. Rev. Lett. **109**, 033603 (2012).
11. C. Lacröute, K. S. Choi, A. Goban, D. J. Alton, D. Ding, N. P. Stern, and H. J. Kimble, "A state-insensitive, compensated nanofiber trap," New J. Phys. **14**, 023056 (2012).
12. G. Sagué, A. Baade, and A. Rauschenbeutel, "Blue-detuned evanescent field surface traps for neutral atoms based on mode interference in ultra thin optical fibers," New J. Phys. **10**, 113008 (2008).
13. T. Hennessy and Th. Busch, "Creating atom-number states around tapered optical fibers by loading from an optical lattice," Phys. Rev. A **85**, 053418 (2012).

#195713 - $15.00 USD Received 13 Aug 2013; revised 20 Sep 2013; accepted 23 Sep 2013; published 31 Oct 2013

14. A. V. Masalov and V. G. Minogin, "Pumping of higher-modes of an optical nano fiber by laser excited atoms," Laser Phys. Lett **10**, 075203 (2013).
15. A. Yu. Okulov, "Cold matter trapping via slowly rotating helical potential," Phys. Lett. A **376**, 650–655 (2012).
16. A. Yu. Okulov, "Superfluid rotation sensor with helical laser trap," J Low Temp Phys **171**, 397–407 (2013)
17. D. Reitz and A. Rauschenbeutel, "Nanofiber-based double-helix dipole trap for cold neutral atoms," Opt. Commun. **285**, 4705–4708 (2012).
18. A. Petcu-Colan, M. C. Frawley, and S. Nic Chormaic, "Tapered Few-Mode Fibers: Mode Evolution during Fabrication and Adiabaticity," JNOPM **20**, 293–307 (2011).
19. M. C. Frawley, A. Petcu-Colan, V. Giang Truong, and S. Nic Chormaic, "Higher order mode propagation in an optical nanofiber," Opt. Commun. **285**, 4648 (2012).
20. S. Ravets, J. E. Hoffman, L. A. Orozco, S. L. Rolston, G. Beadie, and F. K. Fatemi, "A low-loss photonic silica nanofiber for higher-order modes," Opt. Express **21**(15), 18325–18335 (2013).

1. Introduction

A sub-wavelength diameter optical fibre can be produced by heating and pulling a standard telecommunications fibre so that its waist diameter reduces from about a hundred micrometers to a few hundred nanometers [1–3]. These tapered nanofibres have many uses and one of the most prominent is in the study of atomic samples and their optical properties at ultracold temperatures. By locally probing atomic fluorescence emitted from atoms trapped in a magneto-optical trap with high efficiency, they have been used to estimate the size and profile of the atomic cloud and other trap parameters [4] and by recording the fluorescence spectrum of a small number of atoms close to the fibre surface, the effects of the short range van der Waals interaction has been investigated [5].

When light travelling in such a fiber arrives at the tapered waist, the fiber diameter is smaller than the wavelength of the propagating light and it can no longer be confined in the fiber. A considerable fraction of the power propagates outside the surface boundary in the form of an evanescent field. This presents a novel strategy for trapping and guiding atoms near the fiber surface. The evanescent field represents an intensity gradient to a nearby atom, which leads to a dipole force that is either attractive or repulsive depending on whether the guided mode is red- or blue-detuned relative to the atom's dominant transition frequency.

If both a red- and blue-detuned fundamental mode are present in the fiber at the same time, the differing decay lengths of their respective evanescent fields result in a combined optical potential with a minimum at some distance from the fiber surface [6, 7]. This technique has been experimentally demonstrated for cold caesium atoms [8]. The two-color trap can be made state insensitive by using red- and blue-detuned magic wavelengths [9,10] and vector light shifts due to the elliptic polarization of the nanofiber modes can be removed by introducing counter propagating beams [10, 11]. The evanescent field around a tapered optical fiber offers a strategy for gaining near-field access to atoms and characterising potential trapping geometries [12], and exploring possibilities for their use in more involved settings [13] is becoming a very active research area. The advantages of using fibers that are slightly bigger than single-mode fibers has also become a subject of great interest [12, 14].

Here we present a scheme for creating helicoidal potentials by combining a counter-propagating higher mode with a blue-detuned fundamental mode. These spiralling geometries can be produced by fixing the blue-detuned portion of the evanescent field in a cylindrically symmetric configuration while modifying the red-detuned portion of the evanescent field. The creation of helical potentials in free space has previously been considered [15], where they were generated by counter-propagating Laguerre Gaussian beams with counter-directed orbital angular momenta. One application of these spiralling potentials is, for example, the measurement of quantized rotations in atomic clouds [16].

In the next two sections we will first briefly introduce and review the modes that can propagate in an optical nanofiber and discuss the trapping geometries that can be constructed using

#195713 - $15.00 USD Received 13 Aug 2013; revised 20 Sep 2013; accepted 23 Sep 2013; published 31 Oct 2013
(C) 2013 OSA

the fundamental modes. In Section 3 we present different trapping geometries which can be created by exciting a specific higher order mode in the fiber and in Section 4 we consider modification of the trapping geometry due to unintended excitation of nearby modes. Finally we conclude in Section 5.

2. Trapping with the first fundamental mode

An optical nanofiber can be thought of as a very thin optical fiber with a cylindrical silica core of radius a and refractive index $n_1 = 1.452$ and an infinite vacuum clad of refractive index $n_2 = 1$. It can be created by heating and pulling commercial grade optical fiber and tapering it down such that the refractive indices that determine the guiding properties of the fiber are that of the original silica cladding and that of the surrounding vacuum. Such a thin fiber can only support a finite number of modes and the permitted propagation constants, β, can be determined numerically [3]. The field distributions associated with these modes can be found by solving Maxwell's equations and here we will just give the expressions for the evanescent part of the electric field as they will be used throughout this paper. In cylindrical polar coordinates $\{r,\phi,z\}$, these are given by [3]

$$E_r(r,\phi,z) = A\,\frac{J_l(ha)}{K_l(qa)}\,\frac{i\beta}{q^2}\left[K_l^{'}(qr) + B\frac{i\omega\mu l}{\beta r}K_l(qr)\right]e^{i(\omega t + l\phi - \beta z)}, \tag{1a}$$

$$E_\phi(r,\phi,z) = A\,\frac{J_l(ha)}{K_l(qa)}\,\frac{i\beta}{q^2}\left[\frac{il}{r}K_l(qr) - B\frac{\omega\mu}{\beta}K_l^{'}(qr)\right]e^{i(\omega t + l\phi - \beta z)}, \tag{1b}$$

$$E_z(r,\phi,z) = A\,\frac{J_l(ha)}{K_l(qa)}\,K_l(qr)e^{i(\omega t + l\phi - \beta z)}, \tag{1c}$$

where the J_l are Bessel functions of the first kind and the K_l are modified Bessel functions of the second kind. The dash denotes the derivative with respect to the argument of the Bessel function. The constant B is given by $B = \frac{i\beta l}{\omega\mu}\left(\frac{1}{q^2a^2} + \frac{1}{h^2a^2}\right)\left(\frac{J_l^{'}(ha)}{haJ_l(ha)} + \frac{K_l^{'}(qa)}{qaK_l(qa)}\right)$ and A determines the power in a given mode. The parameter q, which is the reciprocal of the decay length of the evanescent field, is defined by $q = \sqrt{\beta^2 - k_0^2 n_2^2}$ and $h = \sqrt{k_0^2 n_1^2 - \beta^2}$. The azimuthal index l counts the number of 2π phase changes of each component in a circle around the fiber axis and its sign determines the polarization of the mode.

The fields described, by Eqs. (1), are not in general transversely polarized due to the $z-$component which, for a set frequency and decreasing fiber radius, increases in magnitude (relative to the transverse components). The transverse parts of the light beams described by these formulae are circularly polarized where the sign of the index l gives the handedness of the polarization. Linearly polarized solutions can be obtained by taking superpositions of the circularly polarized beams with equal amplitude and opposite handedness.

The finite number of modes that can be supported by the fiber is determined by the ratio of the fiber radius to the wavelength of the propagating light. Under the constraint $V \equiv k_0 a\sqrt{n_1^2 - n_2^2} < 2.405$, the fiber can support only one mode, namely the fundamental mode HE_{11}. Here k_0 is the free space wave-number. The HE_{11} mode has a Gaussian intensity profile in the fiber and the shape of its evanescent field depends on three fundamental parameters of the system, the wavelength of the light, the fiber radius and the refractive index of the medium. If the light in the HE_{11} mode is circularly polarized the intensity is azimuthally uniform. If the light is quasi-linearly polarised this uniformity is broken and two intensity maxima appear at opposite sides of the fiber [7]. The intermediate cases of elliptical polarization interpolate between these two scenarios. The evanescent field decays faster for shorter wavelengths.

#195713 - $15.00 USD Received 13 Aug 2013; revised 20 Sep 2013; accepted 23 Sep 2013; published 31 Oct 2013
(C) 2013 OSA

An atom interacting with the evanescent field sees a dipole potential of the form $U = -\frac{1}{4}\alpha(\mathbf{E}^*\mathbf{E})$, where α is the atomic polarizability. It can be calculated from Eqs. (1), and any intensity gradient results in a force whose sign is given by the detuning of the light field with respect to the atoms's dominant frequency.

A simple and stable ring trap in the transverse plane around the fiber can then be created by combining a blue- and a red-detuned evanescent field, which due to their differing decay lengths results in an intensity minima at some radial distance from the fiber surface [7]. However, the attractive red-detuned intensity must overcome the blue-detuned one at a position where the van der Waals potential is negligible. Though the van der Waals expression for an atom close to a curved dielectric surface is quite complex, in our scheme it is sufficient to approximate this attractive potential by the much simpler form for an infinite plane dielectric surface which is given by $V_{vdW} = -\frac{C_3}{(r-a)^3}$ with $C_3 = 5.6 \times 10^{-49}\mathrm{Jm}^3$. This approximation is accurate for trapping minima close to the fiber surface [7]. The radial position of the minimum can be adjusted by varying the powers in the red- and blue-detuned beams and in Fig.1(a) we show typical examples for a fiber of radius $a = 200$nm and two optical fields of $\lambda_{red} = 1064$nm and $\lambda_{blue} = 700$nm, which are red- and blue-detuned from the dominant D2 transition line in caesium at $\lambda = 852$nm . The fiber radius was chosen to ensure the single mode condition is satisfied for both wavelengths and the power in the blue beam is kept fixed. By increasing the power in the red beam, a clear shift of the minimum towards the fiber surface is observed.

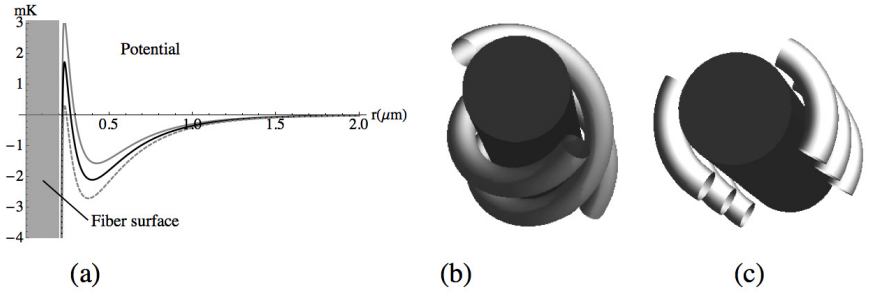


Fig. 1. (a) Potential in the radial direction for a 200nm fiber with 29 mW in the blue-detuned beam and three different powers in the red-detuned beam: 25mW (most shallow), 30 mW (intermediate depth) and 35 mW (deepest potential). Panels (b) and (c) show the shape of the potential in three dimensions when the counter propagating red-detuned modes have orthogonal circular or parallel linear polarization respectively.

It has recently been pointed out, by D. Reitz and A. Rauschenbeutel [17], that a double helix potential can be constructed in the evanescent field of a single mode optical fiber by the appropriate combination of three circularly polarized light beams. Their proposal is based on the following principle; the intensity along the propagation (z) direction can be modified by using a counter-propagating beam configuration. If both beams are linearly polarized, then a simple standing wave pattern is formed. If the beams are circularly polarized, however, the standing wave formed by their superposition can take two different forms depending on whether the components have the same or opposite handedness. In the case where the counter-propagating components have the same handedness a standing wave with circular polarization and hence azimuthal symmetry in the intensity is formed. If the components have opposite handedness the standing wave is linearly polarized everywhere with the polarization direction rotating continuously through 2π along the propagation direction, resulting in the two intensity maxima

#195713 - $15.00 USD Received 13 Aug 2013; revised 20 Sep 2013; accepted 23 Sep 2013; published 31 Oct 2013
(C) 2013 OSA

which form a double helix pattern with a periodicity of $\lambda/2$. The helical angle at the fiber surface is given by $\arctan(2\pi a/\lambda)$ [17].

Figures 1(b) and 1(c) show the different shapes of such a potential in three dimensions for different polarisations in the red-detuned beam. In (b) the counter propagating red-detuned beams have orthogonal circular polarisation and the resulting potential has the form of a double helix [17]. In (c) the beams have parallel linear polarisation and one observes the creation of a potential that is periodic in the azimuthal and longitudinal directions and has similarities to having two one-dimensional optical lattices aligned along opposite sides of the fiber. The trapping frequency in the radial and azimuthal direction can be determined from $\omega_r = \sqrt{\frac{\partial_r^2 U(r_{min})}{m}}$ where m is the mass of caesium and one finds typical values of 500KHz in the radial direction and 150KHz in the azimuthal one.

3. Trapping using the higher order HE_{21} mode

If the parameter V is increased beyond the value of 2.405, simply by increasing the fiber diameter, three additional modes will successively be allowed to propagate. These are the HE_{21}, TE_{01} and TM_{01} modes. In the weakly guiding approximation, all three of these modes correspond to the LP_{11} mode which resembles the free space Laguerre Gaussian LG_{01} mode. The strong confinement of the mode by the nanofiber causes the LP_{11} mode to split into three modes with different propagation constants.The transverse intensity and polarization profiles of these three modes are shown in Fig 2.

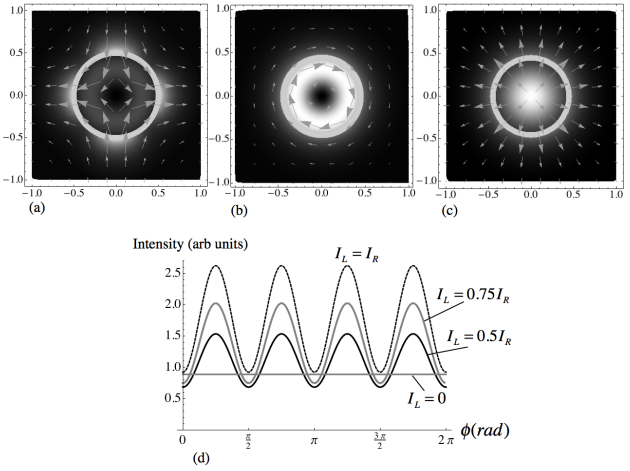


Fig. 2. (a) Intensity and polarization vectors for the HE_{21} mode with quasi-linear polarization, for a 500nm diameter fiber with 1064nm wavelength light. (b) and (c) show the TE_{01} and TM_{01} modes for the same parameters. The ring marks the fiber vacuum boundary. (d) shows the intensity in the azimuthal direction for the HE_{21} mode, at 100nm from the fiber surface, for four different polarization states where $I_{L/R}$ denotes intensity in left/right circularly polarized modes.

It is noteworthy that the TM_{01} mode has significant on axis intensity, due to the large z-component of the field in the nanofiber, whereas the TE_{01} and HE_{21} modes have the same doughnut shape as the LP_{11}. The transverse part of the polarization of the TE_{01} and TM_{01} modes is linear with a 2π rotation of polarization direction.

Since trapping geometries based on superpositions of the TE_{01} modes with both the HE_{21}

#195713 - $15.00 USD Received 13 Aug 2013; revised 20 Sep 2013; accepted 23 Sep 2013; published 31 Oct 2013
(C) 2013 OSA

and the HE_{11} modes are known to be very versatile [12], we present in the following an analysis of the trapping geometries that can be created by combining the HE_{21} mode and the HE_{11} fundamental mode. We will first consider a clean excitation and then include effects from unintended excitations of the TE_{01} and TM_{01} modes on these potentials. Even though these unintended excitations change the trapping potential, we show that this can actually lead to a new category of interesting geometries.

The HE_{21} mode can be either circularly or linearly polarized, where the linearly polarized one is a direct combination of right and left circularly polarized beams. In this case the transverse part of the polarization vector undergoes a 2π rotation in a circuit around the fiber axis, while the polarization vector rotates in the opposite sense to the circuit taken so that the electric field vector is orthogonal to the fiber surface at four points. The evanescent field must be continuous across the fiber boundary at these points and this results in four intensity maxima along the azimuthal direction. These polarization vectors are shown superimposed on the intensity profile at one instant of time in Fig 2(a). The circularly polarized HE_{21} mode has an azimuthally symmetric intensity profile (not shown).

The variation in azimuthal intensity distribution for different polarization states of the HE_{21} mode is shown in Fig. 2(d) and four intensity maxima are clearly visible, which become more pronounced the less circularly polarized the beam is. In these figures the fiber radius is 500nm so that the HE_{21} mode is allowed to propagate for 1064nm wavelength light in a silica fiber with a decay length of $1/q = 0.52\ \mu$m

Counter-propagating HE_{21} modes can broadly be achieved in three different ways, which lead to three different classes of standing wave pattern: (a) counter-propagating circularly polarized modes of the same handedness , (b) counter-propagating quasi-linearly polarized modes, and (c) counter-propagating circularly polarized modes of opposite handedness. Two counter-propagating quasi-circularly polarized modes with the same handedness form a cylindrically symmetric standing wave (case (a)), which can be used to create symmetric, equally spaced disconnected potential rings around the fiber, see Fig. 3(a). Counter-propagating two quasi-linearly polarized HE_{21} modes (case (b)), results in a standing wave with four intensity maxima per circuit of the fiber, which allows to create a regular lattice of traps with periodic boundary conditions around the fiber, see Fig. 3(b). And two counter propagating HE_{21} modes with opposite quasi-circular polarization (case (c)) will combine to form a linearly polarized mode like that shown in Fig 2(c) with the polarization vectors rotating with propagation direction. This results is an evanescent field consisting of four intertwined helices, leading to a potential of the same shape (see Fig. 3(c)).

Switching between these different standing wave configurations by smoothly varying the polarization is experimentally conceivable. In the upper row of Fig. 4 we show how the standing wave formed by two counter-propagating modes with the same quasi-circular polarization transforms into a two-dimensional lattice of traps by simply changing the polarization from circular to linear in each of the counter propagating modes simultaneously. The same method transforms the four helix standing wave into the lattice (see middle row of Fig. 4) and in order to transform the four helix potential into the circularly symmetric standing wave one of the circularly polarized modes, say left circularly polarized, is held constant while the other is smoothly changed from right to left (lower row in Fig. 4).

#195713 - $15.00 USD Received 13 Aug 2013; revised 20 Sep 2013; accepted 23 Sep 2013; published 31 Oct 2013
(C) 2013 OSA

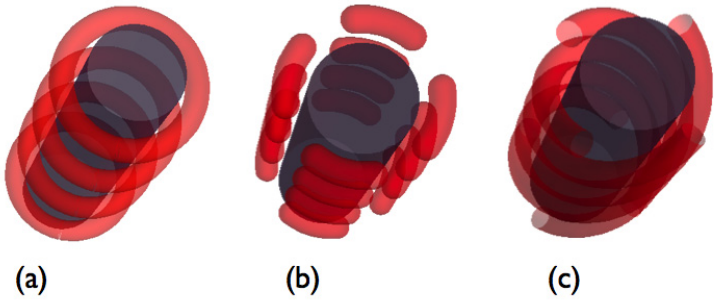


Fig. 3. Potential shapes corresponding to three types of standing wave (a) the shape of the potential in three dimensions when the modes have identical circular polarizations (b) the shape of the potential in three dimensions when the modes are linearly polarized, (c) the shape of the potential in three dimensions when the modes have orthogonal circular polarizations

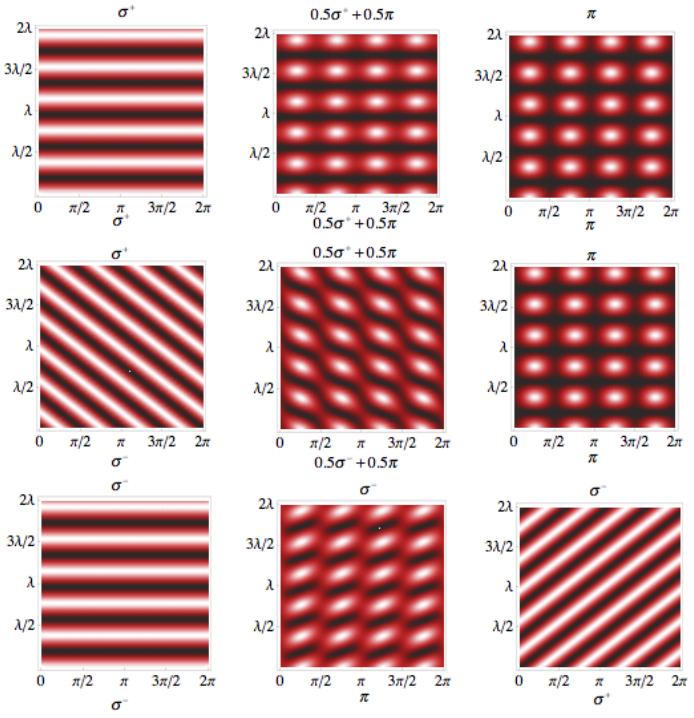


Fig. 4. Intensity in the $\{r, \phi\}$ plane as a circularly symmetric standing wave is transformed into the lattice (upper row), a four helix standing wave is transformed into the lattice (middle row) and a circularly symmetric standing wave is transformed into the four helix standing wave (lower row).

To use the above intensity patterns to trap caesium atoms, we consider introducing a 700nm fundamental HE_{11} mode, which, for the fiber parameters specified above, has an evanescent

#195713 - $15.00 USD Received 13 Aug 2013; revised 20 Sep 2013; accepted 23 Sep 2013; published 31 Oct 2013
(C) 2013 OSA

field decay length of $1/q_{blue} = 0.12\mu$m. The three dimensional geometries of these potentials for counter-propagating modes with identical circular polarization, counter-propagating modes with parallel linear polarization and for counter-propagating modes with orthogonal circular polarization are shown in in Figs. 3(a),(b) and (c), respectively. The distance between potential minima in the azimuthal direction is approximately a wavelength for the chosen parameters and depends on the radial position of the potential minimum, which can be modified by varying the ratio of power in the red-detuned field to that in the blue. Here the potential minimum, for 26 mW in the 1064nm field and 110 mW in the blue field, is located at 145nm from the fiber surface.

Fitting the radial profile in the vicinity of the trapping minimum to a harmonic oscillator potential $\frac{1}{2}m_C\omega_r^2 r^2$, where m_C is the mass of caesium, leads to an estimate of 400kHz for $\omega_r/2\pi$. The same method leads to an estimate of 240kHz for the azimuthal trapping frequency $\omega_\phi/2\pi$. Note that the potential barriers between the traps can be smoothly removed in the longitudinal direction by lowering the power in one of the counter-propagating beams and independently in the azimuthal direction by changing the polarization of the mode from linear to circular.

4. Effects of mode-mixing

Controlling the distribution of power between the available modes in a nanofiber is an experimentally open problem. Depending on the shape of the tapering region and the quality of the beam injected initially, the modes present in the tapered waist can have different populations

Simultaneous excitation of the TE_{01}, TM_{01} and HE_{21} modes has been demonstrated [18, 19]. Recently, a scheme has been presented [20] which allows excitation of the TE_{01}, TM_{01} and HE_{21} modes while supressing contamination of the fundamental mode to less than 1%. However, a clean excitation of the HE_{21} mode has not yet been reported. In the following we will look at the effects the presence of unintended excitation of the TE_{01} and TM_{01} modes has on the HE_{21} based potentials. So far, our scheme has assumed sole excitation the HE_{21} mode. However if power is passed from the HE_{21} to the TE_{01} and TM_{01} modes, the 4-helix potential is modified and in general the potential changes from having four traps per azimuth to only two (see Fig. 5). The effect is stronger in the case of power transfer to the TE_{01} mode. This can be explained by referring back to Fig. 2 where it can be seen that the TE_{01} and TM_{01} modes can interfere destructively with the HE_{21} mode at two azimuthal positions where the polarizations match. In the case of the radially polarized TE_{01} mode this effect will be greater since the HE_{21} evanescent field is strongest where the polarization is radial. In this figure there is $50mW$ propagating in the fundamental mode and $2mW$ shared between the three higher modes.

#195713 - $15.00 USD Received 13 Aug 2013; revised 20 Sep 2013; accepted 23 Sep 2013; published 31 Oct 2013
(C) 2013 OSA

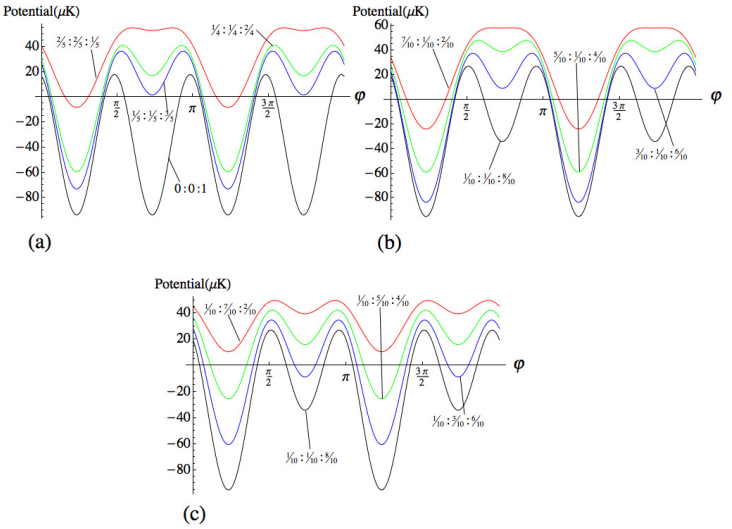


Fig. 5. The modification of the 4-helix potential as power is transferred from HE_{21} to (a) TE_{01} and TM_{01} in equal measure, (b) TE_{01} with the power in TM_{01} held constant and (c) TM_{01} with TE_{01} held constant. The ratios represent the fraction of power in each mode as TE_{01}:TM_{01}:HE_{21}

5. Conclusion

By considering a tapered fiber with a diameter large enough to allow the next lowest modes above the fundamental mode to propagate, we have shown that a trapping potential in the shape of four intertwined helices can be created. This is achieved by combining red- and blue-detuned modes in a specific way and in particular by counter-propagating the red-detuned HE_{21} modes. This 4-helix configuration can be transformed into a rectangular lattice of traps wrapped around the cylinder by adjusting the polarisations of the counter-propagating beams. The potential barriers between traps in the azimuthal and longitudinal directions can be controlled independently. We have also considered the effects on this trapping geometry from unintended transfer of power from the HE_{21} to the TE_{01} and TM_{01} modes. It is apparent that, were it possible to selectively couple to the available modes with strategically chosen relative intensities, a large number of interesting trapping geometries could be achieved.

Acknowledgments

This work was supported by Science Foundation Ireland under project number 10/IN.1/I2979

#195713 - $15.00 USD Received 13 Aug 2013; revised 20 Sep 2013; accepted 23 Sep 2013; published 31 Oct 2013

(C) 2013 OSA

4.3 Conclusions and Future Work

Evanescent field based nanofiber traps provide a powerful experimental platform for quantum optics and make it possible to probe and efficiently interface trapped atoms. These nanofiber traps have great flexibility and potential for various applications in fundamental research and in technology fields. We have shown that these traps have a high degree of tunability, especially when combining higher order modes.

The kind of helical trap presented here has advantages over the free-space helical potentials considered in [70, 71], in that it is not restricted in the maximum length over which it can be made uniform. There is also the possibility of preparing nanofibers with a non-uniform radius and so to create helical or lattice potentials with varying pitch and circumference.

It was pointed out in [75], that in experiments with polar molecules [76] or charged particles [77, 78] long range interaction is present and bound states with a fixed inter-particle distance can occur in helical potentials. This presents an opportunity for investigating zero-temperature second-order liquid to gas transitions [76].

Chapter 5

Detecting Atoms Trapped In An Optical Lattice Using a Tapered Optical Nanofiber

5.1 Introduction

The ability to control the spatial position of single atoms to a high degree of precision is important for controlling collisions and interactions. It is therefore necessary to develop diagnostic tools that allow one to measure the position of a single atom with very high fidelity. A number of methods to achieve this have been developed in recent years, ranging from advanced de-convolution algorithms [79] to the recent development of atom microscopes [29].

In the work I present in this section we study the emission rates that can be achieved from a row of emitting atoms into the guided modes of an optical nanofiber in a configuration where the axis of the fiber is aligned perpendicularly to the row of regularly separated atoms and show that such a setup allows one to distinguish contributions from individual lattice sites. The possibility to detect single atoms using a sub-wavelength-diameter fiber and the fact that single photons spontaneously emitted from the atoms can be readily guided into the fiber modes has

been shown [80]. Furthermore, a recent work by Masalov and Minogin had predicted that the scattering rates into the fiber from the first three higher order modes are generally about ten times higher than for the fundamental mode [81]. This was subsequently measured by Kumar et al. [82].

The parameters governing the emission characteristics of an atom into the guided mode of a nanofiber are the fiber radius a, the atom position and the transition wavelength λ_0, and the orientation of the dipole oscillation. The scheme presented here depends on the capability to align the atomic dipoles so that they oscillate in the x-y plane, transverse to the fiber. We calculate the spatial emission profile of an array of two-level atoms as detected by a tapered fiber and show that an optical nanofiber can be used to resolve spontaneous emission from individual atoms (using ^{133}Cs as an example) trapped in an optical lattice. We compare the use of a single mode fiber (a fiber supporting only the first fundamental mode HE_{11}), to the use of a fiber which supports the first four available modes.

5.2 Paper

Manuscript Information

Manuscript Title: Detecting atoms trapped in an optical lattice using a tapered optical nanofiber.

Journal Information: Optics Express **22**, Issue 26, 32509-32519 (2014).

Authors: Tara Hennessy and Thomas Busch

DOI: 10.1364/OE.22.032509

The idea for the project was developed jointly between myself and Thomas Busch. All calculations were carried out by myself.

Detecting atoms trapped in an optical lattice using a tapered optical nanofiber

T. Hennessy[1,2*] **and Th. Busch**[1]

[1]*Okinawa Institute of Science and Technology Graduate University, Okinawa, Japan*
[2]*Physics Department, University College Cork, Cork, Ireland*

[*]*tara.hennessy@oist.jp*

Abstract: Optical detection of structures with dimensions smaller than an optical wavelength requires devices that work on scales beyond the diffraction limit. Here we present the possibility of using a tapered optical nanofiber as a detector to resolve individual atoms trapped in an optical lattice in the Mott insulator phase. We show that the small size of the fiber combined with an enhanced photon collection rate can allow for the attainment of large and reliable measurement signals.

© 2014 Optical Society of America

OCIS codes: (020.1335) Atom optics; (040.0040) Detectors; (060.2370) Fiber optics sensors.

References and links

1. M. Karski, L. Förster, J. M. Choi, W. Alt, A. Widera, and D. Meschede, "Nearest-neighbor detection of atoms in a 1D optical lattice by fluorescence imaging," Phys. Rev. Lett. **102**, 053001 (2009).
2. W. S. Bakr, J. I. Gillen, A. Peng, S. Fölling, and M. Greiner, "A quantum gas microscope for detecting single atoms in a Hubbard-regime optical lattice," Nature **462**, 74–77 (2009).
3. J.M. Ward, V. H. Le, A. Maimaiti, and S. Nic. Chormaic, "Optical micro- and nanofiber pulling rig," Rev. Sci. Instrum. **85**, 111501 (2014).
4. F. Le Kien, S. Dutta-Gupta, K. P. Nayak, and K. Hakuta, "Nanofiber-mediated radiative transfer between two distant atoms," Phys. Rev. A **72**, 063815 (2005).
5. K. P. Nayak and K. Hakuta, "Single atoms on an optical nanofiber," New Journal of Physics **10**, 053003 (2008).
6. K. P. Nayak, P. N. Melentiev, M. Morinaga, F. Le Kien, V. I. Balykin, and K. Hakuta, "Optical nanofiber as an efficient tool for manipulating and probing atomic fluorescence," Opt. Express **15** (9), 5431–5438 (2007).
7. R. Yalla, F. Le Kien, M. Morinaga, and K. Hakuta, "Efficient channeling of fluoresence photons from single quantum dots into guided modes of optical nanofiber," Phys. Rev. Lett. **109**, 063602 (2012).
8. M. Fujiwara, K. Toubaru, T. Noda, H-Q. Zhao, and S. Takeuchi, "Highly efficient coupling of photons from nanoemitters into single-mode optical fibers," Nano Lett. **11**, 4362-–4365 (2011).
9. F. Le Kien and K. Hakuta, "Cooperative enhancement of channeling of emission from atoms into a nanofiber," Adv. Nat. Sci.: Nanosci. Nanotechnol. **3**, 035001 (2012).
10. T. Søndergaard and B. Tromborg, "General theory for spontaneous emission in active dielectric microstructures: Example of a fiber amplifier," Phys. Rev. A **64**, 033812 (2001).
11. F. Le Kien, S. Dutta-Gupta, V. I. Balykin, and K. Hakuta, "Spontaneous emission of a cesium atom near a nanofiber: Efficient coupling of light to guided modes," Phys. Rev. A **72**, 032509 (2005).
12. A.V. Masalov and V.G. Minogin, "Pumping of higher-modes of an optical nanofiber by laser excited atoms," Laser Phys. Lett. **10**, 075203 (2013).
13. R. Kumar, V. Gokhroo, A. Maimaiti, K. Deasy, M. C. Frawley, and S. Nic Chormaic, "Interaction of laser-cooled ^{87}Rb atoms with higher order modes of an optical nanofiber," arXiv:1311.6860.
14. M.Z. Hasan and C.L. Kane, "Colloquium: Topological insulators," Rev. Mod. Phys. **82**, 3045 (2010).
15. M. Lewenstein, A. Sanpera, and V. Ahufinger, *Ultracold Atoms in Optical Lattices: Simulating Quantum Many-Body Systems* (Oxford University, 2012).
16. See, for example, J.D. Jackson, *Classical Electrodynamics*, 3rd ed. (John Wiley & Sons, 1998).
17. M. Greiner, O. Mandel, T. Esslinger, T.W. Hänsch, and I. Bloch, "Quantum phase transition from a superfluid to a Mott insulator in a gas of ultracold atoms," Nature **415**, 39–44 (2002).
18. C. Becker, P. Soltan-Panahi, J. Kronjäger, S. Dörscher, K. Bongs, and K. Sengstock, "Ultracold quantum gases in triangular optical lattices," New J. Phys. **12**, 065025 (2010).

#225079 - $15.00 USD Received 16 Oct 2014; revised 4 Dec 2014; accepted 7 Dec 2014; published 24 Dec 2014
(C) 2014 OSA

19. L. Tong, R.R. Gattass, J.B. Ashcom, S. He, J. Lou, M. Shen, I. Maxwell, and E. Mazur, "Subwavelength-diameter silica wires for low-loss optical wave guiding," Nature **426**, 816–819 (2003).
20. E. Vetsch, D. Reitz, G. Sagué, R. Schmidt,S.T. Dawkins, A. Rauschenbeutel, " Optical interface created by laser-cooled atoms trapped in the evanescent field surrounding an optical nanofiber," Phys. Rev. Lett. **104**, 203603 (2010)
21. M.J. Morrissey, K. Deasy, Y. Wu, S. Chakrabarti and S. Nic Chormaic, "Tapered optical fibers as tools for probing magneto-optical trap characteristics," Rev. Sci. Instrum. **80**, 053102 (2009).
22. The refractive index n_1 of fused silica (SiO_2) can be calculated using a Sellmeier-type dispersion formula , taking the refractive index of the vacuum $n_2 = 1$

$$n_1 - 1 = \frac{0.696166\lambda^2}{\lambda^2 - (0.068404)^2} + \frac{0.407942\lambda^2}{\lambda^2 - (0.116241)^2} + \frac{0.897479\lambda^2}{\lambda^2 - (9.896161)^2}$$

where λ is in units of μm.
23. See, for example; D. Marcuse, *Light Transmission Optics* (Krieger, 1989); A. W. Snyder and J. D. Love, *Optical Waveguide Theory* (Chapman and Hall, 1983).
24. A. Steffen, A. Alberti, W. Alt, N. Belmechri, S. Hild, M. Karski, A. Widera, and D. Meschede, "Digital atom interferometer with single particle control on a discretized space-time geometry," Proc. Natl. Acad. Sci. U. S. A. **109**, 9770—9774 (2012).
25. M. Boustimi, J. Baudon, P. Candori, and J. Robert, "van der Waals interaction between an atom and a metallic nanowire," Phys. Rev. B **65**, 155402 (2002).
26. F. Le Kien, V.I. Balykin, and K. Hakuta, "Atom trap and waveguide using a two-color evanescent light field around a subwavelength-diameter optical fiber," Phys. Rev. A **70**, 063403 (2004).
27. D. Jaksch, H.J. Briegel, J.I. Cirac, C.W. Gardiner, and P. Zoller, "Entanglement of atoms via cold controlled collisions," Phys. Rev. Lett. **82**, 1975–1978 (1999).
28. T. Hennessy and Th. Busch, "Creating atom-number states around tapered optical fibers by loading from an optical lattice," Phys. Rev. A **85**, 053418 (2012).
29. Síle Nic Chormaic, Okinawa Institute of Science and Technology Graduate University, Okinawa, Japan, (personal communication, 2014).

1. Introduction

Developing tools to control all degrees of freedom of single quantum particles is one of the fundamental aims of the area of quantum engineering. Over the past few decades precision spectroscopy has made significant strides towards achieving this goal for the internal degrees of freedom of atoms and ions, and more recently electro-magnetic trapping technologies have made similar advances in controlling the external degrees. By today; magnetic, optical and magneto-optical traps can be designed to trap and control large or small numbers of atoms, and even single particles. One example of the latter are optical microtraps, in which single atoms can be localized to an area with dimensions smaller than an optical wavelength. Such traps can, for example, be based on highly focussed laser beams or small scale interference patterns, with the most famous example of the latter being optical lattices. Taking advantage of the existence of the so-called Mott transition at low temperatures, such lattices allow for the creation of periodically spaced arrays of individually trapped atoms in one, two or three dimensions.

The ability to control the spatial position of single atoms to a high degree of precision is, for example, important in controlling distance dependent interactions. It is therefore necessary to develop diagnostic tools that can measure the position of a single atom with very high fidelity. A number of technologies have been developed during recent years and among these are de-convolution algorithms [1] and atom microscopes [2]. The latter rely on an advanced optical setup and the ability to position optical elements very close to the atoms. In this work we suggest another method which makes use of technology developed in the emerging area of sub-wavelength diameter optical fibers by calculating the spatial emission profile of an array of periodically spaced two-level atoms in the presence of such a fiber. Optical nanofibers, which are created by placing industrial grade silica fiber over a hot flame and pulling both ends (for a

#225079 - $15.00 USD Received 16 Oct 2014; revised 4 Dec 2014; accepted 7 Dec 2014; published 24 Dec 2014
(C) 2014 OSA

review of this technology see [3]), support only a small number of modes and can therefore be thought of as cavities into which enhanced emission rates can be achieved [4–9]. The emission characteristics of an atom into a nanofiber in general depends on the radius of the fiber, the distance from the atom, the wavelength of the transition and the orientation of the atomic dipole [10]. It has been shown that a single-mode fiber of radius 200 nm can collect up to 28% of the spontaneous emission of a cesium atom when the atom is sitting at the fiber surface [11]. In larger fibers, which support higher order modes as well, even higher collection rates can be achieved [12, 13].

Here we study the coupling between a row of atoms and the guided modes of a perpendicularly aligned optical nanofiber and show that such a setup can resolve the position of single atoms on length scales that are typical for optical lattices. It can also allow for the detection of empty sites in a Mott insulator state or be used in a time-dependent way to identify, for example, edge states [14]. In the following we first briefly introduce the geometry of the setup (Section 2), then present the expressions for the collected radiation (Section 3), discuss the obtained results (Section 4), present an application of our scheme to a relevant dynamical situation in order to demonstrate its limits (Section 5), and make concluding remarks (Section 6).

2. Optical lattices and nanofibers

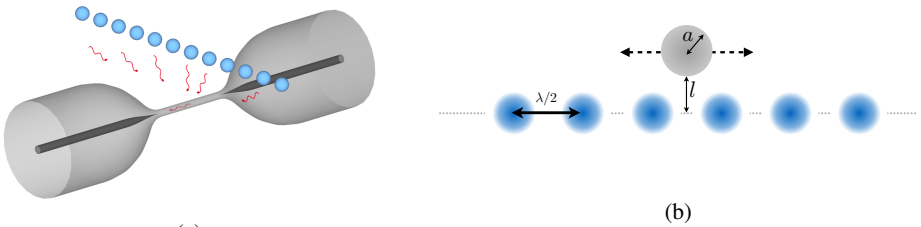
Let us first briefly review the components of the suggested setup. Optical lattices are formed by pairs of counter-propagating lasers which interfere to create spatially periodic arrays of microtraps by employing the dipole force of the standing wave laser light field [15]. The simplest case of an optical lattice trapping potential is given by a one-dimensional model, in which two counter-propagating laser beams interfere. This results in a standing wave for the optical intensity given by $I(z) = I_0 \sin^2(kz)$, where $k = 2\pi/\lambda$ is the free space wave number of the laser light and I_0 is the maximum intensity of the laser beam. The periodicity of the intensity is $\lambda/2$ and the spatially varying ac Stark shift then forms a potential for the induced dipole moment, $\mathbf{d}$, of the atom given by

$$U_{\rm dip} = -\frac{1}{2}\langle \mathbf{d}\cdot\mathbf{E}\rangle = -\frac{1}{2\varepsilon_0 c}\,{\rm Re}(\alpha) I. \tag{1}$$

Here ε_0 is the vacuum permittivity, c is the speed of light and $\alpha(\omega_L)$ is the optical polarizability, which depends on the frequency of the laser field, $\mathbf{E}$, see [16]. By using light which is blue-detuned ($\omega_L > \omega_0$) or red-detuned ($\omega_L < \omega_0$) with respect to the atomic transition ω_0, the atoms can be forced to gather at the nodes or anti-nodes of the laser intensity pattern, respectively. Higher dimensional lattices can simply be created by introducing pairs of counter propagating lasers in the other spatial directions [17], and different spatial geometries can be achieved by varying the angle between these beams [18]. Optical lattices typically have lattice constants in the range between 400 nm and 700 nm and throughout this work we assume a lattice spacing of $\lambda/2 = 640$ nm. The atom we consider is ^{133}Cs, whose ground state has its dominant (D_2) line at λ_0=852 nm.

Cold atoms trapped in optical lattices provide an adaptable quantum system in which a variety of matter-wave quantum phenomena can be engineered and observed. Notably, it has been possible to induce a quantum phase transition from a superfluid to a Mott insulator state by controlling the tunneling interaction between different sites. This was first demonstrated experimentally in 2002 [17], when a Mott insulator state with a well-defined number of atoms per lattice site was achieved using ^{87}Rb. However, until recently it was only possible to demonstrate this phase transition by detecting the loss of coherence using a time-of-flight interferometric measurement, and only the development of so-called atom microscopes has made it possible to resolve single sites inside the lattice [2]. The technological difficulty in constructing a device that can resolve single lattice sites lies in overcoming the diffration limit and allowing for sub-

#225079 - $15.00 USD Received 16 Oct 2014; revised 4 Dec 2014; accepted 7 Dec 2014; published 24 Dec 2014
(C) 2014 OSA



(a) (b)

Fig. 1: (a) Schematic of a tapered optical nanofiber aligned perpendiculary to a periodic array of trapped atoms. In reality the untapered ends have a radius on the order of 125 μm and the nanofiber waist is on the order of hundreds of nanometers. The typical length of the tapered region is between 3 and 10 mm, depending on the tapering technique employed [3]. (b) Top-view of the fiber and atom configuration. The dipoles are arranged in a line (so that they lie end to end) and perpendicular to the fiber. Not drawn to scale.

wavelength resolution. The atom microscope does this by using advanced optical elements to focus the light to below the diffraction limit.

A second strategy for going beyond the diffraction limit is to use sensors of subwavelength size and here we study an approach of this kind based on collecting the optical emission using the guided modes of a nanofiber. Recent advances in technology have made it possible to produce tapered fibers with radii as small as a few hundred nanometres [3,19], in which only a very small number of modes can propagate. These devices can be fully integrated in ultracold atom experiments [20,21] and we suggest a geometry in which a fiber is aligned perpendicularly to a row of regularly spaced atoms (see Fig. 1) in order to collect the atomic fluorescence. Due to the small radius of the fiber, such a setup allows for a good spatial resolution of the atomic distribution.

As already mentioned above, the emission characteristics of an atom into a nanofiber depend on the radius of the fiber, the distance between the atom and the fiber, the wavelength of the transition and the orientation of the atomic dipole [10]. In the following we will investigate the use of single- (supporting only HE_{11}) and multi-mode fibers (supporting HE_{11}, HE_{21}, TE_{01}, TM_{01}), as the latter are known to allow for much higher collection rates [12,13]. We consider a one-dimensional optical lattice in which ^{133}Cs atoms are individually trapped with a separation distance $\lambda/2 = 640$ nm and assume that all dipoles are aligned. For any position of the fiber we therefore only include a contribution from the component of the dipole along the line connecting the fiber centre and the atom. The distance between the surface of the fiber and the axis of the row of atoms is given by l and the fiber radius by a (see Fig. 1(b)). The fiber we consider is made of silica, which for a photon of $\lambda_0 = 852$ nm has a refractive index of $n_1 = 1.4525$ [22]. The refractive index of the vacuum, n_2 , is equal to 1.

Following closely the approach of [12] to calculate the emission rate into the fiber, let us first consider the emission rate into free space,

$$W_0 = \frac{1}{4\pi\varepsilon_0}\frac{4d^2\omega_0^3}{3\hbar c^3}\,, \tag{2}$$

where d is the matrix element of the atomic dipole moment, ε_0 is vacuum permittivity and ω_0 is the atomic frequency. This emission can excite four guided modes given by the four possible combinations of $\pm\sigma$ polarization and $\pm z$ propagation direction in the fiber. Normalizing the

#225079 - $15.00 USD Received 16 Oct 2014; revised 4 Dec 2014; accepted 7 Dec 2014; published 24 Dec 2014
(C) 2014 OSA

emission rate into each of these modes with respect to the full emission rate, we arrive at

$$W_{\text{guid}} = W_0 \frac{3\lambda_0{}^2 \beta'}{8\pi} |\mathbf{E}|^2 \,, \tag{3}$$

where $\mathbf{E}$ is made up of the mode functions of the electric parts of the relevant mode outside of the nanofiber. The parameter β' is the reciprocal of the group velocity and calculated as $\beta' = d\beta/dk$, where the propagation constant β is determined by ensuring continuity between the field components outside of the nanofiber ($r > a$) with the ones at the surface of the fiber [23]. This leads to an implicit equation that has to be solved numerically as a function of the system parameters.

For the presented scheme to work, one has to compare the lifetime of the Mott insulator state with the lifetime of the fluorescence transition and the technical ability to scan the fiber in front of the lattice or vice versa. Since the first two time-scales are orders of magnitude different and since it is technically possible to move atoms in optical lattices over tens of micrometers with high precision [24], the presented scheme can in principle be realized with currently available technology.

3. Emission rates into the four modes of interest

Substituting the electric field components of the relevant modes into Eq. (3) gives four expressions for the rates of emission into the four modes of interest to us [12]. These are the fundamental HE_{11}, TE_{01}, TM_{01} and HE_{21} modes, each propagating into either $\pm z$ with circular polarization $\pm\sigma$

$$\begin{aligned}
W_{\text{HE}_{11}}(r) =& W_0 \frac{3\lambda^2\beta'}{8\pi^2 a^2} \left(\frac{1}{n_1^2 N_1 + n_2^2 N_2} \right) \frac{J_1^2(ha)}{K_1^2(qa)} \\
&\times \left[K_1^2(qr) + \frac{\beta^2}{2q^2} \left[(1-s)^2 K_0^2(qr) + (1+s)^2 K_2^2(qr) \right] \right], \qquad (4) \\
W_{\text{TE}_{01}}(r) =& W_0 \frac{3\lambda^2\beta'}{8\pi^2 q^2 a^4} \left(\frac{1}{n_1^2 P_1 + n_2^2 P_2} \right) K_1^2(qr), \qquad (5) \\
W_{\text{TM}_{01}}(r) =& W_0 \frac{3\lambda^2\beta'}{8\pi^2 a^2} \left(\frac{1}{n_1^2 Q_1 + n_2^2 Q_2} \right) \frac{\beta^2}{q^2} K_0^2(qr) K_1^2(qr), \qquad (6) \\
W_{\text{HE}_{21}}(r) =& W_0 \frac{3\lambda^2\beta'}{8\pi^2 a^2} \left(\frac{1}{n_1^2 R_1 + n_2^2 R_2} \right) \frac{J_2^2(ha)}{K_2^2(qa)} \\
&\times \left[K_2^2(qr) + \frac{\beta^2}{2q^2} \left[(1-u)^2 K_1^2(qr) + (1+u)^2 K_3^2(qr) \right] \right]. \qquad (7)
\end{aligned}$$

In the above equations the J_n are Bessel functions of the first kind, the K_n are modified Bessel functions of the second kind, a is the fiber radius and

$$q = \sqrt{\beta^2 - {n_2}^2 k^2} \quad \text{and} \quad h = \sqrt{n_1^2 k^2 - \beta^2}. \tag{8}$$

The explicit expressions for the constants N, P, Q, R, s and u are given in the appendix.

The number of modes a nanofiber in vacuum can support is related to the quantity $V = \frac{a\omega_0}{c}\sqrt{n_1^2(\omega_0) - 1}$ [23] and for $V < 2.405$ the single-mode condition is satisfied. This means that only the HE_{11} mode can travel in the fiber and for ^{133}Cs, with $\lambda_0 = 852$ nm, this corresponds to keeping the fiber radius in the region where $a < 309.6$ nm. The range of radii for which

#225079 - $15.00 USD Received 16 Oct 2014; revised 4 Dec 2014; accepted 7 Dec 2014; published 24 Dec 2014
(C) 2014 OSA

the first four modes are supported is $0.363\lambda_0 < a < 0.580\lambda_0$, which corresponds to 309.6 nm $< a <$ 494.2 nm.

Since atoms trapped in a Mott insulator state have a rather large separation of $\lambda/2$, they can be treated as independent dipoles and it is appropriate to sum the normalized rates of emission into each of the modes. At every position we therefore sum over all of the atoms and over all of the modes. In all the results we present the emission rates are normalized with respect to emission into free space, W_0.

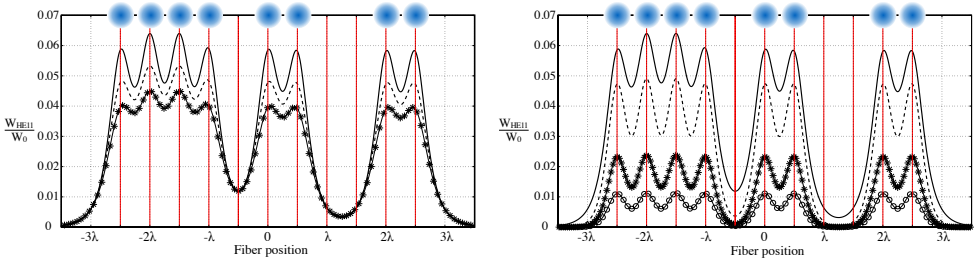
4. Results

To show that the spatially inhomogeneous emissions rate originating from a row of atoms trapped in a one-dimensional optical lattice can be resolved using a nanofiber, we calculate the emission rate into the fiber as a function of the position of the fiber with respect to the position of the atoms. Since this rate depends on the distance from the atoms, spatial resolution with high visibility can be expected if the fiber is close to the atoms.

Table 1: Numerical values of β and β' for the fundamental HE_{11} mode for the $\lambda_0 = 852$ nm transition in ^{133}Cs for a fused silica fiber with $n_1 = 1.4525$.

Fiber Radius	β	β '
150 nm	7.471×10^6	1.115
200 nm	7.883×10^6	1.364
250 nm	8.436×10^6	1.517
300 nm	8.919×10^6	1.566

We first consider the use of single-mode fibers, which support the HE_{11} mode only. This means that we are restricted to fibers with a radius of $a < 309.6$ nm and in Table 1 the numerical values for β and β' are given for fibers of radii 150 nm, 200 nm, 250 nm and 300 nm. The resulting emission rates into a fiber with $a = 150$ nm for various distances l between the fiber surface and the row of atoms are shown in Fig. 2(a) and distinct maxima are clearly visible whenever the fiber is aligned with an occupied trapping position of the lattice (indicated by the vertical red lines and schematic blue atoms).



(a) Varying the atom-fiber distance

(b) Varying the fiber radius

Fig. 2: (a) Emission rate into the HE_{11} mode of a fiber with fixed fiber radius $a = 150$ nm at a distance, l, of 200 nm (solid line), 250 nm (dashed line) and 300 nm (starred line) from the row of atoms. (b) Emission rate into the same mode, but for fibers with different radii at fixed atom-fiber distance $l = 200$ nm. The fiber radius is 150 nm (solid line), 200 nm (dashed line), 250 nm (starred line) and 300 nm (circled line).

#225079 - $15.00 USD Received 16 Oct 2014; revised 4 Dec 2014; accepted 7 Dec 2014; published 24 Dec 2014
(C) 2014 OSA

As expected, the visibility can be seen to decrease with increasing distance of the fiber from the row of atoms, but even for $l = 300$ nm the signal still allows to distinguish individual maxima. Beyond that, when the atoms are a distance away from the fiber surface such that the light from two polarized dipoles overlaps, it becomes very difficult to resolve the atoms. The positions where no maximum is visible have been intentionally left empty, and the effective extinction of the signal shows that this setup is able to resolve defects in the atomic crystal. As the absence effectively measures a signal homogeneous in space, no degrading of the signal is visible for the parameters shown in the plot.

The dependence of the emission rate into the fiber on the radius of the fiber is shown in Fig. 2(b). Note that we keep the distance between the atom row and the fiber surface constant (l), which means that as the fiber radius increases, the critical distance from the fiber axis to the atom ($l + a$) increases, and the rate of emission into the guided modes can be expected to reduce. This is clearly visible in Fig. 2(b) and the results show that even rather big single-mode nanofibers can record very distinct signals if they are close enough to the atoms.

Table 2: Numerical values of β and β' for a fiber of radius $a = 400$ nm fiber for the first four guided modes, again at the $\lambda_0 = 852$ nm transition in ^{133}Cs.

Mode	β	β '
HE11	9.559×10^6	1.564
TE01	8.197×10^6	1.616
TM01	7.893×10^6	1.464
HE21	7.737×10^6	1.599

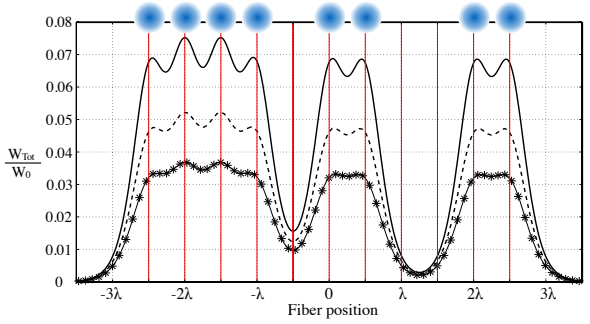


Fig. 3: Combined emission rates into the four available modes in a fiber of radius 400 nm at a distance of 200 nm (solid), 250 nm (dashed) and 300 nm (starred). The overall rates of emission are higher than for a single-mode fiber, however, the visibility decreases faster with increasing distance between the atoms and the fiber.

In slightly larger fibers the presence of three extra modes allows for even higher collection rates and in Fig. 3 we show the emission rates into a fiber of radius $a = 400$ nm. The relevant values for β and β' are given in Table 2. For $\lambda_0 = 852$ nm this fiber can support four guided modes and comparing the rates obtained for $l = 200$ nm with the ones for the single-mode fiber (solid line in Figs. 2(a) and 2(b)), one can see that the collection rate increases from about 0.06 to 0.07. This increase persists at the larger distance of $l = 250$ nm (dashed lines), however less dramatically and by $l = 300$ nm (starred line) it is almost impossible to distinguish the atoms. While using a larger fiber gives an advantage in terms of radiation collected, Fig. 3 also shows

#225079 - $15.00 USD Received 16 Oct 2014; revised 4 Dec 2014; accepted 7 Dec 2014; published 24 Dec 2014
(C) 2014 OSA

that the visibility goes down faster and therefore the resolution for single lattice sites decreases.

From the above it is clear that close proximity between the fiber and the atoms (< 300 nm) is advantageous to obtain clearly distinguishable signals. However, bringing a room-temperature fiber close to a trapped ultracold atom requires the consideration of the van der Waals interaction between the atom and the fiber surface. This is an attractive interaction that can influence the position of the trapping minimum and therefore the distance between the atom and the fiber. While this can lead to a different effective emission rate into the fiber, the more dramatic effect is that the atom can be lost when the attractive potential destabilises the trapping minimum. The classical van der Waals potential felt by an atom near the surface of a dielectric fiber of infinite length was calculated by Boustimi *et al.* [25], and a detailed analysis of their expression by Le Kien *et al.* [26] showed that for atoms close to the surface the van der Waals potential tends to the same values as that for a flat surface

$$V_{\text{flat}} = -\frac{1}{(r-a)^3}\frac{\hbar}{16\pi^2\varepsilon_0}\int_0^\infty d\xi\ \alpha(i\xi) = -\frac{C_3}{(r-a)^3}\,. \tag{9}$$

For atoms further away, the expression for a flat surface offers an upper limit on the influence of the van der Waals interaction and taking $\lambda_0 = 852$ nm gives a van der Waals constant for ^{133}CS of $C_3 \approx 5.6\times10^{-49}$ J m^3 [26]. The combined potentials the atoms sees at two different distances from the fiber ($l = 250$ nm and $l = 300$ nm) are shown in Figs. 4(a) and 4(b), where we have assumed that the atom is transversally trapped in a tight harmonic oscillator trap of frequency 500 kHz. One can see that at these distances the van der Waals interaction does not significantly effect the trapping position and no corrections to the emission rates are necessary. This, however, changes when the atom comes closer to the surface, for distances around 200 nm the trapping potential becomes unstable and the atom is lost to the strong attractive potential from the fiber (see Fig. 4(c)). To avoid this and to stabilise the trapping potential, one can add a field to the fiber, which is blue-detuned for the atom and therefore provides a repulsive, evanescent field that can partly compensate the van der Waals potential.

For this we consider a field of frequency ω_b, chosen such that the single mode condition is fulfilled and that the field is in the fundamental mode HE_{11}. To achieve an angular symmetry in the repulsive intensity distribution we choose circular polarization so that the time-averaged intensity outside the fibre is given by [23]

$$|E|^2 = 2A^2\left[(1-s)^2K_0^2(qr) + (1+s)^2K_2^2(qr) + \frac{2q^2}{\beta^2}K_1^2(qr)\right]. \tag{10}$$

Here the K_n are modified Bessel functions of the second kind, the parameters q and β are as described in Section 3 and A is given in the Appendix. The combined optical and van der Waals potential seen by a ground state atom is then given by [23]

$$U = -\frac{1}{4}\alpha|E|^2 - \frac{C_3}{(r-a)^3}. \tag{11}$$

where $\alpha = \alpha(\omega_b)$ is the real part of the atomic polarizability at the optical frequency ω_b.

The effect of the blue-detuned potential can be seen in Fig. 4(d), where a field of wavelength $\lambda_b = 440$ nm and power $P_b = 1.75$ mW is added to the fibre and allows the original trapping location to be restored. However, it is worth noting that this compensation mechanism does not work for arbitrarily short distances, due to the different functional forms of the van der Waals and the optical potential.

#225079 - $15.00 USD Received 16 Oct 2014; revised 4 Dec 2014; accepted 7 Dec 2014; published 24 Dec 2014
(C) 2014 OSA

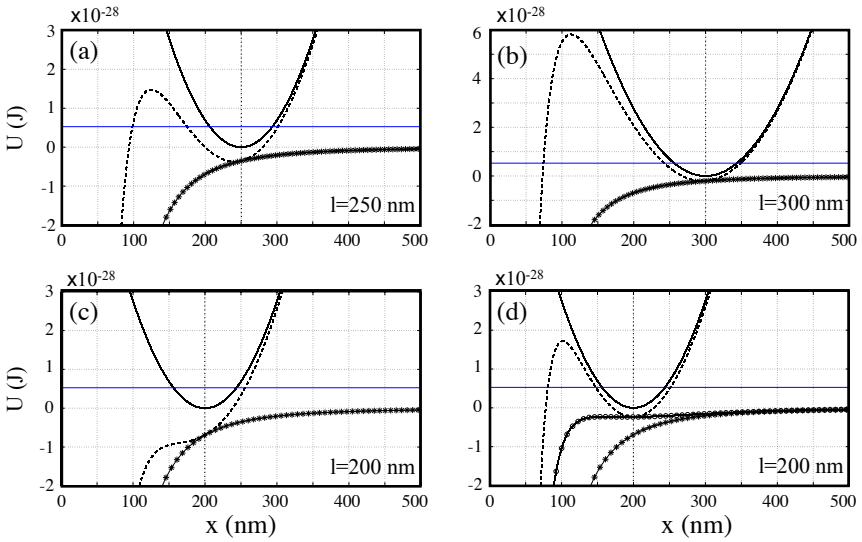


Fig. 4: Potentials along the shortest distance between the fiber surface and the atom. The solid line represents the undisturbed harmonic oscillator potential assumed to have a frequency of ω=500 kHz and the starred line is the van der Waals potential give in Eq. (9). The dashed line is the combined potential of all individual ones. (a) and (b) show that for $l \geq 250$ nm the trapping site is stable, whereas it can be seen in (c) that for $l = 200$ nm the minimum of the joint potential is lost. In (d) a blue-detuned field has been added to the fiber to compensate the attractive van der Waals force. The circled line shows the combined van der Waals and blue-detuned potential, as given in Eq. (11). One can see that this allows for the restoration of the trapping site.

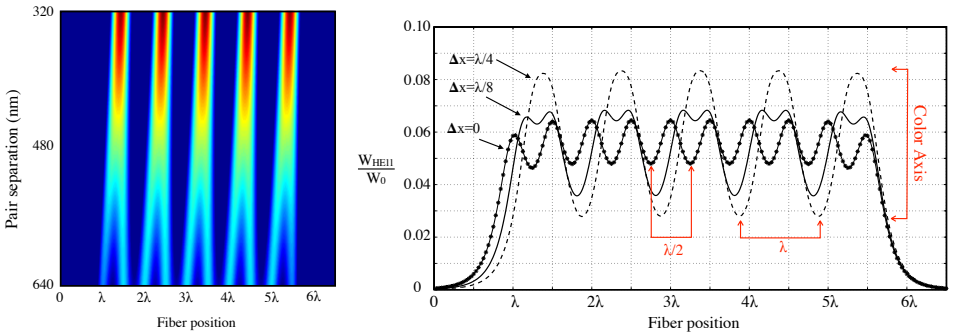
5. Limits

To demonstrate the limits of the technique proposed above and to apply it to a relevant dynamical situation, we return to considering a single-mode fiber of radius 150 nm in this section. From the results shown in Fig. 2(a) we have seen that a nanofiber with a radius smaller than half an optical wavelength can resolve the position space of a collection of atoms trapped in an optical lattice. It is therefore a natural question to ask what the limit of this approach is and if it can be used to resolve more complicated atomic distributions or dynamical processes.

With this in mind, we show in Figs. 5(a) and 5(b) the results for a situation typical in the process of controlled collisions between neutral atoms [27], in which every second atom in a row is brought closer to its neighbor. We consider a row of ten atoms initially equally spaced and calculate the spatially resolved emission rate as the distance between pairs becomes smaller using a fiber of radius $a = 150$ nm, which is $l = 200$ nm away from the row of atoms. One can clearly see that initially the expected well-resolved maxima appear, but with decreasing separation between each pair of atoms the respective maxima move closer together and eventually the pairs of atoms become indistinguishable from each other.

A simple geometrical consideration shows that this should happen when the fibre is so far away from the atoms that it is sitting in the region of overlap of the emission cones from two neighboring dipoles. For the example given in Fig. 5 this corresponds to a distance of around 500 nm. However, as the intensity measured in the fiber increases, one can still infer the presence of two atoms.

#225079 - $15.00 USD Received 16 Oct 2014; revised 4 Dec 2014; accepted 7 Dec 2014; published 24 Dec 2014
(C) 2014 OSA



(a) (b)

Fig. 5: (a) At the bottom of this figure, 10 atoms are arranged in a row, equidistant from one another with a spacing of $\lambda/2 = 640$ nm. Moving towards the top, every other atom shifts closer to its neighbor on the right. The emission from two different atoms can be distinguished until their separation is closer than approximately 500 nm. (b) Here we show three slices from Fig. 5(a) when the pair separation is equal to 640 nm (starred line), 480 nm (solid line) and 320 nm (dashed line). We also indicate the colorbar axis in Fig. 5(a), which ranges from dark blue when low to bright red when high.

Let us finally remark that even though our calculations have been done for a one-dimensional setting, one can easily imagine using a fiber to measure states at the edge of a two-dimensional geometry. Moving the nanofiber through a two-dimensional lattice, however, would lead to losses due to the finite reach of the van der Waals potential and in [28] it was shown that compensation via a blue-detuned field can compensate well enough to allow the fiber to be moved through a lattice while compromising only the very closest sites to itself. This still allows, for example, for measurements to be made on alternate rows. While the analysis of the emission spectrum would be more difficult as emitters are located in two-dimensional space, one can compare measurements from different positions in order to determine the occupation of single lattice sites or even employ fiber arrays [29].

6. Conclusions

We have shown that subwavelength optical nanofibers can be used to resolve atomic distributions in optical lattices. This is an alternative approach to the recently developed atom microscope and allows for higher resolution when using smaller fibers. However, as it requires bringing macroscopic objects very close to single atoms, it is mainly limited to one-dimensional arrays or edges of higher dimensional ones. Nevertheless, it offers a new approach that can be integrated in ultracold atom experiments with current technologies.

Appendix

The explicit forms for the emission rates into the individual modes of the fiber given in Sec. 3 contain the following expressions for completion

#225079 - $15.00 USD Received 16 Oct 2014; revised 4 Dec 2014; accepted 7 Dec 2014; published 24 Dec 2014
(C) 2014 OSA

HE_{11} MODE

$$N_1 = J_1^2(ha) - J_0(ha)J_2(ha) + \frac{\beta^2}{2h^2}\Big[(1-s)^2\left(J_0^2(ha)+J_1^2(ha)\right) + (1+s)^2\left(J_2^2(ha)+J_1(ha)J_3(ha)\right)\Big] \tag{12}$$

$$N_2 = \frac{J_1^2(ha)}{K_1^2(qa)}\left[K_0(qa)K_2(qa) - K_1^2(qa) + \frac{\beta^2}{2q^2}\Big[(1-s)^2\left(K_1^2(qa)+K_0^2(qa)\right) + (1+s)^2\left(K_1(qa)K_3(qa)-K_2^2(qa)\right)\Big]\right] \tag{13}$$

$$s = \frac{1/h^2a^2 + 1/q^2a^2}{J_1'(ha)/haJ_1(ha) + K_1'(qa)/qaK_1(qa)} \tag{14}$$

TE_{01} MODE

$$P_1 = \frac{1}{a^2h^2}\frac{K_0^2(qa)}{J_0^2(ha)}\left(J_1^2(ha) - J_0(ha)J_2(ha)\right) \tag{15}$$

$$P_2 = \frac{1}{a^2q^2}\left(K_0(qa)K_2(qa) - K_1^2(qa)\right) \tag{16}$$

TM_{01} MODE

$$Q_1 = \frac{K_0^2(qa)}{J_0^2(ha)}\left[J_0^2(ha) + \frac{n_1^2k^2}{h^2}J_1^2(ha) - \frac{\beta^2}{h^2}J_0(ha)J_2(ha)\right] \tag{17}$$

$$Q_2 = \frac{\beta^2}{q^2}K_0(qa)K_2(qa) - K_0^2(qa) - \frac{n_2^2k^2}{q^2}K_1^2(qa) \tag{18}$$

HE_{21} MODE

$$R_1 = J_2^2(ha) - J_1(ha)J_3(ha) + \frac{\beta^2}{2h^2}\Big[(1-u)^2(J_1^2(ha) - J_0(ha)J_2(ha)) + (1+u)^2(J_3^2(ha) - J_2(ha)J_4(ha))\Big] \tag{19}$$

$$R_2 = \frac{J_2^2(ha)}{K_2^2(qa)}\left[K_1(qa)K_3(qa) - K_2^2(qa) + \frac{\beta^2}{2q^2}\Big[(1-u)^2(K_0(qa)K_2(qa) - K_1^2(qa)) + (1+u)^2(K_2(qa)K_4(qa) - K_3^2(qa))\Big]\right] \tag{20}$$

$$u = \frac{2\left(1/h^2a^2 + 1/q^2a^2\right)}{J_2'(ha)/haJ_2(ha) + K_2'(qa)/qaK_2(qa)} \tag{21}$$

$$A = \frac{\beta}{2q}\frac{J_1(ha)/K_1(qa)}{\sqrt{\pi a^2(n_1{}^2N_1 + n_2{}^2N_2)}} \tag{22}$$

Acknowledgments

We would like to thank C.F. Phelan for valuable discussions. This work is dedicated to the memory of Prof. V. Minogin.

#225079 - $15.00 USD Received 16 Oct 2014; revised 4 Dec 2014; accepted 7 Dec 2014; published 24 Dec 2014
(C) 2014 OSA

5.3 Conclusions and Future Work

Since the publication of this paper there has been further interest in the interaction of cold atoms with nanofiber higher modes. Recently, in [82], a fiber carrying the first four guided modes was integrated into a gas of ^{87}Rb atoms and the number of fluorescence photons detected was larger by a factor of about six compared to a single mode fiber. This is in agreement with the increase predicted by [81] and provides promising support for the realization of trapping and detection schemes using higher order mdoes.

This presented scheme could be used to detect atomic population non-destructively in lattice sites close to the edge. Such atoms can have specific importance, due to the existence of edge states in topological insulators, and therefore this method might be highly suitable to the exploration of topologically non-trivial phases. Furthermore, non-destructive single site resolution allows for the detection of imperfections in Mott Insulator states or single atoms in optical traps with high accuracy.

However, the impressive advances in the area of quantum gas microscopes raises the question of whether nanofibers have any advantage over such systems in specific scenarios? One aspect would be that nanofibers are only limited by the fiber diameter, rather than the diffraction limit of a highly non-linear lens. It is relatively cheap to build a fiber system, and (currently) requires less resources when compared to atom microscopes.

The prospect of transferring light from one place, or from one specific atom, to another along the path of a nanofiber is also exciting. It is possible to conceive of experiments where the mode selectivity of fibers is an advantage. Since fibers can be bent, one can in principle envision a situation where an atom is located at the centre of a loop, which would allow a detector covering 2π. Arranging nanofibers in arrays could allow for simultaneous measurements, which is not easily done using a microscope. Showing that single atom resolution is possible is only the first step.

Chapter 6

Confined Light in the Scattered Field of Bosons in a Nanofiber Guided Mode

6.1 Abstract

For several decades laser light has been used in many interesting ways to tailor trapping geometries and to manipulate atomic interactions. In most cold atom experiments, the optical potential is provided by external lasers and considered to be static. Light scattering and long-range interactions due to backaction are generally neglected. Only recently, first experiments using the Dicke phase transition for atoms trapped in optical cavities have enabled the creation of potentials that are inherently dependent on the atomic density itself [83]. In the scheme presented here, we consider the light scattered into an optical nanofiber by atoms trapped in a one-dimensional harmonic trap parallel to the axis of the nanofiber. Our approach is semiclassical, and we show how the shape of the scattered electromagnetic field is influenced by the exact density distribution of the trapped atoms. The possibility for backaction on the atomic wavefunction due to the population of the fiber mode is also examined but determined to be negligible, at least for

experimentally realistic parameter regimes. I show that, for particular values of atomic interaction and trapping frequency, the scattered field is completely localized over a range that corresponds to the length on which the atoms are trapped. This is first shown for a pair of interacting atoms, then we give some preliminary results for three interacting atoms, and finally for systems with more particles in the Tonks Girardeau regime.

6.2 Introduction

In recent years, the field of research concerning the use of nanofibers in cold atom experiments has been developing quickly. Notable milestones and key ideas include the proposal and realization of a scheme to trap atoms in a two-color evanescent field around a single mode nanofiber [16, 17] (further discussed in Chapter 3), the possibility for the coupling of atoms to a nanophotonic waveguide in order to self-organize without external trapping potentials or cavity mirrors [85] and the prediction that dipole-dipole interactions via the fiber mode can induce a stable regular order and nontrivial long-range correlations [84].

At the same time, the development of techniques to control and manipulate the interparticle scattering properties of ultracold atoms has given access to gases in the ideal as well as in the strongly correlated regime. These techniques are typically based on Feshbach or confinement-induced resonances, which has permitted, in particular, the experimental realization of strongly interacting bosonic gases in the Tonks-Girardeau (TG) regime [86, 87]. In this limit a quasi-one-dimensional quantum gas of strongly-interacting bosons famously acquires fermionic properties [21, 22].

In the following I will describe a system, where transversally incident laser light is scattered into an optical nanofiber by a small number of atoms trapped next to the fiber. In particular I will be interested in different effects stemming from control over the scattering properties of the atoms, which I describe fully quantum mechanically. Our approach is similar to the one taken by Grießer and Ritsch

in [88], who described a Maxwell–Boltzmann gas interacting with a laser in the vicinity of an optical nanofiber. A scattering matrix approach to this system has also been explored [89]. The atoms scatter light into the fiber, which in turn backacts onto the atoms. Following the Dicke approach, one would expect that above a certain laser intensity threshold, the system will undergo a phase transition into one of multiple self-sustained ordered states. While the dependence of this state on the correlation strengths within the atomic samples is clearly an interesting question, I show in the following that any backaction of the light on the atoms for the small samples we are dealing with is negligible. However, the correlations within the atomic samples have a significant influence on the scattered field, as the source term in the Helmholtz equation depends on the density distribution of the atoms.

This chapter represents a work in progress. However, as we have already obtained significant results, these are presented in the following. I begin with the derivation of the relevant Helmholtz equation in Sec. 6.3 and the situation for two and three interacting bosons is described in Sec. 6.4. A Tonks-Girardeau gas is considered in Sec. 6.5, and Sec. 6.6 lays out the possibilities for future work and concludes.

6.3 Helmholtz Equation in One-Dimension

We consider the atoms to be trapped in an effectively one-dimensional potential parallel to the nanofiber and along the z-axis given by

$$U_H = \frac{1}{2} m\omega^2 z^2. \tag{6.1}$$

The trap is located within range of the evanescent decay length of the fundamental HE_{11} mode of a nanofiber, for light at the dominant wavelength of the trapped atom. This ensures that a significant amount of light will be scattered into the fiber. An incident laser beam is oriented at a right angle to the nanofiber axis, so that the atom trap is illuminated transversely. Below we follow Griesser and Ritsch [88] in order to derive the parameters and form for a Helmholtz equation

that describes the field scattered into the fiber. A schematic of the setup can be seen in Fig. 6.1.

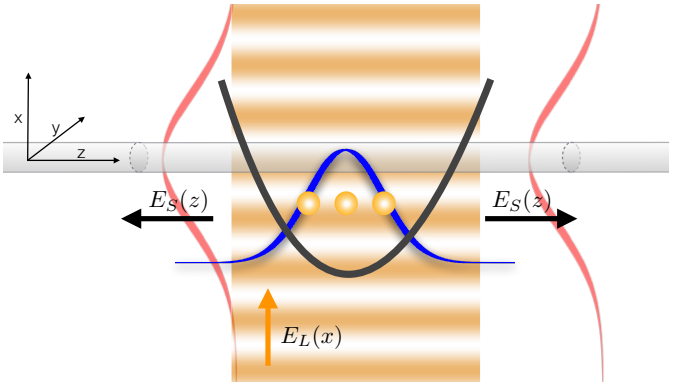


FIGURE 6.1: Schematic of atoms in an elongated trap along the z-axis of a nanofiber and inside the range of the fundamental mode. All other spatial degrees of freedom are assumed to be frozen out by strong transversal confinement.

The incident laser field in three dimensions $\mathbf{E_L}(\mathbf{x}, t)$, with frequency ω_L, can be written in its the usual form

$$\mathbf{E_L}(\mathbf{x}, t) = \hat{\mathbf{e}}_L E_L(\mathbf{x}) \exp(-i\omega_L t) + c.c. \tag{6.2}$$

When this incident beam scatters from the trapped atoms, it gives rise to a new field, $\mathbf{E_S}$, which we can write in the form

$$\mathbf{E_S}(\mathbf{x}, t) = \hat{\mathbf{e}}_L E_S(\mathbf{x}) \exp(-i\omega_L t) + c.c. \ ,$$

where polarization effects and retardation have been neglected. Its envelope, E_S, satisfies the standard Helmholtz equation

$$\nabla^2 E_S + \left(k_L^2 n_f(x) + k_L^2 \chi\right) E_S = -k_L^2 \chi E_L \ , \tag{6.3}$$

where k_L is the wavevector of the incident laser beam and $n_f(x)$ is the refractive index profile of the nanofiber and

$$\chi(x, y, z) = \frac{\alpha}{\epsilon_0} \rho(x, y, z), \tag{6.4}$$

is the susceptibility of the particles in three dimensions. In eq. (6.4) α is the atomic polarizability, as discussed in Chapter 2, ρ is the atomic density and ϵ_0 is the permittivity of free space. For the trapping scenario outlined above, we need to make some adjustments to this three dimensional model.

As we assume the radial confinement to be much stronger than the axial, we can factorize the atomic density as $\rho(\mathbf{x}, t) = \rho(z, t)\rho_\perp(x_\perp)$. A similar ansatz can be made for the fiber mode, requiring that the radial mode function of the fiber is only weakly perturbed by the presence of the atoms

$$E_S(x, y, z, t) = \sqrt{A} E_S(z, t) u(x_\perp) \ , \tag{6.5}$$

where A is the cross-section accounting for the radial overlap of the normalized HE_{11} mode function with the density distribution ρ [88],

$$A = \frac{1}{\int u^2 \rho_\perp d^2 x_\perp} \ . \tag{6.6}$$

Using the separation of variable ansatz made in eqs. (6.5) and (6.6), the Helmholtz equation can be integrated over the transverse degrees of freedom to yield an expression which describes the dynamics in the z-direction only:

$$\frac{\partial^2 E_S(z,t)}{\partial z^2} + \left(\beta^2 + k_L^2 \chi(z)\right) E_S = -k_L^2 \chi(z) E_L. \tag{6.7}$$

Here the effective magnitude of the incoming electric field is given by

$$E_L = -\sqrt{A} \int_{-\infty}^{\infty} E_L u \rho_\perp d^2 x_\perp \tag{6.8}$$

and the effective susceptibility is $\chi = \frac{\alpha}{\epsilon_0 A}\rho$. Henceforth, when we refer to χ and E_S, we mean $\chi(z)$ and $E_S(z)$. We assume that the fiber has an infinite length and therefore choose Sommerfeld's radiation boundary conditions in order to avoid reflections [88]

$$\frac{\partial E_S}{\partial z} = \pm i\beta E_S(z,t), \qquad z \to \pm\infty. \tag{6.9}$$

TABLE 6.1: Parameters, values and units

Quantity	Name	Value	Unit
ω	Harmonic oscillator frequency	$2\pi \times 700$	Hz
m	Mass of Cs	$133 \times 1.66 \times 10^{-27}$	kg
λ_L	laser wavelength	800×10^{-9}	m
β	Prop constant	8.0163×10^{6}	m^{-1}
α	Atomic polarizability	-3.9264×10^{-38}	C m^2V^{-1}
ϵ_0	Vacuum permittivity	8.8542×10^{-12}	F/m
A	Cross section	1	m^2
E_L	Laser field strength	150	V m^{-1}
g	Interaction strength	1×10^{-36}	(J s)^2 kg^{-2}

The dipole potential along the z-direction is given by a combination of the scattered field (the solution of the Helmholtz equation) and the incident laser field as $U_S = -\alpha|E_S + E_L|^2$ and the total potential felt by the atoms is given by

$$U_{\text{tot}} = U_H - \alpha|E_S + E_L|^2. \tag{6.10}$$

Noticing that the electric field interference terms are only present across the width of the incident laser beam, it simplifies outside of this area to

$$U_S(|z| \to \infty) = U_H - \alpha|E_S|^2. \tag{6.11}$$

In the following we will be answering the question of whether this optical dipole potential has an effect on the atomic state. To investigate the effect of the potential due to the scattered field, we look at a set of experimentally realistic parameters, which are listed in Table 6.1.

Looking at the left-hand-side of eq. (6.3), one can see that the magnitude of the scattered field is controlled by the magnitude of the terms in $(\beta^2 + k_L^2\chi)\, E_S$, where the propagation constant β is on the same order of magnitude as the wavevector $k_L = 2\pi/\lambda_L$. For the second term, which contains the effects of the atomic density, to be significant χ must be on the order of one or larger. In our case the density is

low, ($\rho \approx 2\,\mu\mathrm{m}^{-1}$), $\epsilon_0 \approx 8.854 \times 10^{-12}$ F/m, and the cross section, A, is roughly of the order of one or smaller. For typical atoms, i.e. Cesium or Rubidium, the atomic polarizability due to the far-detuned incident beam has a magnitude on the order of 10^{-38}C m^{2}V^{-1}, which can increase by a few orders of magnitude if the beam moves closer to resonance, this however results in unwanted radiation pressure which leads to atom loss. This suggests that χ, even for idealized parameters and on-resonance laser light, is 18 orders of magnitude smaller than one.

It is therefore clear that the optical field will not have any backaction on the atoms, unless the intensity of the incoming laser beam in increased unreasonably. In the following we will therefore concentrate on the effect of the inhomogeneous density distribution of the atoms on the optical field. For this we will solve the Helmholtz equation with the appropriate source term fully numerically, as well as using the Greens function methods.

For the latter, we can very simply apply the standard procedure for a Helmholtz equation of the form

$$\frac{\partial^2 E_S}{\partial z^2} + \beta^2 E_S = -k_L^2 \chi E_L, \tag{6.12}$$

for which the solution is given by (see [90])

$$E_S(z) = \frac{k_L^2 E_L \alpha}{4\pi\varepsilon_0 A} \int_{-\infty}^{-\infty} \rho(z') \frac{e^{-i\beta|z-z'|}}{|z-z'|} dz'. \tag{6.13}$$

6.4 Two and Three Interacting Bosons

The Hamiltonian for two interacting bosons in a harmonic potential can be written as

$$H = \sum_{i=1}^{2} \left[-\frac{\hbar^2}{2m} \frac{\partial^2}{\partial {z_i}^2} + U_{\mathrm{tot}} \right] + g_{1D}\delta(z_1 - z_2). \tag{6.14}$$

The interaction is modeled as point-like and the quantity g_{1D} represents its strength, which we will always assume to be repulsive ($g_{1D} > 0$). It is related to the one-dimensional s-wave scattering length, a_{1D}, through $g_{1D} = -2\hbar^2/ma_{1D}$. In

turn, a_{1D} is related to the actual three-dimensional s-wave scattering length, a_{3D}, through $a_{1D} = -l_\perp^2/2a_{3D}(1 - Ca_{3D}/l_\perp)$, where C is a constant of value $C = 1.4603\ldots$ and $l_\perp$ is the ground state size of the transversal trapping potentials [91].

The density of the two-particle state is given by the diagonal of the reduced single-particle density matrix,

$$\rho = \rho^1(z, z) = \int_{-\infty}^{\infty} \Psi(z, z_2)\Psi^*(z, z_2)dz_2 \,, \tag{6.15}$$

where $\Psi(z_1, z_2)$ is the two-body wave function and z_1 and z_2 are the respective positions of atoms. The wave function satisfies the Schrödinger equation $\epsilon\Psi = H\Psi$.

As g_{1D} increases, the density distribution gets broader and we will show in the following that, for a two atom boson-boson interaction, a singular value of the repulsive interaction strength g_{1D} exists that results in complete destructive interference of the scattered field at large values of $|z|$. In fact, at this value the scattered light is localized across the region where the atoms are trapped. Later we will see that for three interacting atoms two of these critical points exist and that for a Tonks gas with N bosons $N-1$ can be found. The points of localization of light are a direct consequence of the inhomogeneity of the source term.

For the classical Helmholtz equation the main effect of an increased scattering among the atoms is a broader density distribution in the source term. However, this can also be achieved with a change in the trapping frequency, and we therefore show in Fig. 6.2 a diagram where the points that lead to light localization can be found along a black line as a function of g_{1D} and trap ground state width $l = \sqrt{\frac{\hbar}{m\omega}}$. For a given value of l we will call the corresponding value of the interaction strength g_c. One can see from Fig. 6.2 that a minimum value for l exists, below which no localization can be found. This is the regime, where the trap is very tight and the density never becomes broad enough to allow for the destructive interference effect to happen. Note that the width of the density for the two atom case is limited by the width of the first eigenstate of the harmonic oscillator [92].

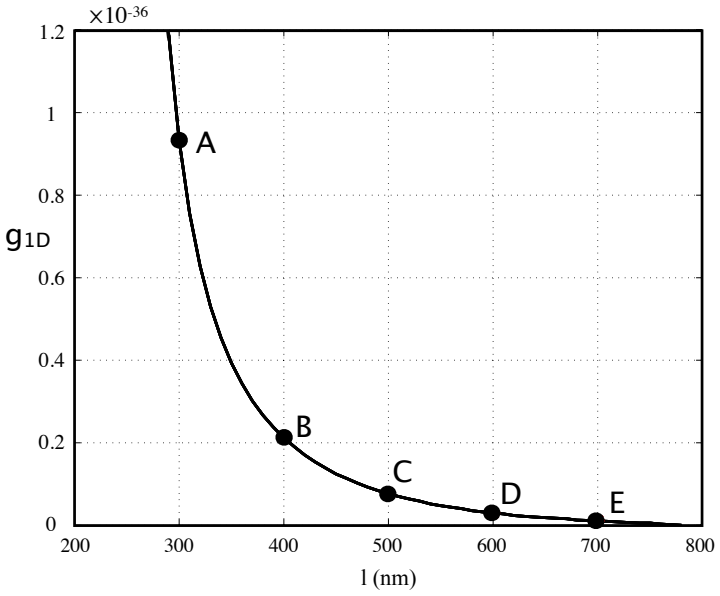


FIGURE 6.2: For a pair of trapped bosons, the black line indicates the critical value for the interaction strength, g_c, at which localization of the scattered field occurs for a given trap width.

To see what happens at the critical value, we show in the middle column of Fig. 6.3 the real part of the electric field for the points marked in red and labeled A-E in Fig. 6.2. For the remainder of this chapter, where we plot the real part of the electric field, we always confirm that the real and imaginary parts undergo their π phase shift at the same critical point. To compare, the column on the left shows the same in the absence of interaction ($g = 0$) and the column on the right assumes g_{1D} to be twice the critical value ($g_{1D} = 2g_c$). For small values of l one can see that the field localizes at the critical interaction strength, whereas for the other two interaction strengths a wave solution can be found at large $|z|$. This is more clearly visible where the chosen interaction strengths are quite different in magnitude (points A,B and C), but can be seen with smaller amplitude also for the points D and E.

To show what happens at the localization point we show in Fig. 6.4 the real part of the electric field for $l = 400$ nm on the left, and for $l = 600$ nm on the right, for continuously changing g_{1D}. The dashed horizontal lines correspond to the values of g_{1D} used in Fig. 6.3, the color scale varies from blue, indicating the lowest value of the real part of the electric field, to red, where the real part of the field takes its

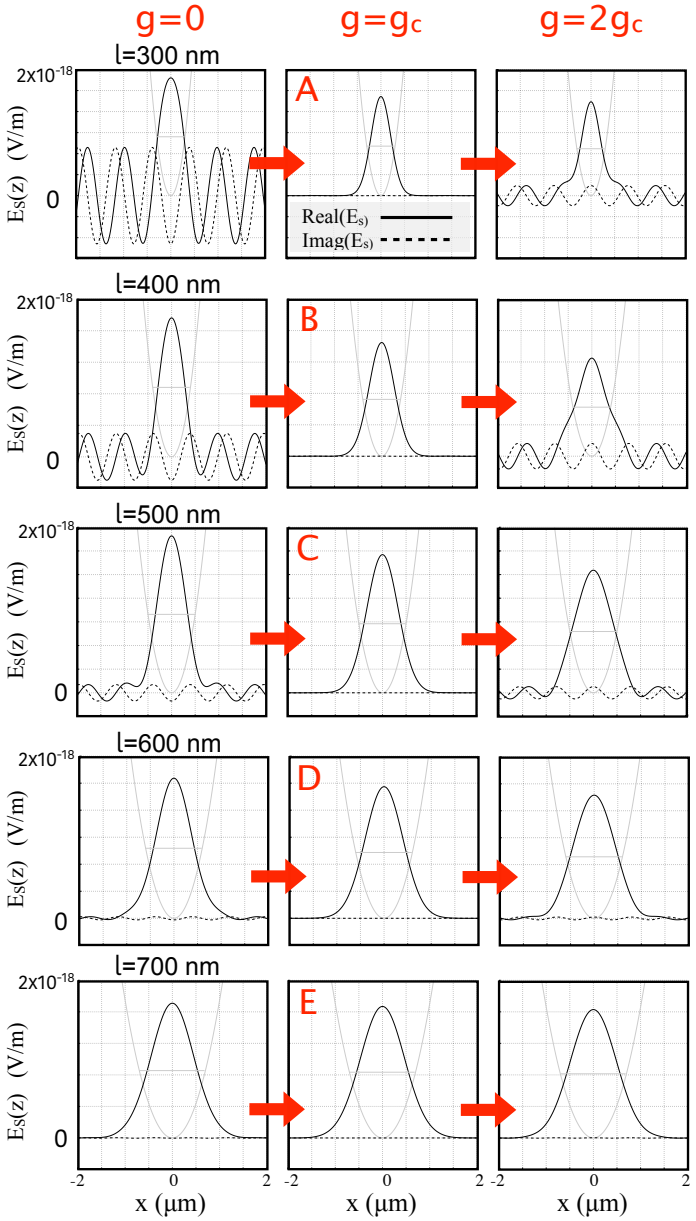


FIGURE 6.3: For the trapping width corresponding to the points labeled A-E in Fig. 6.2, here we show the real (solid line) and the imaginary (dotted line) parts of the scattered electric field E_S at $g = 0$ in the left column, $g = g_c$ in the center column and $g = 2g_c$ in the third column.

highest value. One can clearly see that through the critical point the asymptotic field undergoes a π phase flip, which indicates that the localization is an effect of destructive interference from waves scattered by different parts of the density distribution. For $l = 600$ nm, shown in the right panel in Fig. 6.4, the localization and phase flipping happen at a small value of g_{1D} and one can see that this is the

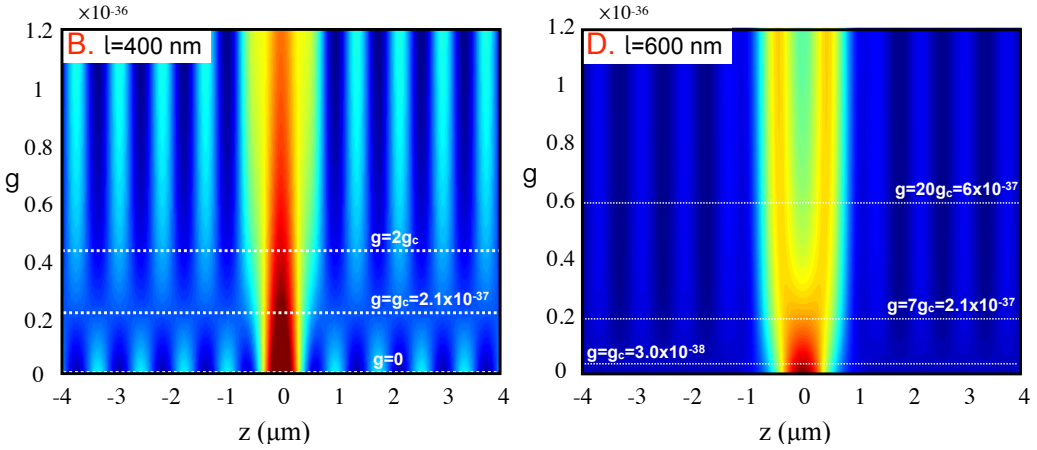


FIGURE 6.4: Real parts of the electric fields for a situation where the width of the harmonic oscillator ground state is $l = 400$ nm (left panel) and $l = 600$ nm (right panel). These again correspond to examples B and D, from Fig. 6.2.

only localization point in this system.

In Fig. 6.5, a more detailed version of the second row in Fig. 6.3 is shown, with the panel on the left corresponding to the real (black) and imaginary (grey) parts of the electric field for different values of g_{1D}. The solid black line is at $g_{1D} = g_c$. The panel on the right shows the optical potential calculated from $-\alpha|E_S|^2$ and the panel at the bottom is an enlargement of the section of the optical potential indicated with a red frame. As expected, at $g_{1D} = g_c$ the optical potential is zero everywhere outside of the region to which atoms are confined. In Fig. 6.6, a more detailed version of the fourth row in Fig. 6.3 is shown, which confirms the same results.

Three Interacting Bosons

While the numerical solution of the two atom problem is rather straightforward, larger numbers cannot be treated easily. However, despite the dimensionality of the Hilbert space for more particles requiring significantly more computational resources than the two particle case, we are able to present a limited set of results here. The Hamiltonian for the one-dimensional problem of three interacting

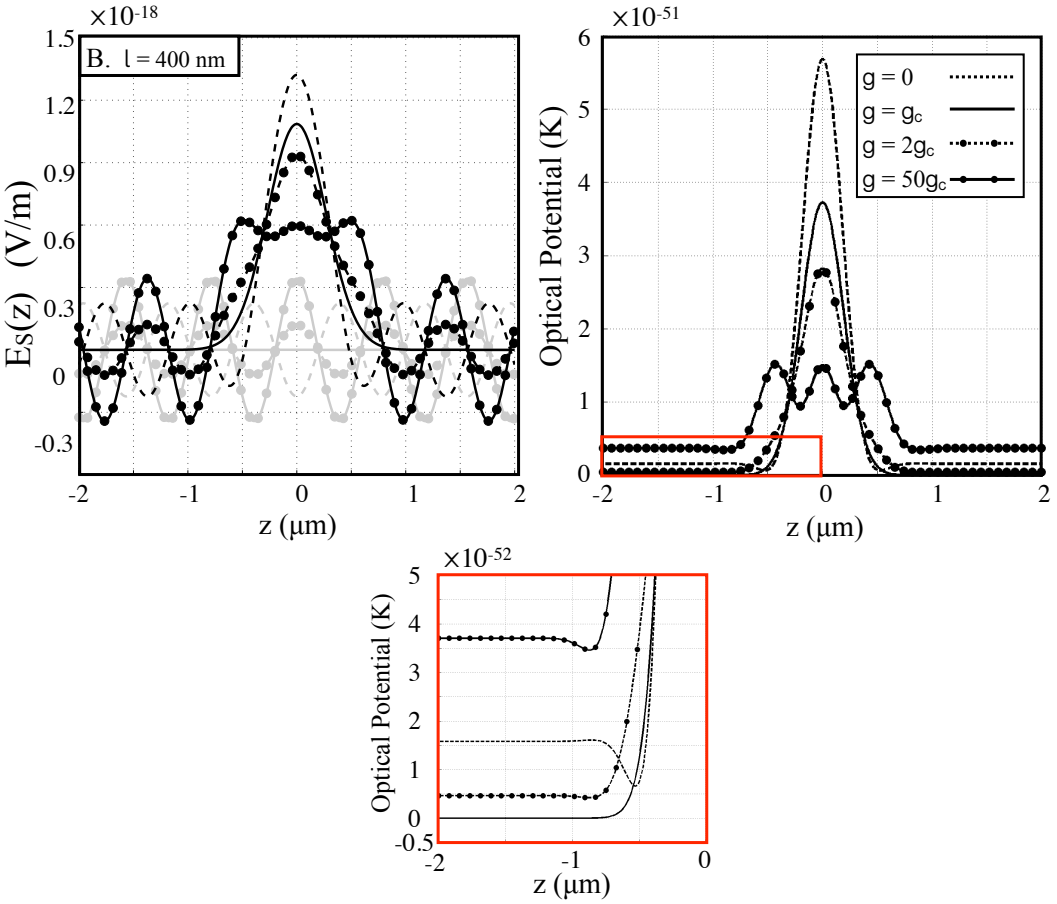


FIGURE 6.5: The panel on the left shows the real and imaginary parts of the scattered electric field and the panel on the right shows the corresponding dipole potential for a variety of g_{1D} values indicated in the right panel. The smaller panel at the bottom is an enlarged section of the panel showing the potential, as indicated by the red frame, to highlight that only the potential for g_c goes to zero for larger values of $|z|$. The data in this figure belongs to the vertical line through point B in Fig. 6.2.

ultracold bosons can be written as

$$H = \sum_{j=1}^{3} \left[-\frac{\hbar^2}{2m} \frac{\partial^2}{\partial {z_j}^2} + U_{\text{tot}} \right] + \sum_{1 \le j < k \le 3} g_{jk} \delta(z_j - z_k) \ , \tag{6.16}$$

and we assume for simplicity that all g_{ij} have the same value (i.e. the gas is made from a single atomic species). The numerical solutions show the existence of a critical interaction strength and in Fig. 6.7 these are given as a function of the width of the underlying trapping potential. Note that two points exist for every trapping width until, similar to the two-particle case, the trap becomes too narrow.

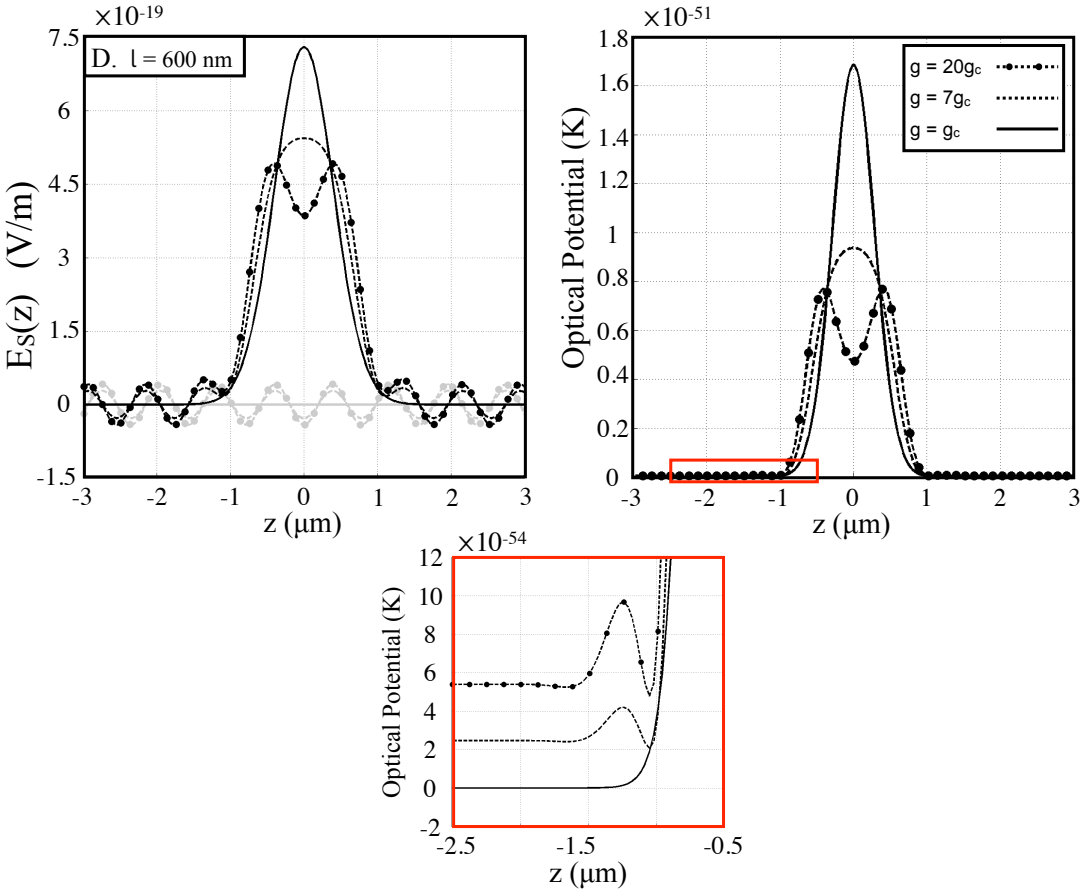


FIGURE 6.6: Same as Fig. 6.5, but for atoms trapped in a harmonic oscillator with a ground state width of $l = 600$nm. This corresponds to the vertical line through point D in Fig. 6.2.

It is also worth pointing out that in Fig. 6.7 the only calculated data points are the ones indicated by bold dots, wheras in the two-particle case the entire curve are calculated values. This is due to the limited access to the large resources necessary to solve the three particle Hamiltonian for more parameters. The indicated curves are extrapolated.

The real part of the electric field over the full range of interaction strength for four different trap widths is shown in Fig. 6.8. One can see that for $l = 200$ nm no critical point exists and that for $l = 300$ nm only one can be found (indicated by the white dashed line). For $l = 400$ nm and $l = 500$ nm two critical points are visible, but none further. As before, at each critical point the field goes through a π phase shift.

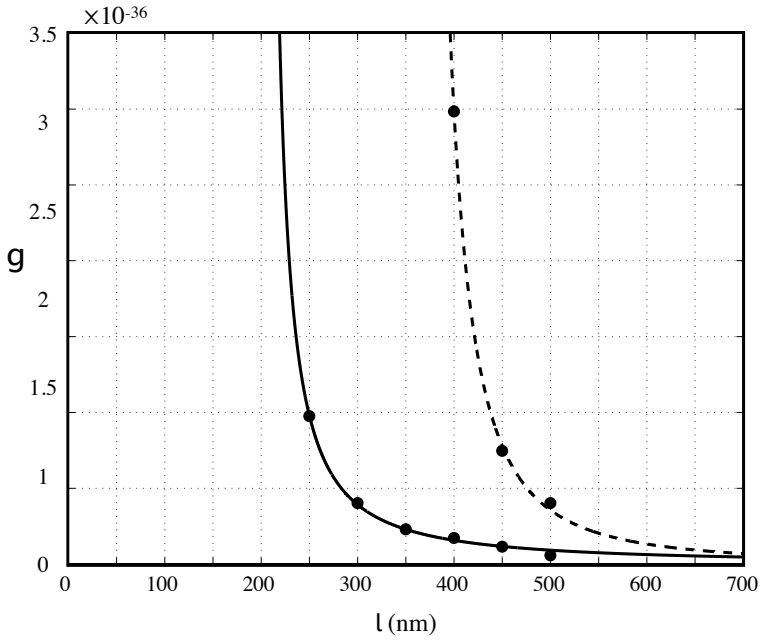


FIGURE 6.7: The line indicates the critical values for the interaction strength, g_c, at which localization of the scattered field occurs for a given trap width. This is for the three particle case.

Solving systems for larger particle numbers and arbitrary interaction is numerically not possible. However in the limit of strong interaction the existence of the so-called Bose-Fermi mapping theorem allows us to map the strongly interacting bosons to non-interacting fermions, and an analytical solution exists again. A gas in this limit is called a Tonks-Girardeau gas.

6.5 Tonks-Girardeau Gas

A Tonks-Girardeau (TG) gas is a one-dimensional, strongly correlated gas consisting of bosons that interact via a hard-core potential [87, 93, 94]. In the limit of point-like interaction, Girardeau found that such a model can be solved exactly by mapping it to an ideal, spinless fermionic system and was the first to point out that a gas of strongly-interacting bosons can acquire certain fermionic properties such as the exclusion of two particles from being at the same point [87]. Tonks gases have proven to be a rich system in which to study new physics, not

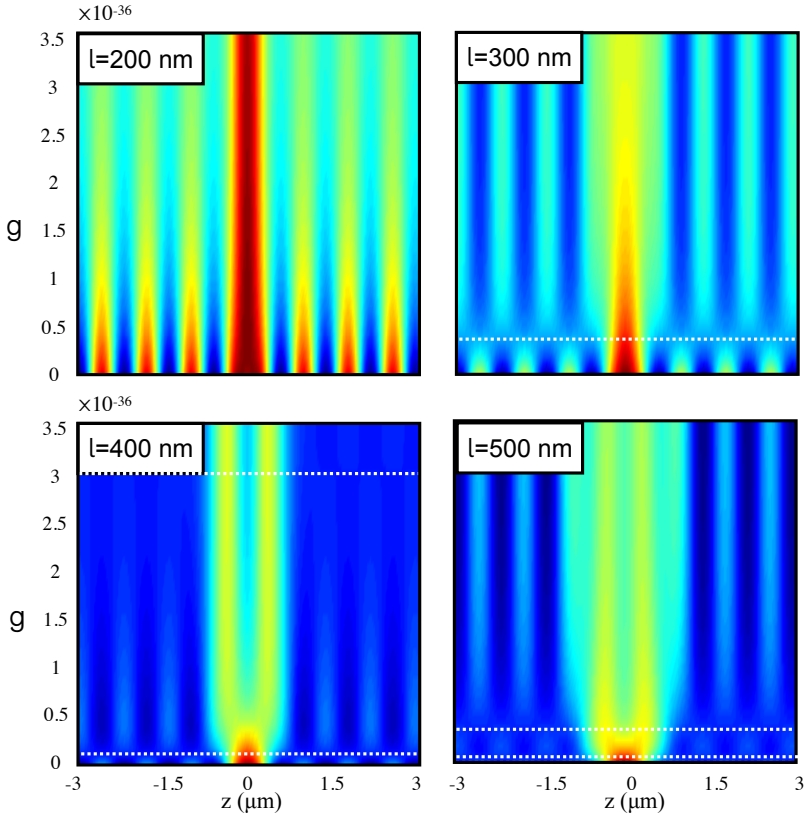


FIGURE 6.8: For three particles, the localization points in the electric field are just about evident where we expect to see them based on Fig. 6.7. The white dashed lines indicate the flipping points described in the text. The color scale again varies from blue, indicating the lowest value of the real part of the scatered electric field, to red, where the real part of the scattered field is at its highest.

least due to their analytic accessibility. Identifying scenarios that take advantage of this is therefore interesting, especially as an exact solution for the harmonic oscillator is known [86, 95]. Here we consider a gas of N bosons trapped in the scenario described in the previous section, where the atoms are tightly confined in the transversal directions and we have control over the trapping frequency in the z-direction. In this way, in the low-temperature limit, we again restrict our model to the longitudinal direction only, as in [91].

The utility of the Fermi-Bose mapping for a TG gas lies in the fact that the density profiles for the Fermi and Bose problems are identical. The ground state density

for a TG gas of N atoms in a harmonic oscillator can be calculated as

$$\rho_N = \sum_{n=0}^{N-1} |\Psi_n|^2 = \sum_{n=0}^{N-1} \left| \frac{\sqrt[4]{\frac{m\omega}{\pi\hbar}} e^{-\frac{mz^2\omega}{2\hbar}} H_n\left(z\sqrt{\frac{m\omega}{\hbar}}\right)}{\sqrt{2^n n!}} \right|^2 . \tag{6.17}$$

As the interaction is fixed, the only way to change the size of the density distribution is to vary the width of the harmonic oscillator potential. Here we use the average spacing, l_{sep}, of the N atoms in a Tonks gas in a harmonic oscillator as our variable

$$l_{\text{sep}} = \frac{2\sqrt{2N-1}}{N-1}\sqrt{\frac{\hbar}{m\omega}} , \tag{6.18}$$

as we can vary it in a linear fashion and it therefore aids intuitive understanding. For all examples in this section, the mass of the atoms was chosen to correspond the Cesium, i.e. $m = 133$ a.m.u.. The corresponding trapping frequencies are then given by

$$\omega = \frac{8N-4}{(N-1)^2}\frac{\hbar}{m l_{\text{sep}}^2}. \tag{6.19}$$

Similar to the two and three atom cases discussed above, we find that certain values of the average spacing exist for which the scattered electric field is zero outside the region where the atoms are trapped. In fact, for a TG gas of N atoms we find that $N-1$ of these points exist.

In order to connect the results of the TG limit to the ones for the cases discussed above, we show in Fig. 6.9 the asymptotic value of the optical potential as a function of l_{sep} for a three particle Tonks gas. One can clearly see that two values exist for which the potential goes to zero. However, one can also notice that the field goes to zero for larger interparticle distances corresponding to lower densities.

In Fig. 6.10 we show the full fields (left panel) and potential (right panel) for the three particle Tonks case for three different values of l_{sep}. The critical value of l_{sep},

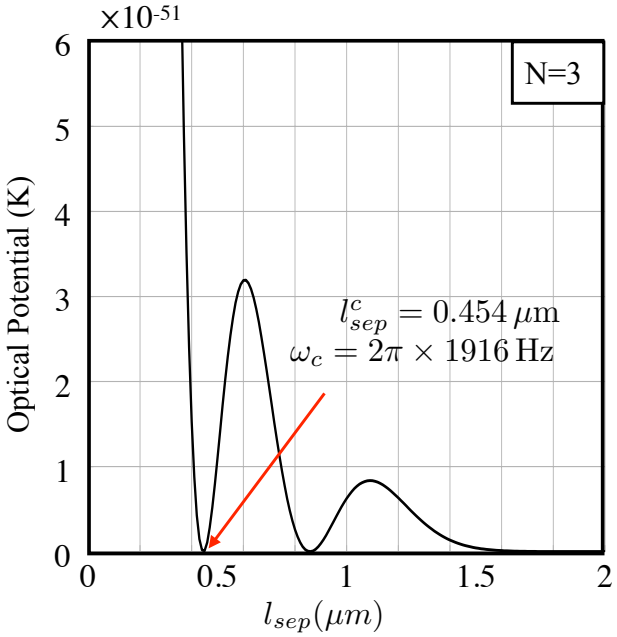


FIGURE 6.9: Optical potential strength in the asymptotic region well outside the trapping width against the average spacing between the atoms for the three-particle Tonks gas. The two points, where the light localises, are clearly visible. The critical value of l_{sep} has been denoted l^c_{sep}.

where the localization occurs, is labeled l^c_{sep}. Again, the localization of the field for l_c is clearly visible.

To see the effect of larger particle numbers, we show in Fig. 6.11 the real part of the scattered field plotted against the ground state size of the harmonic oscillator for easier comparison between the systems of different particle number. One can clearly see that each plot has $N-1$ points at which the field localises and the phase jumps by π.

6.6 Conclusions and Future work

While the results presented in this chapter are undoubtedly interesting, their full understanding requires additional work. Furthermore, the obtained field strengths are very small and to observe this effect one would need to consider strategies that allow more light to scatter into the fiber. This could, for example, be the

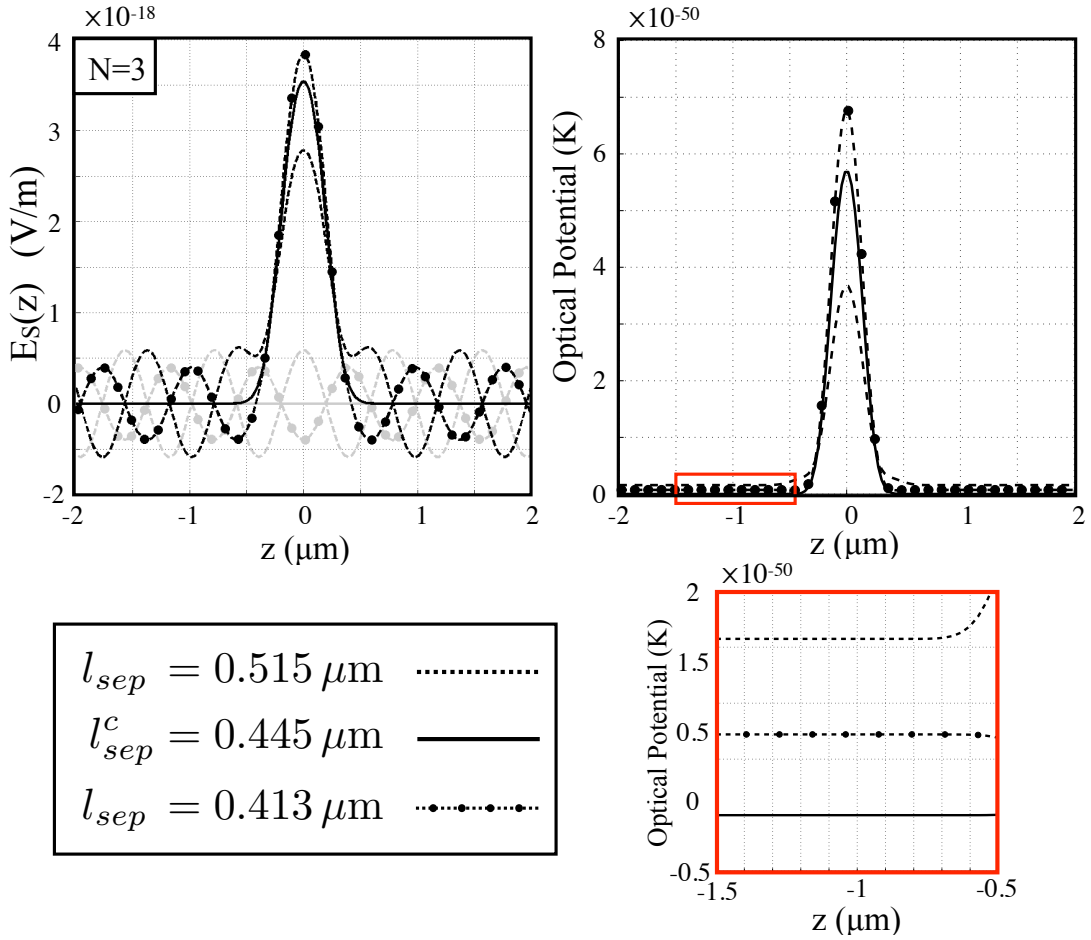


FIGURE 6.10: The real and imaginary parts of E_S (left panel) and the optical potential U_{scat} (right panel) for a Tonks gas of 3 atoms.

inclusion of a Bragg cavity into the fiber, or bringing the scattered light close to the resonance. The latter would, however, also lead to more heating and one would have to consider saturation of the atoms. Furthermore, larger amounts of light inside the fiber will also, at some point, lead to backaction on the atomic density and therefore to a modification of the source term in eq. (6.7).

While at the moment the fully numerical calculations coincide with the numerical solution of the Green's function approach, it would also be valuable to find the analytical solution from the latter.

Finally, it was recently pointed out that at zero-temperature the atom-field entanglement can play a significant role [96] and therefore treating our system in a full quantized mode could lead to additional insights. Small atomic systems coupled

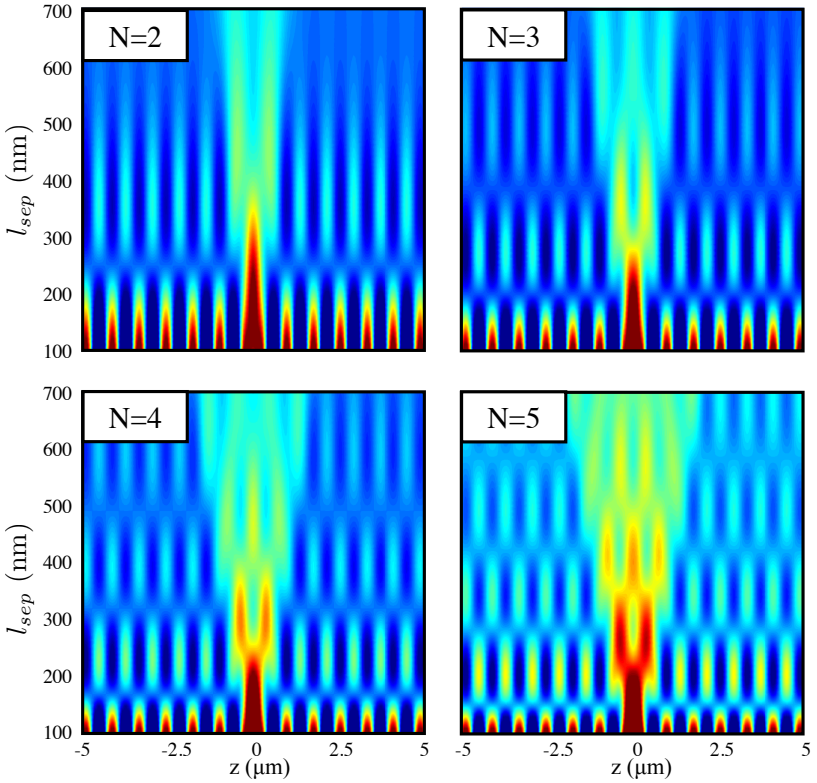


FIGURE 6.11: Real part of the scattered electric field E_S for Tonks gas systems of different particle numbers and for different values of the trap size l_{sep}.

controllably to optical modes would not only be interesting for studying fundamental aspects of physics, but would also be valuable for constructing quantum technology devices, in particular in quantum information.

While research in this area is interesting from a fundamental point of view, ultracold atoms are also well-suited candidates for observing concepts and ideas in quantum information [97].

The idea for the project was developed jointly between myself and Thomas Busch. All calculations were carried out by myself.

Chapter 7

Rotating Phase Separated Bose–Einstein Condensates in a Ring Trap

7.1 Abstract

This chapter explores the superfluid properties of a two-component Bose–Einstein condensate in a toroidal trap as a function of rotation and intra- and inter-species interaction energies. These systems allow for two different kinds of phase separation, radial and azimuthal, and the conditions and consequences of each of these are discussed. In the early part of the Chapter, after presenting the background theory, I numerically determine the conditions for radially phase separated ground states to exist. In the latter part, a published work is enclosed where we show that an azimuthal phase separation process can lead to the breaking of one of the hallmarks of superfluid flow, namely the quantization condition on circulation. In this case, the resulting, non-quantized currents are stable for long times and possess a phase boundary that exhibits classical solid body rotation, despite the quantum nature of superfluid flow.

7.2 Introduction

Beginning in the 1930s, the theory of superfluidity was developed mostly with the aim of explaining the remarkable transport properties of liquid Helium-4 (^{4}He) cooled below its critical temperature ($T_\lambda = 2.17$ K) [3, 98, 99]. However, superfluid ^{4}He is a liquid rather than a gas, and although its underlying BEC nature is fundamental to its superfluid properties, the interactions between the atoms are relatively strong which means that it is not straightforward to describe. In the last 20 years, the achievement of BEC in rubidium, cesium and the other alkalis, has allowed access to systems where superfluid phenomena are more easily isolated and observed. A very successful formulation of superfluid theory uses a picture where a superfluid system comprises a condensate and elementary excitations. This means that the flow patterns that can exist in a BEC in superfluid phase are constrained by the existence of a single macroscopic wave function. The study of the response of such a system to rotation results therefore in some striking signatures of superfluidity, for example the formation of quantized vortices. In recent years many of the signatures of superfluidity, such as frictionless flow below a critical velocity [100], irrotational flow [101], and the formation of vortices with quantized circulation have been experimentally demonstrated [102, 103].

The idea of superflow, or dissipationless flow, first emerged in 1911 when it was observed that the resistance of mercury falls to zero below 4 K [104]. This led physicists to suppose that, if a substance truly had no resistance, then a current flowing in it would remain forever and could be described as a persistent current. Since that time, experiments have shown that persistent currents can, at least in principle, persist on timescales comparable with the age of the universe [105]. Persistent currents represent one of the strongest signatures of superfluidity, but they become unstable above a certain velocity threshold [106]. Despite a growing number of interesting theoretical and experimental works [107–114], some important questions about the superfluid properties of BECs and when they possesses stable persistent currents, remain to be answered.

As the experimental techniques for controlling and investigating cold gases have advanced, they continue to become an even richer testbed for studying superfluidity. An interesting system that has been realized in a number of physics laboratories in recent years is the spinor condensate, which allows for the study of interpenetrating superfluids. In this work we are looking at the example of a two-component condensate trapped in a two-dimensional toroidal trap, where angular momentum is associated with one or both components. This angular momentum might be due to rotation of the external trapping potential, or transferred to one or both of the components by a Raman transfer of atoms between two spin states, for example using a Laguerre-Gauss beam [113, 115, 116]. The interaction parameters associated with the two gaseous components can be tuned in a way that determines whether the mixture is miscible or immiscible (phase separated) and the ground states associated with each take on a variety of interesting forms.

In this chapter I investigate the different kinds of ground state possible in a two-component Bose–Einstein condensate within the framework of mean-field theory. The interaction between the two components can be adjusted to alter the location of each component and probe the transition between miscibility and immiscibility.

The chapter is organized as follows. In Section 7.3 I present a description in terms of a pair of coupled Gross–Pitaevskii (GP) equations, and the associated background theory relevant to the system. Section 7.4 presents my calculations of radially phase separated ground states, which is unpublished work that we are currently preparing for publication. The work on azimuthally phase separated condensates is presented in Section 7.5 and in Section 7.6 I conclude.

7.3 Superfluidity and Spinor Systems

7.3.1 Gross–Pitaevskii Picture

Two dilute bose-condensed gases with wavefunctions Ψ_1 and Ψ_2, self-interaction constants g_{11} and g_{22} and mutual-interaction constant $g_{12} = g_{21}$ can be described

by two coupled Gross–Pitaevskii (GP) equations in the limit of zero temperature [117, 118],

$$i\hbar\frac{\partial\Psi_1(r,t)}{\partial t} = \left[-\frac{\hbar^2\nabla^2}{2m} + V_1(r) + Ng_{11}|\Psi_1(r,t)|^2 + Ng_{12}|\Psi_2(r,t)|^2 - \mathbf{\Omega}_1\hat{L}_1\right]\Psi_1(r,t), \tag{7.1}$$

$$i\hbar\frac{\partial\Psi_2(r,t)}{\partial t} = \left[-\frac{\hbar^2\nabla^2}{2m} + V_2(r) + Ng_{22}|\Psi_2(r,t)|^2 + Ng_{21}|\Psi_1(r,t)|^2 - \mathbf{\Omega}_2\hat{L}_2\right]\Psi_2(r,t). \tag{7.2}$$

For simplicity we assume that each component is in a different hyperfine state (j = 1, 2) of the same atomic species, so that $m_1 = m_2 = m$ [113, 119], and that each component contains an equal number of atoms, $N_1 = N_2 = N$. The rotational energy acquired by the condensates is dependent on the frequency of the externally imposed rotation, Ω_j, which is assumed to be around the z-axis, $\mathbf{\Omega}_j = \Omega_j\mathbf{z}$. The external trapping potentials are given by V_j.

The coupling constants, $g_{ij} = \sqrt{8\pi}\hbar^2 a_{ij}/(ma_z)$, describe atom-atom interactions in terms of the three-dimensional scattering lengths, a_{ij}, and the characteristic harmonic oscillator length in the z direction, $a_z = \sqrt{\hbar/m\omega_z}$. For simplicity we choose the s-wave scattering lengths within each component to be equal, that is $a_{11} = a_{22} = a$, and for both species to experience the same out-of-plane trapping frequencies, ω_z. This leads to $g_{11} = g_{22} = g$, which we will assume to always be positive. In the absence of interaction the GP equation becomes a linear Schrödinger equation, and one can use the single particle solution to describe each component separately.

In the absence of an external trapping potential and rotation the condition for miscibility of the two components is given by [117]

$$g_{11}g_{22} \geq g_{12}^2, \tag{7.3}$$

and the system will phase separate if this condition is broken. In the presence of an external trapping potential (as in the system we consider below) the density is inhomogeneous and therefore the exact point of phase separation will be moved slightly from that defined here [107, 120].

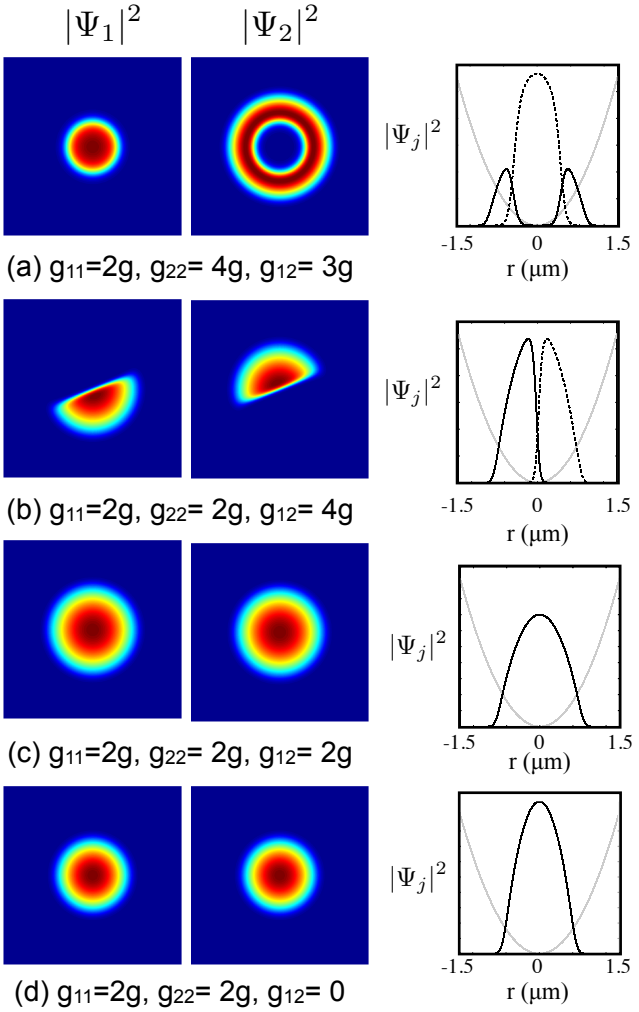


FIGURE 7.1: Examples of miscible and immiscible states in a two-component BEC in a harmonic trap. Each row is described in more detail in the text. The plots on the right hand side show a cut through the density distributions.

In Fig. 7.1 a selection of the different possible ground states for a two-component BEC in a harmonic trap are shown. By varying the interaction parameters, the ground state can be either miscible, or phase separated. Examples (a) and (b) show situations where the two components phase separate ($g_{12}^2 > g_{11}g_{22}$), however in (a) this separation is radial since $g_{11} \neq g_{22}$, whereas in (b) it is azimuthal because $g_{11} = g_{22}$. Examples (c) and (d) both show situations in the miscible regime and demonstrate that a repulsive intercomponent interaction can lead to a lower density overall. All densities are normalized to one, and the trapping potential is shown in the background in the plots on the right hand side as a guide.

7.3.2 Vortices and Persistent Currents

One of the fundamental excitations of a superfluid is a vortex structure. It is defined as a point of zero density around which there is a circulating flow obeying $\nabla \times \mathbf{v}_s = 0$, except at the center [121]. In cylindrical polar coordinates, where $\hat{\mathrm{e}}_r$, $\hat{\mathrm{e}}_\phi$ and $\hat{\mathrm{e}}_z$ are unit vectors in the r, ϕ and z directions, and $\mathbf{v}_s = v_r\hat{\mathrm{e}}_r + v_\phi\hat{\mathrm{e}}_\phi + v_z\hat{\mathrm{e}}_z$

$$\nabla \times \mathbf{v}_s = \frac{1}{r}\begin{vmatrix} \hat{\mathrm{e}}_r & r\hat{\mathrm{e}}_\phi & \hat{\mathrm{e}}_z \\ \frac{\partial}{\partial r} & \frac{\partial}{\partial \phi} & \frac{\partial}{\partial z} \\ v_r & rv_\phi & v_z \end{vmatrix} , \tag{7.4}$$

which means that the condition $\nabla \times \mathbf{v}_s = 0$ is met if $\frac{1}{r}\frac{\partial}{\partial r}(rv_\phi) = 0$. This leads to a flow velocity given by

$$\mathbf{v}_s = \frac{\kappa}{2\pi r}\hat{\mathrm{e}}_\phi, \tag{7.5}$$

where the net circulation is denoted by κ.

There is a close link between the physics of a quantum vortex, and that of a persistent flow around a ring. To understand when persistent currents might be possible, it is helpful to consider the flow velocity, $\mathbf{v_s}(\mathbf{r})$, associated with the wavefunction $\Psi(\mathbf{r}) = |\Psi(\mathbf{r})|e^{i\phi(\mathbf{r})}$

$$\mathbf{v}_s(\mathbf{r})\psi(\mathbf{r}) = -i\frac{\hbar}{m}\nabla\Psi(\mathbf{r}) \, . \tag{7.6}$$

If the gas is uniform, $|\Psi(\mathbf{r})| = C$ (with C a constant), then $\mathbf{v}_s = \frac{\hbar}{m}\nabla\phi(\mathbf{r})$ from which it is evident that $\nabla \times \mathbf{v}_s(\mathbf{r})$ is proportional to $\nabla \times \nabla\phi(\mathbf{r}) = 0$. This can be interpreted to mean that any net circulation in a uniform system has to be zero. However, since a closed flow happens along a well-defined path, the geometry of the underlying system needs to be taken into account.

If, in a given geometry, a path between any two points can be continuously deformed to realize all of the possible paths between these two points then that geometry is called simply-connected. A geometry is said to be multiply-connected if this

condition is not met. In a condensate the geometry can be multiply-connected if either the trap itself is multiply-connected, or if a vortex within the system causes a region of zero density.

The integral of the flow velocity along a path $\mathbf{l}$ can be written as

$$\frac{m}{\hbar}\int_{\mathbf{r}_1}^{\mathbf{r}_2}\mathbf{dl}\cdot\mathbf{v}_s=\phi(\mathbf{r}_2)-\phi(\mathbf{r}_1), \tag{7.7}$$

and it is clear that a simply connected geometry requires $\frac{m}{\hbar}\oint_{\mathbf{r}_1}^{\mathbf{r}_1}\mathbf{dl}\cdot\mathbf{v}_s=0$. Therefore a flow along a closed path cannot exist (see Fig. 7.2a). Circulation in a multiply-connected geometry, however, is permissible if the closed path encircles a point of zero density. In this case $\frac{m}{\hbar}\oint_{\mathbf{r}_1}^{\mathbf{r}_1}\mathbf{dl}\cdot\mathbf{v}_s=2\pi\kappa$, and circulation is allowed as long as it is quantized in units of 2π (see Fig. 7.2b) [122].

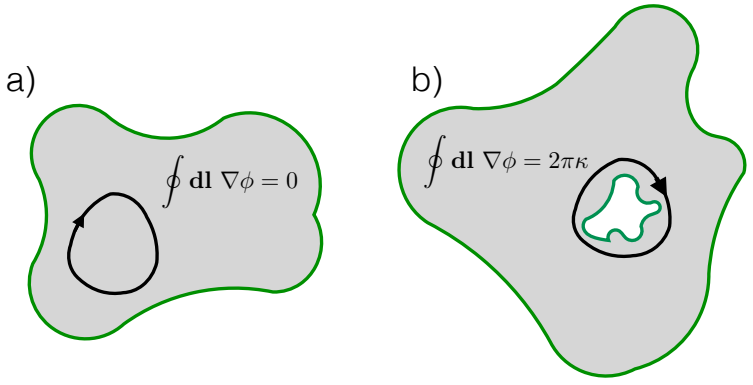


FIGURE 7.2: (a) is an example of a simply-connected trapping geometry. The net circulation around any closed path must be zero. (b) shows a multiply-connected trapping geometry. The net circulation along a path like the one indicated can be any integer multiple of 2π. Recreated from Fig. 2.2 in [122].

As seen above, the ground states possible in two component systems belong to two regimes, miscible and phase-separated, which have different sets of spatial properties, excitation spectra, and stability criteria. The physics of persistent currents can therefore vary a great deal across these regimes and in the phase separated regime the presence of domain walls can lead to new physics.

In the preprint in Sec. 7.5.1 of this Chapter, we discuss a scenario where the condition of quantized rotation is broken due to azimuthal phase separation between the two components in a toroidal trap. This symmetry breaking results in changing the multiply-connected toroidal geometry into two individual simply-connected ones and, as we will show, this leads to a change from superfluid to quasi solid-body rotation. This change has interesting consequences, as in the superfluid situation the atomic velocity has a $\frac{1}{r}$ dependence, which means that atoms closer to the vortex core move faster than atoms farther away, whereas for a solid body the dependence is usually considered to be proportional to r.

In order to have persistent currents, a multiply connected trap is necessary and the simplest possible form for our purpose is given by a two-dimensional ring. This will be discussed in the next section.

7.3.3 Toroidal Traps

As mentioned before, we are interested in the simple multiply connected potential realized by a toroidal trap, which has recently been the subject of strong experimental interest [115, 123, 124]. Persistent currents in single component condensates have been shown to exist for up to 40 seconds in [115], and for over two minutes in [113]. However, superflow in toroidally trapped miscible two-component condensates has been observed only on much shorter timescales, with no rotation at all remaining after 20 s in [113].

Since we are only interested in azimuthally symmetric potentials, we can restrict the treatment here to a radial co-ordinate. In its simplest form a suitable potential can be written as a displaced harmonic oscillator given by

$$V_j = \frac{1}{2} m\omega_r^2 (r - r_0)^2, \tag{7.8}$$

where r_0 is the toroidal radius, $r^2 = x^2 + y^2$, and ω_r is the radial trapping frequency, identical for both components.

Experimentally a number of techniques can be used to create toroidal potentials. Ring traps formed by passing a repulsive barrier, the Gaussian beamwaist of a blue-detuned laser, through the center of a harmonic potential have been demonstrated [115, 123, 125, 126]. These can be modelled as $V = \frac{1}{2}m\omega^2 r^2 + V_0 e^{-2r^2/\sigma_0^2}$, where ω is the radial trapping frequency of the standard harmonic oscillator potential, σ_0 is the beam waist of the blue-detuned laser and V_0 is its strength. Such setups allow control over the height of the central barrier, as this is proportional to the beam intensity, and therefore make it possible to convert between toroidally shaped traps and harmonic potentials. A second possibility is to create all-optical traps by using a red-detuned Laguerre-Gauss beam (often created using a hologram) [113, 115, 127]. A novel optical ring lattice, created by combining Laguerre-Gauss modes has also been proposed [128]. Alternatively, and especially related to the work presented in this thesis, ring-shaped trapping potentials can be produced in the evanescent field of a nanofiber [16, 17]. Such traps have the advantage that the fiber at the center can be used to deliver light in a specific way to the trapped atoms, and it also provides a well defined region of zero density at the center. However, the use of toroidal nanofiber traps also presents some obstacles. For example, the presence of a solid, dielectric fiber at the center of the experiment would make carrying out time-of-flight (TOF) measurements impossible. Furthermore, the evanescent field potentials are limited in range and the dimensions of the trap are restricted to the scale of the evanescent decay lengths. A direct comparison between a two-color nanofiber trap, as described earlier in this thesis and in the paper in Chapter 3 [129], and the shifted harmonic oscillator potential used in some of our calculations below, can be seen in Fig. 7.3. The evanescent field potential is given for a fiber of radius $a = 150$ nm and the wavelengths of the two lasers used to make it are $\lambda_b = 640$ nm and $\lambda_r = 1064$ nm. These are blue- and red-detuned about the dominant D2 transition in Rubidium 85 ($\lambda_{Rb} = 780$ nm) and the powers of the two associated laser fields are $P_b = 35$ mW and $P_r = 30$ mW. For the harmonic oscillator potential we choose $\omega = 2\pi \times 30000$ kHz, the mass of rubidium is $m = 85$ a.m.u. and we choose trap parameters such that $r_0 = 400$ nm. It is clear that, while the choice of trap will undoubtedly make a quantitative differences to any

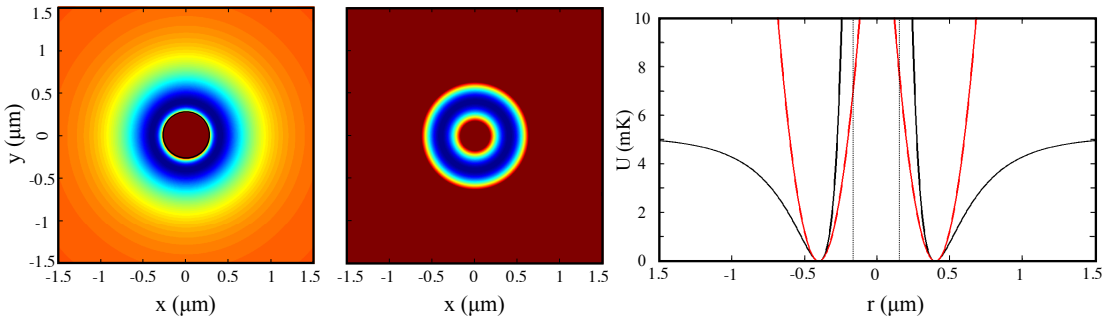


FIGURE 7.3: The left hand panel shows the evanescent field potential around a nanofiber and the panel in the middle shows the shifted harmonic oscillator potential. The panel on the right shows a radial cut through both potentials, with the black line being the evanescent field potential around the fiber for the parameters given in the text. The red line is a harmonic oscillator potential which has a similar frequency to the evanescent field potential at its deepest part. One can see that the evanescent field potential is asymmetric around the minimum, with its inner wall being much steeper than the outer-wall. Additionally, the evanescent field potential is bounded. Further details and parameter values are given in the text.

results, qualitatively similar behavior can be expected when the system's energy is low.

In Fig. 7.4, we show some examples of ground states in a toroidal trap, when neither component has angular momentum and $\Omega_1 = \Omega_2 = 0$ Hz. Panel (a) shows a state in the miscible regime ($g_{11} = g_{22} = g$, $g_{12} = 0.5g$) and azimuthally homogeneous density distributions for both components are clearly visible. In panel (b), where the scattering parameters are chosen to be on the border between the miscible and immiscible regime ($g_{11} = g_{22} = g_{12} = g$), the first appearance of in-homogeneities in the density distribution can be seen. Finally, panel (c) shows a system deep in the phase-separated regime ($g_{11} = g_{22} = g, g_{12} = 1.5g$), where it is evident that the state is azimuthally symmetrically split. In (c), the splitting angle is determined by random noise added numerically. For tight traps, i.e. when the trap width is smaller than the circumference, this kind of azimuthal phase separation is always energetically favourable to a radial one [114, 130, 131], while in wider toroidal traps concentric ring configurations can occur (see for instance [114, 131]).

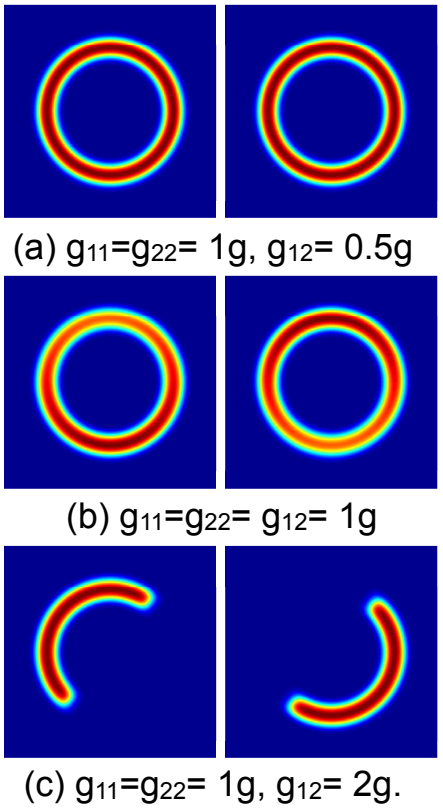


FIGURE 7.4: Ground states for two-component condensates in the absence of angular momentum. In (a) $g_{11} = g_{22} = g$ and $g_{12} = 0.5g$, which results in a uniformly mixed state. In (b) the parameters are on the border between the miscible and immiscible regime, $g_{11} = g_{22} = g_{12} = g$, and an in-homogeneity in the density distribution can be seen. In (c) the system is deep in the phase separated regime, $g_{11} = g_{22} = g$ and $g_{12} = 1.5g$, which results in a symmetrical azimuthally phase separated state.

In the next section we will show that the inclusion of angular momentum can lead to the appearance of a radially phase separated ground state.

7.4 Radial Phase Separation

An interesting scenario in which to examine the ground state of a two-component condensate in the phase separated regime in a toroidal trap is the situation where one component has no angular momentum and the other has a large amount. To achieve this we will assume $\mathbf{\Omega}_1 = 0$ and $\mathbf{\Omega}_2$ large in all calculations presented in this chapter.

The presence of angular momentum in one of the components leads to a centrifugal force that draws this component towards the outer edge of the toroidal trap. When this is combined with the presence of large repulsive interaction between the two components (i.e. large $g_{12} \gg \sqrt{g_{11}g_{22}}$), radial phase separation can become energetically favorable over azimuthal phase separation at some point as the overlap in their densities decreases.

All simulations in this chapter have been carried out using a real-space mesh of $2^9 \times 2^9$ points. The algorithm we have used for imaginary-time propagation is based on the split-operator method [132]. In the next section we will systematically explore the changeover from an azimuthally phase separated ground state to one that is radially phase separated.

7.4.1 The Transition from Azimuthal to Radial Phase Separation

As the phase separation dynamics in multicomponent BECs is an energetically driven process, it depends on the detailed interplay between kinetic, rotational and non-linear energies. While it was argued in the last section that radial phase separation is possible, determining the values for its first appearance is the aim of this chapter. It is clear that for low amounts of angular momentum azimuthal phase separation is strongly favorable, whereas for increasing rotation the radial overlap reduces and at some point it becomes energetically cheaper to radially phase separate. However, as the exact trapping geometry and size of the system are playing a role in determining quantitative parameters, we will here only show that this transition point exists for experimentally realistic numbers.

While one could examine the density distribution each time to establish the kind of phase separation the system has undergone, here we take advantage of the insight, that for azimuthally phase separated condensates the expectation value of the angular momentum does not need to be quantized. A non-integer number therefore indicates azimuthal phase separation and in Fig. 7.5 these numbers are

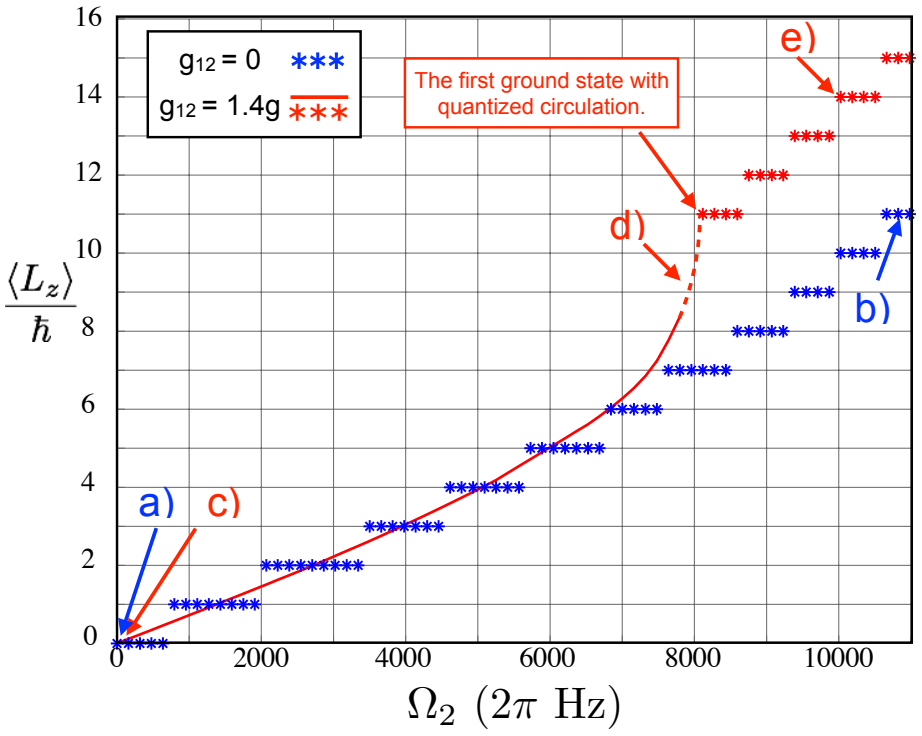


FIGURE 7.5: Angular momentum in the ground states of the miscible (blue) and immiscible (red) regimes, in component with angular momentum, $|\Psi_2|^2$. Quantization of winding in the miscible regime is clear from the staircase pattern, where the stairs only have integer values. As the external trap rotation for Ψ_2 increases, we see that there is a transition from where the quantization condition does not hold, to where it does.

given for the ground state of systems in the miscible (blue) and immiscible (red) regime as a function of increasing rotation applied to the second component. One can see that in the miscible regime the system always adheres to the requirement of having a quantized winding number, which is consistent with the expectation. In the immiscible case, however, the expectation value of the angular momentum shows a continuous increase for small values of the applied rotation, indicating that the system is azimuthally phase separated. Once Ω_2 exceeds a certain value, the quantized behaviour returns, indicating that the system is no longer azimuthally phase separated.

These interpretations can be confirmed by looking at the density distributions for certain values, indicated in Fig. 7.5 and shown in Fig. 7.6. For points (a) and (b) in the miscible regime one can see the expected azimuthally homogeneous

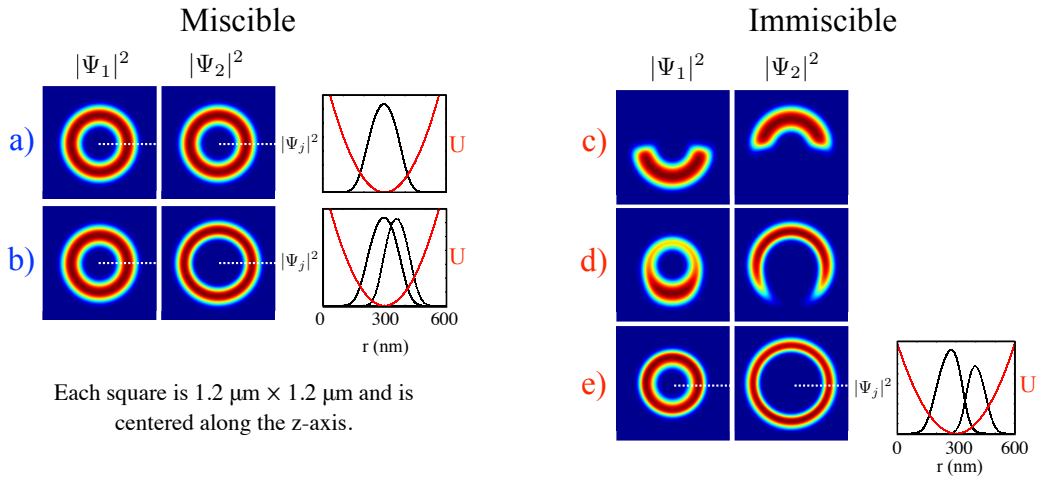


FIGURE 7.6: Density distributions corresponding to the points indicated in Fig. 7.5. Where a radial cut is present, in (a), (b) and (e), the origin is indicated by the dotted line in the full 2D plots. The trapping potential is also indicated in red as a guide for the eye but does not correspond to the same scales and axes.

distribution and also the fact that the angular momentum carrying component, $|\Psi_2|^2$, represented by the dotted line in the cut, is sitting farther out in the trap.

The point (c) corresponds to an immiscible state where neither $|\Psi_1|^2$ nor $|\Psi_2|^2$ have any angular momentum and where the ground state is azimuthally phase separated. As Ω_2 increases, quantized circulating states appear and the first one is indicated in the graph. However, just below this transition frequency (indicated by the dashed part of the red line), the states are not cleanly azimuthally phase separated, as can be seen from the density distribution corresponding to point (d). In this region the states are at the transition between azimuthally phase separated and fully radially phase separated. Finally, an immiscible state where $|\Psi_1|^2$ has no angular momentum and $|\Psi_2|^2$ has 11 units is shown for (e). One can see that the system is now in a fully radially phase separated state.

The simulation parameters used in Figs 7.6 and 7.5 are $\omega_r = 2\pi \times 30000$ Hz, $r_0 = 0.3\,\mu$m and $Ng_{11} = Ng_{22} = g = 1.1095 \times 10^{-41}$ (Js)^2 kg $^{-1}$.

7.4.2 Variational Calculation

In order to determine the influence of the phase separation process on the ground states obtained above and distinguish it from the separation due to the centrifugal force, we will carry out a variational calculation in this section. As we are only interested in the radially phase separated state, we can take advantage of the azimuthal symmetry to simplify the calculations.

The variational principle says that if one assumes a trial wavefunction $|\Psi\rangle$ and calculates the energy expectation value

$$E(\Psi) = \frac{\langle\Psi|\hat{H}|\Psi\rangle}{\langle\Psi|\Psi\rangle}, \tag{7.9}$$

where $\langle\Psi|\hat{H}|\Psi\rangle = \int \Psi^* \hat{H}\Psi dx$, this value gives an upper bound to the true ground state energy, i.e. $E(\Psi) \geq E_0$. Minimizing a number of free parameters in a trial wavefunction can therefore provide us with a good approximation to the real ground state.

In our case the energy functional of the system of two coupled GP equations (eqs. (7.1) and (7.2)) is given by

$$E(\Psi_1, \Psi_2) = \int dr \Bigg(\underbrace{\frac{\hbar^2|\nabla\Psi_1|^2}{2m}}_{\substack{\text{kinetic energy}\\ \text{component 1}}} + \underbrace{\frac{\hbar^2|\nabla\Psi_2|^2}{2m}}_{\substack{\text{kinetic energy}\\ \text{component 2}}} + \underbrace{V(|\Psi_1|^2 + |\Psi_2|^2)}_{\text{potential energies}} + \underbrace{\frac{1}{2}g_{11}|\Psi_1|^4}_{\substack{\text{interaction in}\\ \text{component 1}}} + \underbrace{\frac{1}{2}g_{22}|\Psi_2|^4}_{\substack{\text{interaction in}\\ \text{component 2}}} + \underbrace{g_{12}|\Psi_1|^2|\Psi_2|^2}_{\substack{\text{interaction between}\\ \text{components}}} \Bigg). \tag{7.10}$$

Because we will be considering states with given and well defined winding numbers, the $-\Omega L$ terms do not appear in this functional and we instead choose appropriate trial wave-functions.

In order to find a good variational ansatze for the condensates we need to consider both, the form of the density and the contribution from the in-homogeneous phase, while also taking advantage of the symmetry of the system. As the potential is

built from displaced harmonic oscillators, we choose (using cylindrical coordinates)

$$\Psi_1(r,\kappa_1) = N_1\, r e^{-A_1(r-R_1)^2} e^{i2\pi\kappa_1}, \tag{7.11}$$

$$\Psi_2(r,\kappa_2) = N_2\, r e^{-A_2(r-R_2)^2} e^{i2\pi\kappa_2}, \tag{7.12}$$

where A_i accounts for the width of the wavefunction and R_i allows for positioning the maximum of the Gaussian function. The normalization is given by the constants N_i, which are carried through the variational calculation as constraints. This reduces the number of variational parameters by two and means that ultimately we have four variational parameters A_1, A_2, R_1, and R_2.

Since the calculations are long winded and the obtained expressions rather unwieldy (see Appendix A for the detailed forms of the expectation values), the minimization process for the variational parameters is carried out numerically. From this, the position of the maxima of the density can be determined as

$$R_{i,\max} = \frac{A_i R_i + \sqrt{A_i^2 R_i^2 + 2A_i}}{2A_i}\,. \tag{7.13}$$

where $i = 1, 2$ for the first and second component respectively. The distance between the two maxima, R_{gap}, is given by

$$R_{\mathrm{gap}} = \frac{1}{2}\left(\frac{\sqrt{A_2\,(A_2R_2^2+2)}}{A_2} - \frac{\sqrt{A_1\,(A_1R_1^2+2)}}{A_1} - R_1 + R_2\right). \tag{7.14}$$

The variational results for the position of the maxima of the individual density distributions are compared to the numerically exact ones in Fig. 7.7. The unfilled shapes correspond to the maxima of $|\Psi_1|^2$, which is the non-rotating component, and the filled shapes correspond to $|\Psi_2|^2$. The horizontal red line indicates the position of the trap minimum at $r_0 = 300$ nm. Ground states in the miscible regime are circular and correspond to any point on the blue plateaus in Fig. 7.5. Ground states in the immiscible regime are diamonds and correspond to any point on the red plateaus in Fig. 7.5. The data resulting from the variational calculation

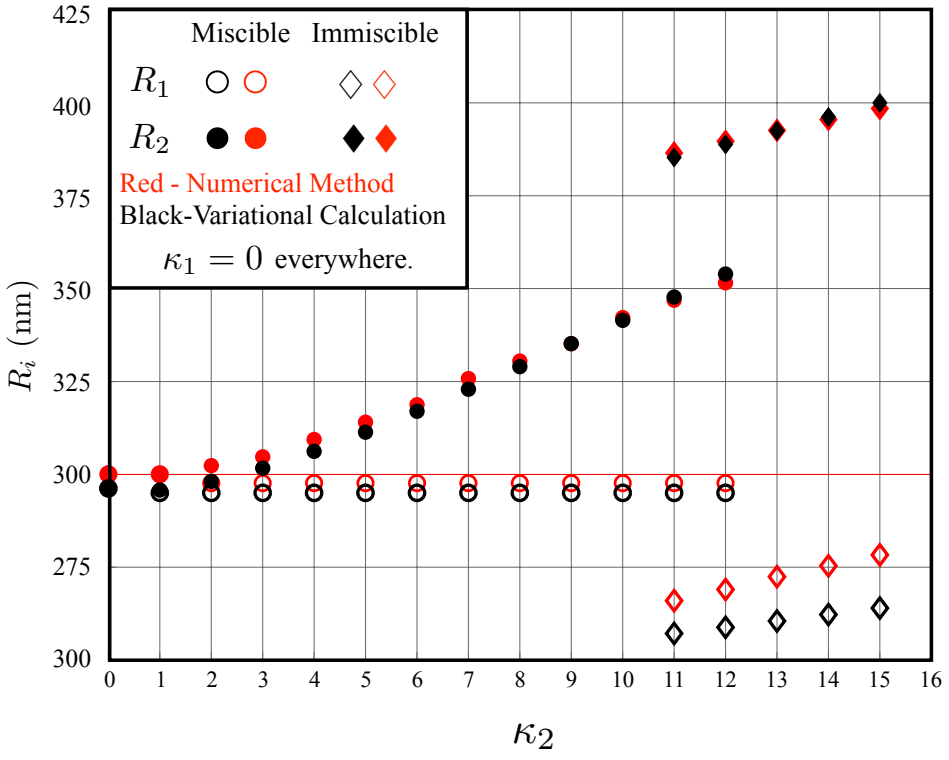


FIGURE 7.7: Position of the maximum of the density distribution for increasing winding number for miscible and immiscible systems. The trap parameters here are the same as in Fig. 7.5, i.e. $\omega_r = 2\pi \times 30000$ Hz, $r_0 = 0.3\,\mu$m and $g = 1.1095 \times 10^{-41}$ (Js)^2 kg^{-1}.

is in black and data from the numerical ground-state finding program is in red. One can see that excellent agreement between the two approaches exists.

A comparison of the density distributions obtained from the variational and the numerical method is shown in Fig. 7.8, for two examples with the same external rotation, $\Omega_2 = 2\pi \times 9000$ Hz, but with different values of g_{12}. The parameters used are the same as in Fig. 7.5. It is interesting to note that for the same external rotation, the second component acquires a different winding in the miscible and immiscible states. In the left panel, the miscible case, $|\Psi_2|^2$ has eight units of winding and so it gains a centrifugal contribution which pushes it further from $r = 0$ than $|\Psi_1|^2$, which carries no angular momentum. As $g_{12} = 0$ in this panel, the separation is completely due to the centrifugal force. The right panel is in the immiscible regime and $|\Psi_2|^2$ has twelve units of phase winding. From Fig. 7.5 one can see that this is in the regime where it is energetically favorable for $|\Psi_2|^2$ to sit

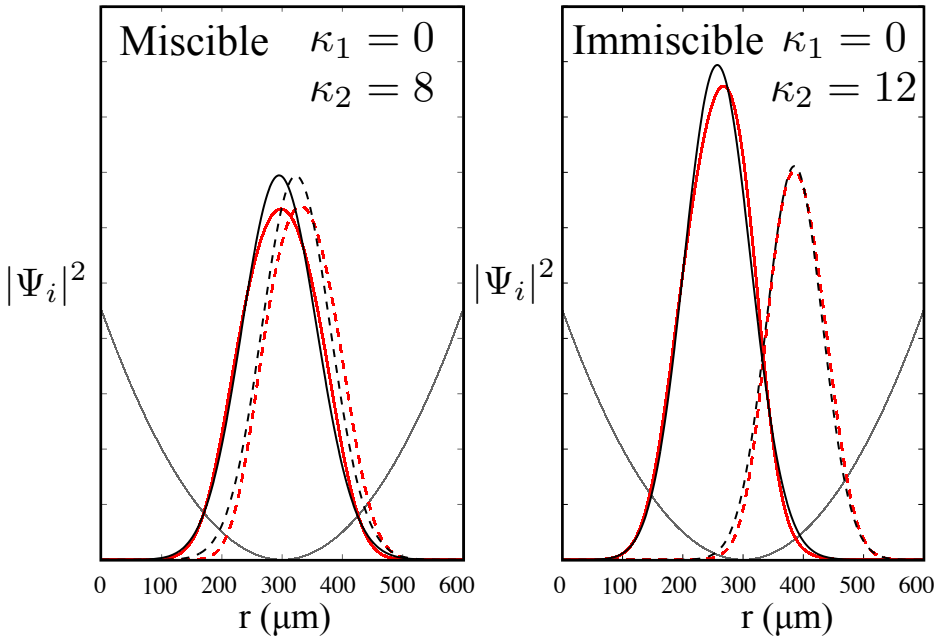


FIGURE 7.8: Comparison of the densities obtained by variational (black) and numerical calculation (red). $|\Psi_1|^2$ is represented by the solid lines and $|\Psi_2|^2$ is represented by the dotted lines.

outside $|\Psi_1|^2$ and that the ground state is radially symmetric. In this situation the inter-component interaction pushes $|\Psi_2|^2$ away from the centre and it therefore effectively sees a trap with larger radius and higher frequency leading to a higher κ_2.

While this variational calculation gives results that agree very well with our numerical calculations, it only does so in the range where the phase separation is radially symmetric, rather than azimuthal. Since the variational calculation gives a one dimensional solution along the radial direction, it is not useful for finding ground states that have significant variation in the azimuthal direction. The range over which the variation approach is useful must be informed by numerical simulation.

7.5 Azimuthal Phase Separation

The following section contains a preprint, currently submitted to Phys. Rev. Lett., in which the transition between miscibility and phase separation in rotating toroidally

trapped two-component condensates is discussed. In the phase separated regime the requirement of quantization of circulation is broken and azimuthally phase separated superfluids can rotate with arbitrary circulation. As the phase separation also leads to the presence of a phase boundary, we show that energetic considerations force the system to undergo solid body rotation. This is a novel demonstration of the coexistence of classical and quantum behaviors, which can be observed in current state of the art cold-atom experiments.

7.5.1 Emergence of Classical Rotation in Superfluid Bose–Einstein Condensates (paper)

Manuscript Information

Manuscript Title: Emergence of Classical Rotation in Superfluid Bose–Einstein Condensates.

Journal Information: Phys. Rev. A **93**, 033601(2016).

Authors: Angela White, Tara Hennessy, and Thomas Busch

DOI: 10.1103/PhysRevA.93.033601

The idea for the project was jointly developed between Angela White, Thomas Busch and myself. The calculations for the radial phase separation were carried out by me, whereas Angela White lead the work on the azimuthal phase transition. The interpretation of the results was a joint effort between all three members in this project.

Emergence of Classical Rotation in Superfluid Bose-Einstein Condensates

Angela White,[1] Tara Hennessy,[1] and Thomas Busch[1]

[1] *Quantum Systems Unit, Okinawa Institute of Science and Technology Graduate University, Onna-son, Okinawa 904-0495, Japan.*

Phase transitions can modify quantum behaviour on mesoscopic scales and give access to new and unusual quantum dynamics. Here we investigate the superfluid properties of a rotating two-component Bose–Einstein condensate as a function of changes in the interaction energy and in particular through the phase transition from miscibility to immiscibility. We show that the breaking of one of the hallmarks of superfluid flow, namely the quantisation condition on circulation, is continuous throughout an azimuthal phase separation process and displays intriguing flow dynamics. We find that the resulting currents are stable for long times and possess a boundary between the two condensate components that exhibits classical solid body rotation, despite the quantum nature of superfluid flow. To support this co-existence of classical and quantum behaviour the system develops a unique velocity flow profile, which includes unusual radial flow in regions near the boundary.

Phase transitions in quantum systems can have a dramatic impact on the quantum mechanical behaviour on mesoscopic scales. Superfluidity in Bose-condensed gases is a mesoscopic manifestation of quantum mechanical effects and one of its hallmarks is the existence of quantised flow around phase singularities as a response to external rotation [1–4]. However, as the quantisation condition arises from the requirement of the single-valuedness of the wavefunction, an interesting, and less well investigated, generalization appears in superfluids composed of several components. In these systems, due to the interplay of intra- and inter-component interactions, the spinor order parameter can undergo a phase transition that modifies the global symmetry of the system. As the quantisation condition applies to each component independently, the path along which circulation is determined consequently depends on the presence of the other component. This has proven to be particularly striking in toroidally trapped binary mixtures of BECs, where immiscibility can drive a transition to azimuthal phase separation, breaking the requirement of quantised circulation around the toroid [5]. We show that this transition is continuous and leads to a boundary between the two condensate components which rotates as a classical solid body. While this might seem at first to be incompatible with the quantum nature of superfluid flow, this co-existence can be explained through the presence of a radial flow.

In superfluids the circulation around a closed path p is quantised according to $\oint_{\mathsf{p}} \mathbf{v} \cdot d\mathbf{r} = n2\pi\hbar/m$. Here n is an integer winding number, m the atomic mass, $\hbar$ the reduced Planck constant, and the superfluid velocity field, $\mathbf{v} = \hbar\nabla\theta/m$, is completely determined by the gradient of the condensate phase, θ. This implies the velocity field of a vortex has a tangential $1/r$ velocity profile, in contrast to classical rigid-body rotation, where $\mathbf{v} = \mathbf{\Omega} \times \mathbf{r}$. The creation of vortices is a response to external rotation and many of their properties depend, in particular, on the confining geometry. While in simply connected trapping potentials vortices with higher winding numbers are unstable [6], multiply connected geometries are known to support persistent currents with large angular momentum [7–10].

A simple multiply connected potential can be realised by a toroidal trap, which has recently been the subject of intense experimental interest [7, 9]. For single component condensates superflows have been shown to exist for up to 40 s [11], however the superflow in toroidally trapped miscible two-component condensates has only been observed on much shorter timescales [12].

In this work we first study how the quantisation of circulation breaks down in the transition region between miscibility and phase separation in a rotating, toroidally trapped two-component condensate. While deep in the phase separation regime angular momentum scales linearly with rotation frequency, close to the phase separation point an oscillatory behaviour is found, which is accompanied by significant changes in the order parameter. At the same time, the phase profile, which drives the superfluid flow, adjusts in a way that allows quantum and classical behaviour to coexist.

The system is modelled using two coupled Gross–Pitaevskii (GP) equations, which aptly describe a two-component Bose–Einstein condensate in the limit of zero temperature. Each component is assumed to be a different hyperfine state ($j = 1, 2$) of the same atomic species, $m_1 = m_2 = m$, [12, 13] and to consist of the same numbers of atoms, $N_1 = N_2 = N$. The two-dimensional coupled GP equations for the wave functions ψ_j under rotation around the z-axis with rotation frequency $\vec{\Omega} = \Omega\vec{z}$, are then given by

$$i\hbar\frac{\partial\psi_j}{\partial t} = \left(-\frac{\hbar^2}{2m}\nabla^2 + V_j + \sum_i^{1,2} N g_{ij}|\psi_i|^2 - \vec{\Omega}\cdot\hat{L}\right)\psi_j\,. \tag{1}$$

In order to allow for stable systems with high angular momentum, we assume that the atoms are trapped in a harmonic ring-shaped potential of the form $V_j = \frac{1}{2}m\omega_r^2(r - r_0)^2$, where r_0 is the toroidal radius, $r^2 = x^2 + y^2$, and ω_r is the radial trapping frequency, identical for both components. Toroidal trapping potentials have recently been realised in several experiments by using, for example, a

time-averaged harmonic potential with a Gaussian laser beam through its centre [7] or all optical traps made by applying a red-detuned Laguerre-Gauss mode of a laser beam [8, 11, 12]. Alternatively, ring-shaped trapping potentials which vanish asymptotically can be produced in the evanescent field of an optical nanofiber [14, 15].

The coupling constants, $g_{ij} = \sqrt{8\pi}\hbar^2 a_{ij}/(m a_z)$, describe atom-atom interactions in terms of the three-dimensional scattering length a_{ij}, and the characteristic harmonic oscillator length in the z direction, $a_z = \sqrt{\hbar/m\omega_z}$. For simplicity we choose the s-wave scattering lengths within each component to be equal, that is $a_{11} = a_{22} = a$, and for both species to experience the same out-of-plane trapping frequencies, ω_z. The strength of atom-atom interactions between the two components, g_{12}, will be varied to induce the phase transition.

Homogeneous two-component condensates are miscible for values of $g_{12}^2 < g_{11}g_{22}$ and immiscible or phase-separated when $g_{12}^2 > g_{11}g_{22}$ [16–18]. For trapped condensates these values are slightly shifted due to the inhomogeneous density profile [19, 20] and the density distribution in the phase separated regime is determined by the shape of the external trapping potential. In narrow ring traps (and when $g_{11} = g_{22}$), azimuthal phase separation is favoured (see for instance [5, 21, 22]), while in wider toroidal traps concentric ring configurations can occur (see for instance [21, 22]).

In the following we will show how the phase separation influences the rotational properties of azimuthally separated states and how the existence of a boundary between the two condensate components forces the system to adopt a rotation pattern that mimics solid body rotation. For this we numerically solve the coupled GP equations by applying a pseudo-spectral second order Strang method with symmetric three-operator splitting [23].

When the atom-atom interaction is chosen so that the two superfluid components are miscible, each component is multiply connected and circulation around the toroid is quantised. This implies that for each component the average angular momentum per particle, $\langle L_z\rangle = i\hbar\int d\mathbf{x}\,\psi_j^*\,(y\partial/\partial x - x\partial/\partial y)\,\psi_j$, is also quantised. In stark contrast, azimuthally phase-separated states break the multiply connected nature of each condensate component around the toroid and it was recently shown that they can therefore rotate with arbitrary circulation and angular momentum of any value [5].

As experimentally realistic toroidal condensates are inherently of finite size, the phase-transition takes the form of a continuous transition and in Fig. 1 we show how the breakdown of the quantisation condition across this transition for the above system develops. To do so, we calculate the angular momentum of the stationary state for three values of inter-atom interaction, g_{12}, selected such that the system is either fully miscible, fully immiscible or in the transition region between these two domains. As expected, for g_{12} well in the miscible regime, quantisation of angular momentum in each component is observed (curve with blue asterisks). When g_{12} is chosen

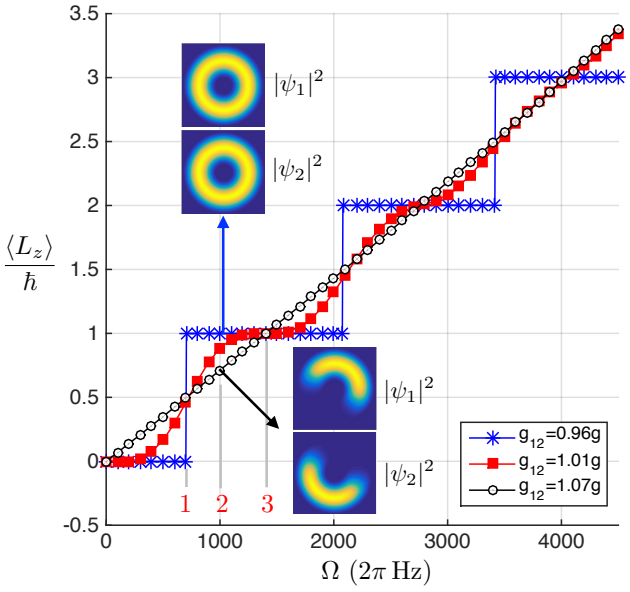


FIG. 1: Phase diagram mapping the transition from quantised steps of angular momentum to linear scaling of $\langle L_z\rangle/\hbar$ with Ω, by varying g_{12} from the miscible to immiscible regime. For g_{12} on the border of miscibility to immiscibility, an oscillatory behaviour, damped with increasing Ω is observed. Simulation parameters: $\omega_r = 2\pi \times 30000\,\mathrm{Hz}$, $\lambda = \omega_z/\omega_r \approx 10$, $r_0 = 0.3\,\mu$m with $Ng = 1.1564 \times 10^{-41}\,(\mathrm{Js})^2\mathrm{kg}^{-1}$. Points labelled 1, 2 and 3 correspond to density profiles in the transition regime, which we plot in Fig. 2.

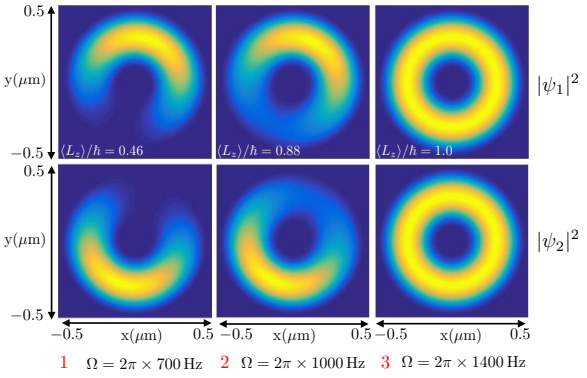


FIG. 2: Condensate density profiles in the transition between the miscible and immiscible regime. These correspond to points labelled 1, 2 and 3 in Fig. 1. Simulation parameters: $g_{12} = 1.01g$, $\omega_r = 2\pi \times 30000\,\mathrm{Hz}$, $r_0 = 0.3\,\mu$m and $Ng = 1.1564 \times 10^{-41}\,(\mathrm{Js})^2\mathrm{kg}^{-1}$.

so that the condensate exhibits clear azimuthal phase-separation, angular momentum can be seen to scale linearly with Ω (curve with black circles). In the intermediate regime ($g_{12} \simeq g$), however, an interesting damped oscillatory dependence of angular momentum with rotation frequency is found. The damping arises as a result of the increased rotation effectively cancelling the harmonic trapping potential, which shifts the value of the critical

interspecies interaction strength at the phase separation point towards the free space result ($g_{12}^C = g$). For larger Ω the chosen interspecies interaction strength $g_{12} = 1.01g$ therefore moves further into the phase separated regime and the curve becomes more linear. The density distributions corresponding to the miscible and immiscible regimes are also displayed in Fig. 1.

On the border between miscibility and immiscibility (curve with red squares in Fig. 1), the density distribution changes as a function of the rotation frequency and three examples corresponding to different angular momenta are shown in Fig. 2. This behaviour can be understood by realising that the rotational energy acquired by the condensate is dependent on the frequency of the externally imposed rotation, Ω. If the system is in a phase-mixed state at a rotation frequency that allows for an integer winding number, it can acquire a certain amount of rotational energy with increasing rotation frequency before it is energetically more favourable to phase separate and adjust the amount of angular momentum. This leads to the observed cycling through mixed and phase separated density distributions for condensates close to the phase boundary.

While in the mixing regime the well known $1/r$ velocity profile characteristic of rotation with quantised angular momentum is exhibited, it is easy to see that in the phase separated regime, where fractional winding numbers appear, this needs to be modified. In fact, if each superfluid component demonstrated a perfect vortex-like velocity profile everywhere, the phase boundaries would shear over time, as the atoms closer to the center of the potential move faster than those at the outer radial edges. This would lead to an increase in the interaction energy and consequently unstable rotation. Instead, to ensure that the boundary between the two condensate components is always as short as possible, i.e. along the radial direction, the system reacts by modifying the velocity profile away from purely azimuthal flow (see Fig. 3).

To understand the flow profile in the phase separated case, we decompose the velocity field into its radial and azimuthal velocity contributions. These correspond to $v_r = \cos(\varphi)v_x + \sin(\varphi)v_y$ and $v_\varphi = -\sin(\varphi)v_x + \cos(\varphi)v_y$ and are shown in Fig. 4. Two regions where the velocity field exhibits distinctly unique behaviour can be clearly identified. In the bulk of each component, the flow displays the characteristic tangential superfluid velocity profile of the form $\mathbf{v} \propto n/r\,\hat{\mathbf{e}}_\varphi$, with $\hat{\mathbf{e}}_\varphi$ a unit vector in the direction of the azimuthal angle φ. In contrast, in the vicinity of the boundary, the velocity field departs from a purely azimuthal profile and a radial flow develops. This is consistent with the fact that each component only reacts to the presence of the other over the scale of the domain wall width [24].

The appearance of the radial flow can be understood by realising that, in order to have minimal length, the boundary between the two condensate components needs to move as a classically rotating object. This leads to a rotation velocity proportional to r, meaning that at

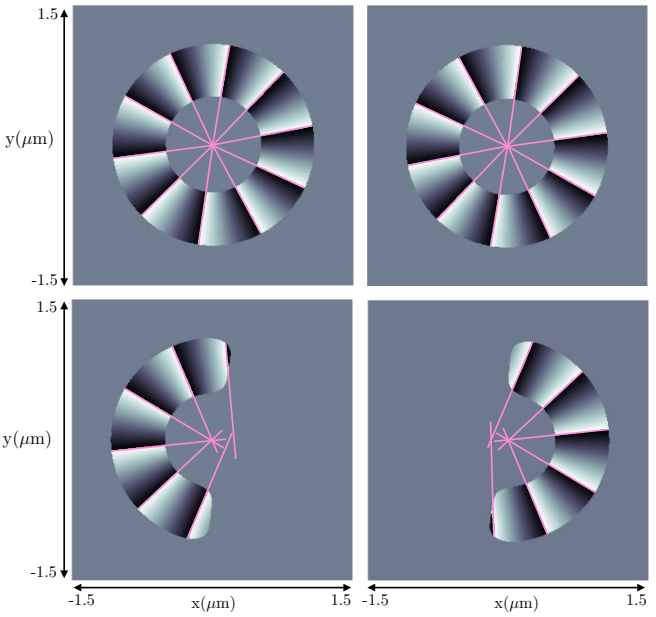


FIG. 3: Phase profile within the condensate, θ_j, with overlaid lines of constant phase (pink) extended towards the central point of the trap.Upper row shows the two components in the miscible regime ($g_{12} = 0.95g$), where the purely azimuthal flow is confirmed by the fact that all lines meet at a single point. The lower row shows the phase separated regime ($g_{12} = 1.6g$) and the presence of a radial flow component is indicated by the absence of a single crossing point. Simulation parameters: $\Omega = 2\pi \times 1910\,\mathrm{Hz}$, $\omega_r = 2\pi \times 8000\,\mathrm{Hz}$, $r_0 = 0.75\,\mu\mathrm{m}$, $Ng = 1.1564 \times 10^{-41}\,(\mathrm{Js})^2\mathrm{kg}^{-1}$.

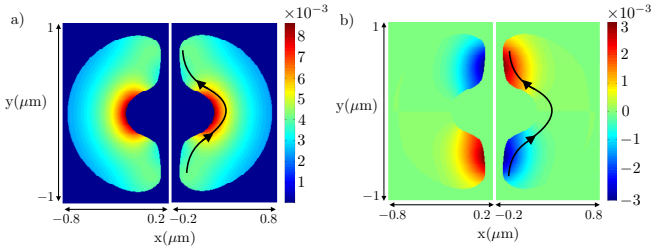


FIG. 4: Decomposition of the condensate velocity into (a) azimuthal and (b) radial components plotted within the condensate edge (defined as 6% of the maximum density $|\psi_j|^2$). Simulation parameters: $\Omega = 2\pi \times 1273\,\mathrm{Hz}$, $\omega_r = 2\pi \times 10000\,\mathrm{Hz}$, $r_0 = 0.5\,\mu\mathrm{m}$, $Ng = 1.1564 \times 10^{-41}\,(\mathrm{Js})^2\mathrm{kg}^{-1}$ and $g_{12} = 1.2g$.

larger radii the boundary has a larger velocity than at smaller radii. As this is in contrast to the $1/r$ velocity profile of the superfluid in the bulk region, the radial flow correctly re-distributes the atoms between the faster flow at smaller radii and the slower flow at larger radii. Behind the boundary, the radial flow leads to the movement of atoms from smaller to larger radii, while at the same time reducing their azimuthal velocity, while in front of the boundary the opposite process takes place, with atoms flowing from larger to smaller radius (see Fig. 4).

The stable, classical solid body rotation of the phase

boundary can be observed when the external rotation is switched off and the system is able to evolve without constraint (see supplementary video 1). As expected, the condensates rotate with an effective rotation frequency, $\Omega_{\rm eff} = \langle v_\varphi / r \rangle$, which corresponds to the frequency of externally imposed rotation, that is $\Omega/\Omega_{\rm eff} \sim 1$.

The above system is therefore an intriguing example where classical behaviour is displayed on a mesoscopic scale, despite the dynamics of the constituents being fully quantum mechanical. Similar behaviour can be found in the rotation of Abrikosov vortex lattices [25]. The emergence of large-scale classical behaviour in systems composed of quantum vortices also occurs in quantum turbulence, which displays classical Kolmogorov scaling on length scales larger than the average inter-vortex spacing [26–30].

In conclusion, we have studied the transition between miscibility and phase separation in rotating toroidally trapped two-component condensates. In the phase separated regime the requirement of quantisation of circulation is broken and azimuthally phase separated superfluids can rotate with arbitrary circulation. However, to minimise the energy of the system, the boundary between the two condensate components has to always be aligned in the radial direction and therefore rotates as an effective solid body within the two-component flow. To resolve the dichotomy between this solid-body rotation, which has a velocity profile proportional to r, with the superfluid vortex profile in the bulk of the components, which is proportional to $1/r$, the system develops an unusual flow pattern involving radial components. This novel demonstration of the coexistence of classical and quantum behaviours can be observed in current state of the art cold-atom experiments.

Acknowledgments

We thank Marta Abad for valuable discussions and input. We acknowledge discussions with K. Rzażewski, P. Engels and L. J. O'Riordan. This work was supported by the Okinawa Institute of Science and Technology Graduate University. We are grateful to JSPS for partial support from Grant-in-Aid for Scientific Research (Grant No. 26400422).

[1] M. R. Matthews, B. P. Anderson, P. C. Haljan, D. S. Hall, C. E. Wieman, and E. A. Cornell, *Vortices in a Bose–Einstein condensate*, Phys. Rev. Lett. **83**, 2498 (1999).

[2] K. W. Madison, F. Chevy, W. Wohlleben, and J. Dalibard, *Vortex formation in a stirred Bose–Einstein condensate*, Phys. Rev. Lett. **84**, 806 (2000).

[3] A. L. Fetter and A. A. Svidzinsky, *Vortices in a trapped dilute Bose–Einstein condensate*, J. Phys.: Condens. Matter **13**, R135 (2001).

[4] P. G. Kevrekidis, R. Carretero-Gonzàlez, D. J. Frantzeskakis, and I. G. Kevrekidis, *Vortices in Bose–Einstein condensates: some recent developments*, Mod. Phys. Lett. B **18**, 1481 (2004).

[5] T. Shimodaira, T. Kishimoto, and H. Saito, *Connection between rotation and miscibility in a two-component Bose–Einstein condensate*, Phys. Rev. A **82**, 013647 (2010).

[6] H. Pu, C. K. Law, J. H. Eberly, and N. P. Bigelow, *Coherent disintegration and stability of vortices in condensates*, Phys. Rev. A **59**, 1533 (1999).

[7] C. Ryu, M. F. Andersen, P. Cladé, V. Natarajan, K. Helmerson, and W. D. Phillips, *Observation of persistent flow of a Bose–Einstein condensate in a toroidal trap*, Phys. Rev. Lett. **99**, 260401 (2007).

[8] S. Moulder, S. Beattie, R. P. Smith, N. Tammuz, and Z. Hadzibabic, *Quantized supercurrent decay in an annular Bose–Einstein condensate*, Phys. Rev. A **86**, 013629 (2012).

[9] S. Eckel, F. Jendrzejewski, A. Kumar, C. J. Lobb, and G. K. Campbell, *Interferometric measurement of the current-phase relationship of a superfluid weak link*, Phys. Rev. X **4**, 031052 (2014).

[10] A. L. Fetter, B. Jackson, and S. Stringari, *Rapid rotation of a Bose-Einstein condensate in a harmonic plus quartic trap*, Phys. Rev. A **71**, 013605 (2005).

[11] A. Ramanathan, K. C. Wright, S. R. Muniz, M. Zelan, W. T. Hill, C. J. Lobb, K. Helmerson, W. D. Phillips, and G. K. Campbell, *Superflow in a toroidal Bose–Einstein condensate: An atom circuit with a tuneable weak link*, Phys. Rev. Lett. **106**, 130401 (2011).

[12] S. Beattie, S. Moulder, R. J. Fletcher, and Z. Hadzibabic, *Persistent currents in spinor condensates*, Phys. Rev. Lett. **110**, 025301 (2013).

[13] K. M. Mertes, J. W. Merrill, R. Carretero-González, D. J. Frantzeskakis, P. G. Kevrekidis, and D. S. Hall, *Nonequilibrium dynamics and superfluid ring excitations in binary Bose–Einstein condensates*, Phys. Rev. Lett. **99**, 190402 (2007).

[14] F. Le Kien, V. I. Balykin, and K. Hakuta, *Atom trap and waveguide using a two-color evanescent light field around a subwavelength-diameter optical fiber*, Phys. Rev. A **70**, 063403 (2004).

[15] E. Vetsch, D. Reitz, G. Sagué, R. Schmidt, S. T. Dawkins, and A. Rauschenbeutel, *Optical interface created by laser-cooled atoms trapped in the evanescent field surrounding an optical nanofiber*, Phys. Rev. Lett. **104**, 203603 (2010).

[16] C. J. Pethick and H. Smith, Bose–Einstein condensation in dilute gases (Cambridge University Press, 2008).

[17] P. Ao and S. T. Chui, *Symmetric-asymmetric transition in mixtures of Bose–Einstein condensates*, Phys. Rev. A **58**, 4836 (1998).

[18] E. Timmermans, *Phase separation of Bose–Einstein condensates*, Phys. Rev. Lett. **81**, 5718 (1998).

[19] J. Smyrnakis, S. Bargi, G. M. Kavoulakis, M. Magiropoulos, K. Kärkkäinen, and S. M. Reimann, *Mixtures of Bose gases confined in a ring potential*, Phys. Rev. Lett. **103**,

100404 (2009).
[20] L. Wen, W. M. Liu, Y. Cai, J. M. Zhang, and J. Hu, *Controlling phase separation of a two-component Bose–Einstein condensate by confinement*, Phys. Rev. A **85**, 043602 (2012).
[21] M. Abad, A. Sartori, S. Finazzi, and A. Recati, *Persistent currents in two-component condensates in a toroidal trap*, Phys. Rev. A **89**, 053602 (2014).
[22] P. Mason, *Ground states of two-component condensates in a harmonic plus Gaussian trap*, Eur Phys. J. B. **86**, 453 (2013).
[23] H. Salman, *A time-splitting pseudo spectral method for the solution of the Gross–Pitaevskii equations using spherical harmonics with generalised-Laguerre basis functions*, Journal of Computational Physics **258**, 185 (2014).
[24] S. Coen and M. Haelterman, *Domain wall solitons in binary mixtures of Bose–Einstein condensates*, Phys. Rev. Lett. **87**, 140401 (2001).
[25] J. R. Abo-Shaeer, C. Raman, J. M. Vogels, and W. Ketterle, *Observation of vortex lattices in Bose–Einstein condensates*, Science **292**, 476 (2001).
[26] J. Maurer and P. Tabeling, *Local investigation of superfluid turbulence*, Europhys. Lett. **43**, 29 (1998).
[27] C. Nore, M. Abid, and M. E. Brachet, *Kolmogorov turbulence in low-temperature superflows*, Phys. Rev. Lett. **78**, 3896 (1997).
[28] S. R. Stalp, L. Skrbek, and R. J. Donnelly, *Decay of grid turbulence in a finite channel*, Phys. Rev. Lett. **82**, 4831 (1999).
[29] T. Araki, M. Tsubota, and S. K. Nemirovskii, *Energy spectrum of superfluid turbulence with no normal–fluid component*, Phys. Rev. Lett. **89**, 145301 (2002).
[30] J. Salort, C. Baudet, B. Castaing, B. Chabaud, F. Daviaud, T. Dedelot, P. Diribarne, B. Dubrulle, Y. Gagne, F. Gauthier, et al., *Turbulent velocity spectra in superfluid flows*, Phys. Fluids **22**, 125102 (2010).

7.6 Discussion and Future Work

The portion of this chapter dealing with radial phase separation (Sec. 7.4) is still a work in progress and in my thesis I have laid the foundations by carrying out the full variational approach. However, the question of stability needs to be answered before the material can be considered for publication, which can be done using Bogoliubov-de Gennes theory on the trial wavefunction or the exact numerical solution. For energetic instabilities originating from the Landau criterion, it is important to determine the speed of sound, which in multi-component systems can be different to the well-known free space result. In addition, the existence of a dynamical instability due to a possible counterflow needs to be investigated.

It is also possible to imagine a more complex phase diagram using three component systems. Here two components can, for example, azimuthally phase separate, whereas a third component carrying a larger amount of angular momentum radially phase separates with respect to the other two. Trapping geometries which are not rotationally symmetric are also of large interest, as they do not require the conservation of angular momentum and therefore can allow for additional dynamics or instabilities.

Finally, situations in which one component is significantly smaller than the other can lead to the interesting regime of Josephson physics, where in the azimuthally phase separated regime the majority component is tunnel-coupled through the minority one.

Chapter 8

Conclusions

This thesis has focused around a few main topics including (i) the introduction of nanofibers into a system of cold atoms trapped in an optical lattice (in Chapter 3), (ii) the various trapping geometries that can be created using the first few modes of a nanofiber (in Chapter 4), (iii) the use of a nanofiber as a detector of single atoms in periodic arrays (in Chapter 5), (iv) the light scattering into a nanofiber due to an inhomogeneous atomic distribution close to its surface (in Chapter 6), and (v) the radial and azimuthal phase separation of a two-component condensate in a toroidal trap (in Chapter 7).

Even though each chapter had its own conclusions section, here I will provide a brief and general summary of my work.

In Chapters 3, 4, 5 and 6 I have discussed several examples of systems where tapered nanofibers are integrated into a cold atomic system and shown that such systems are versatile and realistic. While experiments in such systems are already delivering impressive results, they have by far not reached their full potential and one can predict many more exciting applications to come in the future. I would expect that nanofibers will play a significant role in the first realizations of quantum technologies based on integrating atoms and light.

While at first glance the work presented in Chapter 7 might seem to be a divergence from the rest of the thesis, it is connected by the fact that toroidal trapping

potentials can naturally be made using the evanescent field around a nanofiber. Their advantage is that these traps would be highly stable, as the fields creating them are inherently linked to the fiber and can therefore not drift with respect to each other.

Multicomponent superfluids have only become available over a wider range with the appearance of gaseous BECs and a lot of the associated physics is still unknown. The emergence of classical rotation in a quantum system is a rather unexpected finding and clearly demonstrates that these systems hold potential for dynamics quite different from single component systems. With first experiments in this area appearing at the moment, I would expect many more interesting results to be discovered in the near future.

Appendices

Appendix A

Variational Expressions

Here we give the various expressions relating to the variational approach described in Chapter 7. The normalization of the trial wavefunction is given by ($X_1 = \sqrt{2A_1}R_1$)

$$\langle \Psi_1 | \Psi_1 \rangle = \frac{\pi \left(\sqrt{\pi} X_1 (2X_1^2 + 3)(\mathrm{erf}(X_1) + 1) + e^{-X_1^2}(2X_1^2 + 2) \right)}{8\mathrm{A}_1^2}. \tag{A.1}$$

The expectation value of the kinetic energy is

$$\begin{aligned} \left\langle \Psi_1 \left| \frac{\hbar^2}{2m} \nabla^2 \right| \Psi_1 \right\rangle =& \frac{\pi \hbar^2 \left(\sqrt{\pi} X_1 (2X_1^2 + 5)(\mathrm{erf}(X_1) + 1) + e^{-X_1^2}(2X_1^2 + 4) \right)}{16\mathrm{A}_1 m} \\ &+ \frac{\pi \kappa_1^2 \hbar^2 \left(\sqrt{\pi} X_1 \left(\mathrm{erf}(X_1) + 1 \right) + e^{-X_1^2} \right)}{4\mathrm{A}_1 m}, \end{aligned} \tag{A.2}$$

where we note the dependence on the winding number, κ_1. The expectation value of the potential energy is

$$\begin{aligned}\langle\Psi_1|V|\Psi_1\rangle = \frac{\pi m\omega^2 e^{-X_1^2}}{(4A_1)^3}\Bigg[&4\mathrm{A}_1 r_0^2\left(\sqrt{\pi}X_1\left(2X_1^2+3\right)e^{X_1^2}\left(\mathrm{erf}(X_1)+1\right)+2X_1^2+2\right)\\&+\sqrt{\pi}X_1(4X_1^2(X_1^2+5)+15)e^{X_1^2}\left(\mathrm{erf}(X_1)+1\right)\\&+2\sqrt{2\pi}\sqrt{\mathrm{A}_1}r_0\left(4X_1^2\left(X_1^2+3\right)+3\right)e^{X_1^2}\left(\mathrm{erfc}(X_1)-2\right)\\&-8\mathrm{R}_1\mathrm{A}_1 r_0\left(2X_1^2+5\right)+2\left(X_1^2+4\right)\left(2X_1^2+1\right)\Bigg]\end{aligned} \tag{A.3}$$

The expectation value of the self-interaction term of the Hamiltonian is

$$\begin{aligned}&\langle\Psi_1|g_{11}|\Psi_1|^2|\Psi_1\rangle =\\&\frac{e^{-X_1^2}(\sqrt{\frac{\pi}{2}}g_{11}e^{2X_1^2}X_1(16X_1^4+40X_1^2+15)(\mathrm{erf}(\sqrt{2}X_1)+1)+2g_1(X_1^2+2)(4X_1^2+1))}{16A_1(\sqrt{\pi}e^{X_1^2}X_1(2X_1^2+3)(\mathrm{erf}(X_1)+1)+2X_1^2+2)}\end{aligned} \tag{A.4}$$

The expectation value of the interaction term of the Hamiltonian is

$$\begin{aligned}&\langle\Psi_1|g_{12}|\Psi_2|^2|\Psi_1\rangle = \frac{A_2^2 g_{12}e^{-(X_1^2+X_2^2)}}{4(A_1+A_2)^5(\sqrt{\pi}X_2(2X_2^2+3)(\mathrm{erf}(X_2)+1)+2e^{-X_2^2}(X_2^2+1))}\times\\&\Bigg\{2(A_1+A_2+2A_1X_1^2+4\sqrt{A_1A_2}X_1X_2+2A_1X_2^2)(A_1(4+X_1^2)+2\sqrt{A_1A_2}X_1X_2+A_2(4+X_2^2))+\\&\Bigg[\frac{\sqrt{\pi}e^{\frac{(\sqrt{A_1}X_1+\sqrt{A_2}X_2)^2}{A_1+A_2}}(\sqrt{A_1}X_1+\sqrt{A_2}X_2)}{\sqrt{A_1+A_2}}\times\\&\Big(8X_1X_2(5(\sqrt{{A_1}^3A_2}+\sqrt{A_1{A_2}^3})+2{X_1}^2\sqrt{{A_1}^3A_2}+2{X_2}^2\sqrt{A_1{A_2}^3})+{A_1}^2(4({X_1}^2+5){X_1}^2+15)\\&+2A_1A_2(2{X_1}^2(6{X_2}^2+5)+5(2{X_2}^2+3))+{A_2}^2(4({X_2}^2+5){X_2}^2+15)\Big)+\\&\frac{\sqrt{\pi}e^{\frac{(\sqrt{A_1}X_1+\sqrt{A_2}X_2)^2}{A_1+A_2}}(\sqrt{A_1}X_1+\sqrt{A_2}X_2)}{\sqrt{A_1+A_2}}\times\\&\Big((8X_1X_2(5(\sqrt{{A_1}^3A_2}+\sqrt{A_1{A_2}^3})+2{X_1}^2\sqrt{{A_1}^3A_2}+2{X_2}^2\sqrt{A_1{A_2}^3})+{A_1}^2(4({X_1}^2+5){X_1}^2+15)\\&+2A_1A_2(2{X_1}^2(6{X_2}^2+5)+5(2{X_2}^2+3))+{A_2}^2(4({X_2}^2+5){X_2}^2+15))\mathrm{erf}(\frac{\sqrt{A_1}X_1+\sqrt{A_2}X_2}{\sqrt{A_1+A_2}})\Big)\Bigg]\end{aligned} \tag{A.5}$$

The corresponding expressions for Ψ_2 can be arrived at by switching all of the subscripts, i.e. replacing 1 by 2, and 2 by 1. As these expressions are rather cumbersome, they are minimised numerically for the results presented in Chapter 7.

Bibliography

[1] S. N. Bose, Z. Phys. **26**, 178 (1924).
Plancks Gesetz und Lichtquantenhypothese.

[2] A. Einstein, Sitzungsber. Kgl. Preuss. Akad. Wiss. **22**, 261 (1924).
Quantentheorie des einatomigen idealen Gases.

[3] F. London, Nature **141**, 643 (1938).
The λ-Phenomenon of Liquid Helium and the Bose-Einstein Degeneracy.
F. London, Phys. Rev. **54**, 947 (1938).
On the Bose-Einstein Condensation.

[4] N. N. Bogoliubov, J. Phys. USSR **11**, 23 (1947).
On the theory of superfluidity.

[5] M. H. Anderson, J. R. Ensher, M. R. Matthews, C. E. Wieman, and E. A. Cornell, Science **269**, 198 (1995).
Observation of Bose–Einstein Condensation in a Dilute Atomic Vapor.

[6] K. B. Davis, M.-O. Mewes, M. R. Andrews, N. J. van Druten, D. S. Durfee, D. M. Kurn, and W. Ketterle, Phys. Rev. Lett. **75**, 3969 (1995).
Bose-Einstein Condensation in a Gas of Sodium Atoms.

[7] C. C. Bradley, C. A. Sackett, J. J. Tollett, and R. G. Hulet, Phys. Rev. Lett. **75**, 1687 (1995).
Evidence of Bose-Einstein Condensation in an Atomic Gas with Attractive Interactions.

[8] B. DeMarco, and D. S. Jin, Science **285**, 1703 (1999).
Onset of Fermi degeneracy in a trapped atomic gas.

[9] E. A. Cornell, J. R. Ensher, and C. E. Wiemann, edited by M. Inguscio, S. Stringari, and C. E. Wiemann (Proc. Int. School Physics, 'Enrico Fermi', course CXL), p15.
Bose-Einstein Condensation in Atomic Gases.

[10] W. Ketterle, D. S. Durfee, and D. M. Stamper-Kurn, edited by M. Inguscio, S. Stringari, and C.E. Wiemann (Proc. Int. School Physics, 'Enrico Fermi', course CXL), p67.
Bose-Einstein Condensation in Atomic Gases.

[11] M. Lewenstein, A. Sanpera, V. Ahufinger, B. Damski, A. Sen(De) and U. Sen, Adv. Phys. **56**, 243 (2007).
Ultracold atomic gases in optical lattices: mimicking condensed matter physics and beyond.

[12] C. K. Kao and T. W. Davies, J. Sci. Instrum. **1**, no. 2, p.1063, 1968.
Spectroscopic studies of ultra low loss optical glasses.
K. C. Kao and G. A. Hockham, Proc. Inst. Elect. Eng. **113**, 1151 (1966).
Dielectric-fiber surface waveguides for optical frequencies.

[13] J. M. Ward, V. H. Le, A. Maimaiti, and S. Nic Chormaic, Rev. Sci. Instrum. **85**, 111501 (2014).
Optical micro- and nanofiber pulling rig.

[14] K. P. Nayak, P. N. Melentiev, M. Morinaga, Fam Le Kien, V. I. Balykin, and K. Hakuta, Optics Express **15**, 5431 (2007).
Optical nanofiber as an efficient tool for manipulating and probing atomic fluorescence.

[15] L. Zhang, J. Lou, and L. Tong, Photonic Sensors **1**, 1, p. 31 (2011).
Micro/Nanofiber Optical Sensors.

[16] F. Le. Kien, V. I. Balykin, and K. Hakuta, Phys. Rev. A **70**, 063403 (2004).
Atom trap and waveguide using a two-color evanescent light field around a subwavelength-diameter optical fibre.

[17] E. Vetsch, D. Reitz, G. Sagué, R. Schmidt, S. Dawkins, and A. Rauschenbeutel, Phys. Rev. Lett. **104**, 203603 (2010).
Optical Interface Created by Laser-Cooled Atoms Trapped in the Evanescent Field Surrounding an Optical Nanofiber.

[18] D. Jaksch, C. Bruder, J. I. Cirac, C.W. Gardiner, and P. Zoller. Phys. Rev. Lett. **81**, 3108 (1998).
Cold Bosonic Atoms in Optical Lattices.

[19] M. Greiner, O. Mandel, T. Esslinger, T. W. Hansch and I. Bloch, Nature **415**, 39 (2002).
Quantum phase transition from a superfluid to a Mott insulator in a gas of ultracold atoms.

[20] T. Stoferle, H. Moritz, C. Schori, M. Kohl and T. Esslinger, Phys. Rev. Lett. **92**, 13 (2004).
Transition from a strongly interacting 1D superfluid to a Mott insulator.

[21] B. Paredes, A. Widera, V. Murg, O. Mandel, S. Folling, I. Cirac, G. V. Shlyapnikov, T. W. Hansch and I. Bloch, Nature **429**, 277 (2004).
Tonks-Girardeau gas of ultracold atoms in an optical lattice.

[22] T. Kinoshita, T. Wenger and D. S. Weiss, Science **305**, 1125 (2004).
Observation of a one-dimensional Tonks- Girardeau gas.

[23] M. Takamoto, F. L. Hong, R. Higashi and H. Katori, Nature **435**, 321 (2005).
An optical lattice clock.

[24] A. Kay, J. K. Pachos, New Journal of Physics **6**, 126 (2004).
Quantum Computation in optical lattices via global laser addressing.

[25] T. Calarco, U. Dorner, P. Julienne, C. Williams, and P. Zoller, Phys. Rev. A **7**0, 012306 (2004).

Quantum computations with atoms in optical lattices: marker qubits and molecular interactions.

[26] F. Shimizu, Japanese Journal of Appl. Phy. **43**, 8376 (2004).
Scalable Quantum Computer with Optical Lattices.

[27] I. Bloch, J. Dalibard, W. Zwerger. Rev. of Mod. Phys. **80**, 885 (2008).
Many-body physics with ultracold gases.

[28] I. Bloch, Nature Physics **1**, 23 (2005).
Ultracold quantum gases in optical lattices.

[29] W. S. Bakr, J. I. Gillen, A. Peng, S. Fölling, and M. Greiner, Nature **462**, 74 (2009).
A quantum gas microscope for detecting single atoms in a Hubbard-regime optical lattice.

[30] J. F. Sherson, C. Weitenberg, M. Endres, M. Cheneau, I. Bloch, and S. Kuhr, Nature **467**, 68 (2010).
Single-atom-resolved fluorescence imaging of an atomic Mott insulator.

[31] I. Bloch and M. Greiner, Adv. At. Mol. Opt. Phys. **52**, 1 (2005).
Exploring quantum matter with ultracold atoms in optical lattices.

[32] C. J. Foot, *Atomic Physics*, Oxford Master Series in Atomic, Optical and Laser Physics, Oxford University Press, 2007.

[33] R. Grimm, M. Weidemüller, and Y. B. Ovchinnikov, Adv. in At. Mol and Opt. Phys. **42**, 95 (2000).
Optical Dipole Traps for Neutral Atoms.

[34] See, for example, J. D. Jackson, *Classical Electrodynamics*, 3rd ed, J. Wiley, New York, 1999.

[35] L. Allen and J. H. Eberly, *Optical Resonance and Two Level Atoms*, J.Wiley, New Your, 1975.

[36] S. Chu, Rev. Mod. Phys. **70**, 685 (1998).
Nobel lecture: the manipulation of neutral particles.
C. Cohen-Tannoudji, Rev. Mod. Phys. **70**, 707 (1998).
Nobel lecture: manipulating atoms with photons.
W. D. Phillips, Rev. Mod. Phys. **70**, 721 (1998).
Nobel lecture: laser cooling and trapping of neutral atoms.

[37] H. J. Metcalf and P. van der Straten. *Laser Cooling and Trapping*, Springer-Verlag, 1999.

[38] S. Peil, J. V. Porto, B. L. Tolra, J. M. Obrecht, B. E. King, M. Subbotin, S. L. Rolston, and W. D. Phillips. Phys. Rev. A **67**, 051603 (2003).
Patterned loading of a Bose-Einstein condensate into an optical lattice.

[39] Z. Hadzibabic, S. Stock, B. Battelier, V. Bretin, and J. Dalibard. Phys. Rev. Lett. **93**, 180403 (2004).
Interference of an Array of Independent Bose-Einstein Condensates.

[40] D. Jaksch and P. Zoller. Ann. Phys. **315**, 52 (2005).
The cold atom Hubbard toolbox.

[41] M. Fisher, P. Weichman, G. Grinstein and D. Fisher. Phys. Rev. B **40**, 546 (1989).
Boson localization and the superfluid-insulator transition.

[42] A. Yariv, *Optical Electronics*, CBS College, New York, 1985.

[43] H. L. Sørensen, Master's Thesis, University of Copenhagen (2013).
Controlling the shape of subwavelength-diameter tapered optical fibers.

[44] A. W. Snyder, J. D. Love, *Optical Waveguide Theory*, Chapman and Hall, New York, 1983.

[45] J. Ward, D. O'Shea, B. Shortt, M. Morrissey, K. Deasy and S. Nic Chormaic. Rev. Sci. Instrum. **77**, 083105 (2006).
A heat-and-pull rig for fiber taper fabrication.

[46] L. Tong, R. R. Gattass, J. B. Ashcom, S. He, J. Lou, M. Shen, I. Maxwell and E. Mazur. Nature **426**, 816 (2003).
Subwavelength-diameter silica wires for low-loss optical waveguiding.

[47] F. Warken, E. Vetsch, D. Meschede, M. Sokolowski and A. Rauschenbeutel, Optics Express **15**, 11952 (2007).
Ultrasensitive surface absorption spectroscopy using sub-wavelength diameter optical fibers.

[48] F. Le Kien, V. I. Balykin, and K. Hakuta, Phys. Rev. A **73**, 053823 (2006).
Angular momentum of light in an optical nanofiber.

[49] G. Sagué, PhD Dissertation, University of Bonn, (2008).
Cold atom physics using ultra-thin optical fibers.

[50] Fam Le Kien, S. Dutta Gupta, V. I. Balykin, and K. Hakuta, Phys. Rev. A **72**, 032509 (2005).
Spontaneous emission of a cesium atom near a nanofiber: Efficient coupling of light to guided modes.

[51] G. Sagué, A. Baade and A. Rauschenbeutel, New J. Phys. **10**, 113008 (2008).
Blue-detuned evanescent field surface traps for neutral atoms based on mode interference in ultra-thin optical fibres.

[52] G. Sagué, E. Vetsch, W. Alt, D. Meschede and A. Rauschenbeutel, Phys. Rev. Lett. **99**, 163602 (2007).
Cold Atom Physics Using Ultra-Thin Optical Fibers: Light-Induced Dipole Forces and Surface Interactions.

[53] J. Bures and R. Ghosh, J. Opt. Soc. Am. A **16**, 8 (1999)
Power density of the evanescent field in the vicinity of a tapered fiber.

[54] F. Le Kien, J. Q. Liang, K. Hakuta, and V. I. Balykin, Opt. Commun. **242**, 445 (2004).
Field intensity distributions and polarization orientations in a vacuum-clad subwavelength-diameter optical fiber.

[55] Fam Le Kien, J.Q. Liang, K. Hakuta, and V. I. Balykin, Optics Communications **242**, 445 (2004).
Field intensity distributions and polarization orientations in a vacuum-clad subwavelength-diameter optical fibre.

[56] See, for example; D. Marcuse, *Light Transmission Optics*, Krieger, 1989; A. W. Snyder and J. D. Love, *Optical Waveguide Theory*, Chapman and Hall, New York, 1983.

[57] M. Boustimi, J. Baudon, P. Candori, and J. Robert, Phys. Rev. B **65**, 155402 (2002).
van der Waals interaction between an atom and a metallic nanowire.
M. Boustimi, J. Baudon, and J. Robert. Phys. Rev. B, **67**, 045407 (2003).
Molecules interacting with a metallic nanowire.

[58] V. I. Balykin, K. Hakuta, Fam Le Kien, J. Q. Liang, and M. Morinaga, Phys. Rev. A **70**, 011401 (2004).
Atom trapping and guiding with a subwavelength-diameter optical fiber.

[59] V. I. Balykin, V.G. Minogin, and V. S. Letokhov, Rep. Prog. Phys **63**, 1429 (2000).
Electromagnetic trapping of cold atoms.

[60] Yu. B. Ovchinnikov, S. V. Shul'ga, and V. I. Balykin, J. Phys. B **24**, 3173 (1991).
An atomic trap based on evanescent light waves.

[61] F. Le Kien, V. I. Balykin, and K. Hakuta, J. Phys. Soc. Japan **74**, 910 (2005).
State insensitive trapping and guiding of cesium atoms using a two-color evanescent field around a subwavelength-diameter fiber.

[62] A. Goban, K. S. Choi, D. J. Alton, D. Ding, C. Lacröute, M. Potoschnig, T. Thiele, N. P. Stern, and H. J. Kimble, Phys. Rev. Lett. **109**, 033603 (2012).
Demonstration of a state insensitive, compensated nanofiber trap.

[63] C. Lacröute, K. S. Choi, A. Goban, D. J. Alton, D. Ding, N. P. Stern, and H. J. Kimble, New J. Phys. **14**, 023056 (2012).
A state-insensitive, compensated nanofiber trap.

[64] L. Tong, J. Lou, and E. Mazur, Opt. Express **12**, 1025 (2004).
Single-mode guiding properties of subwavelength-diameter silica and silicon wire waveguides.

[65] L. Russell, D. A. Gleeson, V. G. Minigon, and S. Nic Chormaic, J. Phys. B: At. Mol. Opt. Phys. **42**, 185006 (2009).
Spectral Distribution of atomic flouresence coupled into an optical nano-fibre.

[66] W. R. Johnson, V. A. Dzuba, U. I. Safronova and M. S. Safronova, Phys. Rev. A **69**, 022508 (2004).
Finite-field evaluation of the Lennard-Jones atom-wall interaction constant C3 for alkali-metal atoms.

[67] J. E. Sansonetti, W. C. Martin, and S. L. Young, *Handbook of Basic Atomic Spectroscopic Data* (version 1.00). http://physics.nist.gov/Handbook. National Institute of Standards and Technology, Gaithersburg, MD.

[68] J. Estève, C. Gross, A. Weller, S. Giovanazzi and M. K. Oberthaler, Nature **455**, 1216 (2008).
Squeezing and entanglement in a Bose-Einstein condensate.

[69] P. Würtz, T. Langen, T. Gericke, A. Koglbauer, and H. Ott, Phys. Rev. Lett. **103**, 080404 (2009).
Experimental demonstration of single-site addressability in a two-dimensional optical lattice.

[70] M. P. MacDonald, K. Volke-Sepulveda, L. Paterson, J. Arlt, W. Sibbett, and K. Dholakia, Opt. Commun. **201**, 21 (2002) .
Revolving interference patterns for the rotation of optically trapped particles.

[71] A. Yu. Okulov, Phys. Lett. A **376**, 650 (2012).
Cold matter trapping via slowly rotating helical potential.

[72] A. Petcu-Colan, M. C. Frawley, and S. Nic Chormaic, JNOPM **20**, 293–307 (2011).
Tapered Few-Mode Fibers: Mode Evolution during Fabrication and Adiabaticity.

[73] M. C. Frawley, A. Petcu-Colan, V. Giang Truong, and S. Nic Chormaic, Opt. Commun. **285**, 4648 (2012).
Higher order mode propagation in an optical nanofiber.

[74] S. Ravets, J. E. Hoffman, L. A. Orozco, S. L. Rolston, G. Beadie, and F. K. Fatemi, Opt. Express **21**, 18325 (2013).
A low-loss photonic silica nanofiber for higher-order modes.

[75] D. Reitz and A. Rauschenbeutel, Opt. Commun. **285**, 4705 (2012).
Nanofiber-based double-helix dipole trap for cold neutral atoms.

[76] K. T. Law and D. E. Feldman, Phys. Rev. Lett. **101**, 096401 (2008) .
Quantum Phase Transition Between a Luttinger Liquid and a Gas of Cold Molecules.

[77] P. Schmelcher, Europhys. Lett. **95**, 50005 (2011).
Effective long-range interactions in confined curved dimensions.

[78] O. V. Kibis, Phys. Lett. A **166**, 393 (1992) .
Electron-electron interaction in a spiral quantum wire.

[79] M. Karski, L. Förster, J. M. Choi, W. Alt, A. Widera, and D. Meschede, Phys. Rev. Lett. **102**, 053001 (2009).
Nearest-neighbor detection of atoms in a 1D optical lattice by fluorescence imaging.

[80] K. P. Nayak and K. Hakuta, New Journal of Physics **10**, 053003 (2008).
Single atoms on an optical nanofiber.

[81] A. V. Masalov and V. G. Minogin, Laser Phys. Lett. **10**, 075203 (2013).
Pumping of higher-modes of an optical nanofiber by laser excited atoms.

[82] R. Kumar, V. Gokhroo, A. Maimaiti, K. Deasy, M. C. Frawley, and S. Nic Chormaic, New J. Phys. **17**, 013026 (2015).
Interaction of laser-cooled ^{87}Rb atoms with higher order modes of an optical nanofiber.

[83] K. Baumann, C. Guerlin, F. Brennecke, and T. Esslinger, Nature (London) **464**, 1301 (2010).
Dicke quantum phase transition with a superfluid gas in an optical cavity.

[84] D. Chang, L. Jiang, A. Gorshkov, and H. Kimble, New J. Phys. **14**, 063003 (2012).
Cavity QED with atomic mirrors.

[85] D. E. Chang, J. I. Cirac, and H. J. Kimble, Phys. Rev. Lett. **110**, 113606 (2013).
Self-Organization of Atoms along a Nanophotonic Waveguide.

[86] M. D. Girardeau, E. M. Wright, and J. M. Triscari, Phys. Rev. A **63**, 033601 (2001).
Ground-state properties of a one-dimensional system of hard-core bosons in a harmonic trap.

[87] M. Girardeau, J. Math. Phys. **1**, 516 (1960).
Relationship between Systems of Impenetrable Bosons and Fermions in One Dimension.

[88] T. Grießer and H. Ritsch, Phys. Rev. Lett. **111**, 055702 (2013).
Light induced crystallization of cold atoms in a 1D optical trap.

[89] D. Holzmann, M. Sonnleitner, and H. Ritsch, Eur. Phys. J. D **68**, 352 (2014).
Self-ordering and collective dynamics of transversely illuminated point-scatterers in a 1D trap.

[90] R. E. Collin, *Field Theory of Guided Waves*, IEEE Press, New York, pp.45-47, 1991.

[91] M. Olshanii, Phys. Rev. Lett. **81**, 938 (1998).
Atomic Scattering in the Presence of an External Confinement and a Gas of Impenetrable Bosons.

[92] Th. Busch, B. G. Englert, K. Rzazewski, and M. Wilkens, Foundations of Physics **28**, 549 (1998).
Two cold atoms in a trap.

[93] L. Tonks, Phys. Rev. **50**, 955 (1936).
The Complete Equation of State of One, Two and Three-Dimensional Gases of Hard Elastic Spheres.

[94] V. I. Yukalov and M. D. Girardeau, Laser Phys. Lett. **2**, 375 (2005).
Fermi-Bose mapping for one-dimensional Bose gases.

[95] M. D. Girardeau and E. M. Wright, Phys. Rev. Lett. **84**, 5239 (2000).
Breakdown of Time-Dependent Mean-Field Theory for a One-Dimensional Condensate of Impenetrable Bosons.

[96] C. Maschler, H. Ritsch, A. Vukics, and P. Domokos, Opt. Comm. **273**, 446 (2007).
Entanglement assisted fast reordering of atoms in an optical lattice within a cavity at $T = 0$.

[97] C. Monroe, Nature **416**, 238 (2002).
Quantum information processing with atoms and photons.

[98] J. F. Allen and A. D. Misener, Nature **141**, 75 (1938).
Flow of liquid helium II.

[99] L. Tisza, Nature **141**, 913, (1938).
Transport phenomena in helium II.

[100] R. Onofrio, C. Raman, J. M. Vogels, J. R. Abo-Shaeer, A. P. Chikkatur, and W. Ketterle, Phys. Rev. Lett. **85**, 2228, (2000).
Observation of superfluid flow in a Bose-Einstein condensed gas.

[101] G. Hechenblaikner, E. Hodby, S. A. Hopkins, O. M. Maragò, and C. J. Foot, Phys. Rev. Lett. **88**, 070406 (2002).
Direct Observation of Irrotational Flow and Evidence of Superfluidity in a Rotating Bose-Einstein Condensate.

[102] K. W. Madison, F. Chevy, W. Wohlleben, and J. Dalibard, Phys. Rev. Lett. **84**, 806 (2000).
Vortex formation in a stirred Bose-Einstein condensate.

[103] E. Hodby, G. Hechenblaikner, S. A. Hopkins, O. M. Maragò, and C. J. Foot, Phys. Rev. Lett. **88**, 010405 (2001).
Vortex Nucleation in Bose-Einstein Condensates in an Oblate, Purely Magnetic Potential.

[104] H. K. Onnes, Akad. van Wetenschappen **14**, 818 (1911).
On the sudden rate at which the resistance of mercury disappears.

[105] D. J. Quinn and W. B. Ittner, Journal of Applied Physics **33**, 748 (1962).
Resistance in a Superconductor.

[106] F. Bloch, Phys. Rev. A **7**, 2187 (1973).
Superfluidity in a Ring.

[107] J. Smyrnakis, S. Bargi, G. M. Kavoulakis, M. Magiropoulos, K. Kärkkäinen, and S. M. Reimann, Phys. Rev. Lett. **103**, 100404 (2009).
Mixtures of Bose Gases Confined in a Ring Potential.

[108] S. Bargi, F. Malet, G. M. Kavoulakis, and S. M. Reimann, Phys. Rev. A **82**, 043631 (2010).
Persistent currents in Bose gases confined in annular traps.

[109] K. Anoshkin, Z. Wu, and E. Zaremba, Phys. Rev. A **88**, 013609 (2013).
Persistent currents in a bosonic mixture in the ring geometry.

[110] Z. Wu and E. Zaremba, Phys. Rev. A **88**, 063640 (2013).
Mean-field yrast spectrum of a two-component Bose gas in ring geometry: Persistent currents at higher angular momentum.

[111] Z. Wu, E. Zaremba, J. Smyrnakis, M. Magiropoulos, N. K. Efremidis, and G. M. Kavoulakis, Phys. Rev. A **92**, 033630.
Mean-field yrast spectrum and persistent currents in a two-component Bose gas with interaction asymmetry.

[112] A. I. Yakimenko, K. O. Isaieva, S. I. Vilchinskii, and M. Weyrauch, Phys. Rev. A **88**, 051602(R) (2013).
Stability of persistent currents in spinor Bose-Einstein condensates.

[113] S. Beattie, S. Moulder, R. J. Fletcher, and Z. Hadzibabic, Phys. Rev. Lett. **110**, 025301 (2013).
Persistent Currents in Spinor Condensates.

[114] M. Abad, A. Sartori, S. Finazzi, and A. Recati, Phys. Rev. A **89**, 053602 (2014).
Persistent currents in two-component condensates in a toroidal trap.

[115] A. Ramanathan, K. C. Wright, S. R. Muniz, M. Zelan, W. T. Hill III, C. J. Lobb, K. Helmerson, W. D. Phillips, and G. K. Campbell, Phys. Rev. Lett. **106**, 130401 (2011).
Superflow in a Toroidal Bose-Einstein Condensate: An Atom Circuit with a Tunable Weak Link.

[116] S. Franke-Arnold, L. Allen, and M. Padgett, Laser and Photonics Reviews **2**, 299 (2008).
Advances in optical angular momentum.

[117] C. J. Pethick and H. S. Smith, *Bose-Einstein Condensation in Dilute Gases*, Cambridge University Press, 2008.

[118] L.P. Pitaevskii and S. Stringari, *Bose-Einstein Condensation*, Oxford University Press, 2003.

[119] K. M. Mertes, J. W. Merril, R. Carretero-González, D. J. Fratzeskakis, P. G. Kevrekidis, and D. S. Hall, Phys. Rev. Lett. **99**, 190402 (2007).

Nonequilibrium Dynamics and Superfluid Ring Excitations in Binary Bose-Einstein Condensates.

[120] L. Wen, W. M. Liu, Y. Cai, J. M. Zhang, and J. Hu, Phys. Rev. A **85**, 043602 (2012).
Controlling phase separation of a two-component Bose-Einstein condensate by confinement.

[121] J. F. Annett, *Superconductivity, Superfluids and Condensates*, Oxford Master Series in Condensed Matter Physics, Oxford University Press, 2003.

[122] A. K. Ramanathan, Ph.D. thesis, University of Maryland, College Park (2011).
A Ring with a Spin : Superfluidity in a toroidal Bose-Einstein condensate.

[123] C. Ryu, M. F. Andersen, P. Cladé, V. Natarajan, K. Helmerson, and W. D. Phillips, Phys. Rev. Lett. **99**, 260401 (2007).
Observation of Persistent Flow of a Bose-Einstein Condensate in a Toroidal Trap.

[124] S. Eckel, F. Jendrzejewski, A. Kumar, C. J. Lobb, and G. K. Campbell, Phys. Rev. X **4**, 031052 (2014).
Interferometric Measurement of the Current-Phase Relationship of a Superfluid Weak Link.

[125] K. C. Wright, R. B. Blakestad, C. J. Lobb, W. D. Phillips, and G. K. Campbell, Phys. Rev. Lett. **110**, 025302 (2013).
Driving Phase Slips in a Superfluid Atom Circuit with a Rotating Weak Link.

[126] N. Murray, M. Krygier, M. Edwards, K. C. Wright, G. K. Campbell, and C. W. Clark, Phys. Rev. A **88**, 053615, (2013).
Probing the circulation of ring-shaped Bose-Einstein condensates.

[127] S. Moulder, S. Beattie, R. P. Smith, N. Tammuz, and Z. Hadzibabic, Phys. Rev. A **86**, 013629 (2012).
Quantized supercurrent decay in an annular Bose-Einstein condensate.

[128] S. Franke-Arnold, J. Leach, M. J. Padgett, V. E. Lembessis, D. Ellinas, A. J. Wright, J. M. Girkin, P. Öhberg, and A. S. Arnold, Optics Express **15**, 8619 (2007).
Optical ferris wheel for ulatracold atoms.

[129] T. Hennessy and Th. Busch, Phys. Rev. A **85**, 053418 (2012).
Creating atom-number states around tapered optical fibers by loading from an optical lattice.

[130] T. Shimodaira, T. Kishimoto, and H. Saito, Phys. Rev. A **82**, 013647 (2010).
Coherent disintegration and stability of vortices in trapped Bose condensates.

[131] P. Mason, Eur Phys. J. B. **86**, 453 (2013).
Ground states of two-component condensates in a harmonic plus Gaussian trap.

[132] W. H. Press, S. A. Teukolsky, W. T. Vetterling, and B. P. Flannery, *Numerical Recipes in C*, Second edition, Cambridge University Press, 1992.